Advanced Numerical Methods in Diffractive Optics and Applications to Periodic Photonic Nanostructures

Zur Erlangung des akademischen Grades eines
Doktors der Naturwissenschaften
von der Fakultät für Physik des
Karlsruher Instituts für Technologie (KIT)

genehmigte

Dissertation

von

Diplom-Physikerin Sabine Essig
aus Baden-Baden

Tag der mündlichen Prüfung: 4. Februar 2011
Referent: Prof. Dr. Kurt Busch
Korreferent: Prof. Dr. Martin Wegener

Contents

1. Introduction

The interaction of electromagnetic radiation with matter, which is investigated in the research field of optics and photonics, has a wide variety of applications in telecommunication and sensing. Furthermore, microscopy and lithography make use of the fundamental properties of light and its interaction with matter, as well.
Especially, the optical properties of periodic systems such as photonic crystals [1, 2] and metamaterials [3] can be used for enhancing and modifying the interaction of light and matter. These systems may lead to the development of more efficient sensors [4], telecommunication devices with higher bandwidth, or microscopy and lithography with higher resolution [5] than feasible with conventional techniques. Since those structures represent artificial materials, they can be engineered to have special properties which are not available in nature.
The main focus in this thesis lies in the investigation of periodic photonic nanostructures, such as photonic crystals and metamaterials as well as periodically structured surfaces. These systems may exhibit interesting optical responses which can be exploited for numerous applications.
Photonic crystals contain a periodicity at the scale of the operation wavelength desired. With the appropriate choice of both the unit cell design, as woodpile photonic crystals or inverse opals, and the constituent materials, the resulting photonic crystal can exhibit a complete photonic band gap, i.e., a frequency range in which the propagation of electromagnetic waves is forbidden.
By deliberately introducing of deviations from the perfect periodicity, functional elements such as cavities and waveguiding structures can be realized [6]. They allow selected frequencies to propagate in the forbidden region and find applications in optical devices. Photonic crystals can support the advance in all-optical circuitry and data processing [7].
In contrast to photonic crystals, metamaterials require a periodicity at subwavelength range. Thus, they act as effective media. Consequently, their optical properties can be described by effective material parameters such as the refractive index, permittivity and permeability. It is especially intriguing that the metamaterial concept allows not only for tailoring the permittivity, but also the permeability. In order to vary the permeability, the structure needs to include also metallic components. Many interesting phenomena have been proposed for metamaterials, e.g. negative refractive indices [8], which allow for astonishing effects such as perfect lensing [5] or inverse Cherenkov radiation [8]. Additionally, metamaterials form the basis for certain types of cloaking devices [9, 10, 11].
In the visible and near-infrared part of the spectrum, the experimental realization of such devices remains challenging. Unfortunately, for general problems no analytical solutions are known. Thus, efficient numerical tools are required for both modeling

these devices and obtaining a deeper understanding of the underlying physics. These have to model the propagation and diffraction of light. Thereby, structured optical materials are characterized as well as optimized designs can be developed.
Since the individual problems have different requirements it is hard to find a numerical method which can handle all of them at once in adequate time. The method of choice depends on the system which shall be studied.
Numerical methods can be roughly subdivided into two distinct classes: time domain and frequency domain methods. Time domain methods are mainly more general methods which reproduce the situation by illuminating the investigated system with a light pulse. Then, they record the temporal evolution of the system. Here, the most popular method is the finite-difference time-domain method [12]. A further method is the discontinuous Galerkin time-domain method [13], which solves the spatial discretization part of the problem adapted to the structure via an unstructured grid instead of an equidistant cubic grid.
In many cases, the exact temporal response of the system on the exciting electric field is not important. More specialized methods can be applied. These are frequency domain methods which solve the time-harmonic Maxwell's equations. This set of equations can also be solved on an unstructured grid where the most popular method is the finite element method [14] but there are also other methods which are more adapted to special problems.
In the case of strictly periodic systems the plane-wave method [15] is advantageous. This method sets up an eigenvalue problem by Maxwell's equations in Fourier space to determine the bandstructure with the corresponding Bloch functions of the special system.
Another class of numerical methods is formed by the grating methods [16] which are specially adapted to grating systems. They treat the lateral periodicity in Fourier space whilst the finite part, which determines the propagation through the grating, is solved in real space. There are different possibilities to determine the finite part. Accordingly, several methods have been developed such as the differential method [16], the Chandezon method [17] and the Fourier Modal Method (FMM) [18].
In this thesis, we use and extend the FMM, which is an adequate and commonly used method for the numerical analysis of periodic structures and the investigation of their optical properties in frequency domain.

Outline of this Thesis

We will start in chapter 2 with a short introduction to the fundamentals of optics by Maxwell's equations and the description of different material types. We also take a look at the behavior of light which impinges on a material interface and more generally on a periodically structured surface. Additionally, we give a short overview on curvilinear coordinates in combination with Maxwell's equations. In the next chapter (chapter 3) we introduce the FMM and the Chandezon method after a short historical review on the developments in the numerical investigation of gratings. We also discuss some extensions to the FMM such as perfectly matched layers and excitation of the system by internal point sources. In chapter 4 we present calculations of photonic crystals. In the

case of woodpile photonic crystals, we investigate cavities and waveguiding structures. Opal photonic crystals are studied with respect to their polarization properties. In both cases we compare the calculations with experimentally measured results if possible. At the end (chapter 5) we present our efforts in improving the convergence of the FMM by application of adaptive spatial resolution. We investigate the convergence of three different test systems. Finally, we summarize this thesis in chapter 6 and give a short outlook.

2. Basic Principles of Classical Optics

In this chapter the fundamentals of optics are discussed. First, Maxwell's equations and the mathematical description of different materials are presented. Additionally, we state Poynting's theorem and introduce the plane wave solutions of the wave equation in homogeneous materials. Then, we determine the behavior of the fields at material interfaces and calculate transmittance and reflectance of a plane wave impinging onto a planar interface.
We give a short introduction to Maxwell's equations in covariant formulation, since we need this for the numerical method we apply. Because periodicity plays an essential role in this thesis, we introduce the optical properties of periodic systems. Finally, rescaled variables for Maxwell's equations are introduced.

2.1. Maxwell's Equations

Maxwell's equations provide the basis to describe electromagnetism [19]. They are a set of four equations which consists of two divergence equations

$$\nabla \cdot \mathbf{D}(\mathbf{r},t) = \rho(\mathbf{r},t), \tag{2.1a}$$
$$\nabla \cdot \mathbf{B}(\mathbf{r},t) = 0, \tag{2.1b}$$

and two curl equations

$$\nabla \times \mathbf{E}(\mathbf{r},t) = -\partial_t \mathbf{B}(\mathbf{r},t), \tag{2.2a}$$
$$\nabla \times \mathbf{H}(\mathbf{r},t) = \partial_t \mathbf{D}(\mathbf{r},t) + \mathbf{J}(\mathbf{r},t). \tag{2.2b}$$

Here, they are written in SI-units. Since we have stated the so-called macroscopic Maxwell equations, ρ depicts the free charge density and $\mathbf{J}$ the free current density in the system. By Maxwell's equations we can derive the continuity equation

$$\nabla \cdot \mathbf{J}(\mathbf{r},t) + \partial_t \rho(\mathbf{r},t) = 0, \tag{2.3}$$

which determines the conservation of charge in the system.
In this formulation of Maxwell's equations, the electric field $\mathbf{E}$ and the magnetic field $\mathbf{H}$ represent only macroscopic field quantities. They are locally averaged in space over the microscopic fields and do not depict the fields on atomic scale. However, also the contribution of the charges and currents which form the matter have to be considered. Thus, in order to include the existence of matter with its bound charges and currents, the macroscopic magnetic induction $\mathbf{B}$ and electric displacement field $\mathbf{D}$ are introduced.

2.2. Constitutive Relations

Maxwell's equations (2.1) and (2.2) can not give a full description of the electromagnetic fields. We also need relations between the four field quantities. These relations are given by the so-called material equations which are in general form [19, 20]

$$\mathbf{D} = \mathbf{D}\left[\mathbf{E}, \mathbf{H}\right], \tag{2.4a}$$
$$\mathbf{B} = \mathbf{B}\left[\mathbf{E}, \mathbf{H}\right], \tag{2.4b}$$

and describe the interaction of light with matter. Here, we consider only materials which do not cross-couple the electric and magnetic fields. The interaction is also assumed to be local in space and only dipolar interaction in the materials are taken into account. Thus, our starting point for the material equations is

$$\mathbf{D}(\mathbf{r}, t) = \epsilon_0 \mathbf{E}(\mathbf{r}, t) + \mathbf{P}(\mathbf{r}, t), \tag{2.5a}$$
$$\mathbf{B}(\mathbf{r}, t) = \mu_0 \mathbf{H}(\mathbf{r}, t) + \mu_0 \mathbf{M}(\mathbf{r}, t), \tag{2.5b}$$

with the electric polarization $\mathbf{P}$ and magnetization $\mathbf{M}$. μ_0 is the vacuum permeability and ϵ_0 the vacuum permittivity. They are related by the vacuum speed of light via $c_0^2 = 1/(\mu_0 \epsilon_0)$.
The polarization is the material contribution to the dielectric displacement field $\mathbf{D}$ and represents the response of the medium to the external electric field $\mathbf{E}$. The polarization can be expanded into orders of the electric field. We only consider the first order, since we deal only with weak electric fields. Thus, the linear dependency determines the behavior of light-matter interaction. The higher order terms would be responsible for nonlinear effects [21]. Some examples for second order nonlinear effects are second harmonic generation, sum frequency generation and difference frequency generation. The third order nonlinearity is responsible for self-focusing, self-phase modulation and third harmonic generation.
The linear interaction is described by

$$\mathbf{P}(\mathbf{r}, t) = \epsilon_0 \int_{-\infty}^{\infty} \mathrm{d}\tau \chi^{(1)}(\mathbf{r}, t - \tau) \mathbf{E}(\mathbf{r}, \tau), \tag{2.6}$$

with the electric susceptibility $\chi^{(1)}$. The time dependence of the susceptibility is due to the fact that the response of the matter to the external light does not need to be instantaneous in time. Since the integral (2.6) is a convolution, the relation is easier to examine in frequency domain by a Fourier transformation [22]. In order to transform the fields $\mathbf{f}(\mathbf{r}, t)$ we use

$$f(\mathbf{r}, \omega) = \frac{1}{2\pi} \int_{-\infty}^{\infty} \mathrm{d}t \, f(\mathbf{r}, t) \mathrm{e}^{\mathrm{i}\omega t} \quad \Leftrightarrow \quad f(\mathbf{r}, t) = \int_{-\infty}^{\infty} \mathrm{d}\omega \, f(\mathbf{r}, \omega) \mathrm{e}^{-\mathrm{i}\omega t}. \tag{2.7}$$

Thus, in frequency domain the polarization can be written as

$$\mathbf{P}(\mathbf{r}, \omega) = \epsilon_0 \chi^{(1)}(\mathbf{r}, \omega) \mathbf{E}(\mathbf{r}, \omega), \tag{2.8}$$

with the susceptibility in frequency domain as

$$\chi^{(1)}(\mathbf{r},\omega) = \frac{1}{2\pi}\int_{-\infty}^{\infty} \mathrm{d}t\chi^{(1)}(\mathbf{r},t)\mathrm{e}^{\mathrm{i}\omega t}. \tag{2.9}$$

We can introduce the permittivity $\epsilon(\mathbf{r},\omega) = 1 + \chi^{(1)}(\mathbf{r},\omega)$ to relate the electric field directly with the dielectric displacement field. Similar to the expansion of the polarization, the magnetization can be expanded into orders of the magnetic field. The linear dependence between magnetic field and magnetic induction is then described by the permeability μ of the material. As constitutive relations in frequency domain we obtain

$$\mathbf{D}(\mathbf{r},\omega) = \epsilon_0\epsilon(\mathbf{r},\omega)\mathbf{E}(\mathbf{r},\omega), \tag{2.10a}$$
$$\mathbf{B}(\mathbf{r},\omega) = \mu_0\mu(\mathbf{r},\omega)\mathbf{H}(\mathbf{r},\omega). \tag{2.10b}$$

In the optical regime natural materials exhibit nonmagnetic behavior and we can set the magnetization equal to zero throughout this thesis and the permeability $\mu = 1$. This is only valid for natural materials. There is a whole class of new artificial materials, metamaterials, which exhibit a permeability different from one due to sub-wavelength structuring [23].
Because the constitutive relations read easier in frequency domain, we transform Maxwell's curl equations (2.2) also into frequency domain and obtain

$$\nabla\times\mathbf{E}(\mathbf{r},\omega) = \mathrm{i}\omega\mu_0\mathbf{H}(\mathbf{r},\omega), \tag{2.11a}$$
$$\nabla\times\mathbf{H}(\mathbf{r},\omega) = -\mathrm{i}\omega\epsilon_0\epsilon(\mathbf{r},\omega)\mathbf{E}(\mathbf{r},\omega) + \mathbf{J}(\mathbf{r},\omega). \tag{2.11b}$$

These two equations are the foundation of the numerical method we treat in this thesis. Since we do not deal with nonlinearities, the individual frequencies do not couple and the equations can be solved for each frequency independently. In case of no free currents and charges, the divergence equations (2.1) are implicitly fulfilled which can be easily seen by eq. (2.11) if we apply the divergence operator ∇ on the whole curl equations. We directly obtain $\nabla\cdot\mathbf{H} = 0$ and $\nabla\cdot\epsilon\mathbf{E} = 0$. Consequently, the divergence equations do not need to be considered separately. By a Fourier transformation the solution of the fields in time domain can be constructed. In our case, we only consider time-harmonic fields

$$\mathbf{E}(\mathbf{r},t) = \mathbf{E}(\mathbf{r})\mathrm{e}^{-\mathrm{i}\omega t}, \tag{2.12}$$

which only exhibit a time dependence by the oscillating term.

2.2.1. Ordinary Dielectrics

In dielectric materials the polarization field $\mathbf{P}$ is formed by the induced dipole moments of the atoms, that are generated by the applied electric field $\mathbf{E}$. Their strength depends on the polarizability of the atoms in the material. In an isotropic material the polarizability is independent of the direction of the external electric field. Thus, the polarization points always into the same direction as the electric field. Therefore, the permittivity is a scalar. If the response of the material to the applied field is

instantaneous, the permittivity is constant in time. Then, the constitutive relation reads

$$\mathbf{D}(\mathbf{r},t) = \epsilon_0 \epsilon \mathbf{E}(\mathbf{r},t), \tag{2.13}$$

and can be easily written down in time as well as in frequency domain.

2.2.2. Anisotropic Dielectrics

If the polarizability of the material depends on the direction of the electric field vector, ϵ becomes a second rank tensor. As constitutive relation of such an anisotropic material we obtain

$$D_m = \epsilon_0 \sum_n \epsilon_{mn} E_n, \tag{2.14}$$

where we sum over the three field components $n = x, y, z$. D_m and E_n denote the components of the electric displacement and the electric field. Then, the permittivity ϵ possesses nine components. In reciprocal materials the components have to fulfill the condition $\epsilon_{mn} = \epsilon_{nm}$. Thus, only six of these components are independent of each other [20]. Due to the anisotropy, the dielectric displacement field can point in another direction than the electric field vector. In other words, the polarization $\mathbf{P}$ of the material is no longer parallel to the external electric field.

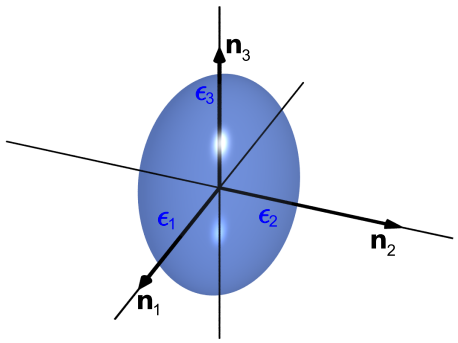

Figure 2.1.: Ellipsoid to visualize the permittivity in the principle coordinate system with the principle axes $\mathbf{n}_1$, $\mathbf{n}_2$, and $\mathbf{n}_3$.

In order to display the permittivity we can use an ellipsoid as in fig. 2.1. In the principle coordinate system of this ellipsoid the three principal axes have different dielectric constants which are the eigenvalues of the ϵ-tensor [24]. The propagation of light through such a material is determined by the direction of the electric field vector. This dependence is called birefringence.
If all three eigenvalues of the permittivity differ, the crystal is biaxial. With two identical eigenvalues the crystal is called uniaxial. In this case, it is characterized by a single optical axis. The last possibility with all three eigenvalues identical brings us back to the isotropic case. This classification is governed mainly by the crystal structure. But anisotropy can also be induced in isotropic crystals by external effects such as deformation or applying of electric (Kerr effect) or magnetic fields (Cotton-Mouton effect), which introduce a direction dependence in the permittivity.

2.2.3. Dispersive Materials

If the permittivity is frequency dependent, the materials are called dispersive and the response of the material is nonlocal in time. The dispersion of a material comes always hand-in-hand with dissipation which is stated by the Kramers-Kronig relation [19]. It relates real and imaginary part of the permittivity to each other. Thus, a dispersive material has a complex permittivity and consequently a complex refractive index, which accounts for dissipation.
In the following, we present two models which describe the light-matter interaction for two different types of materials.

Lorentz Oscillator Model

As already explained, an external electric field induces a dipole moment in the atoms of the material. In the Lorentz model, the atoms are modelled as electron and positive atom core forming an oscillator with a resonance frequency ω_0 and a damping constant γ_L. The external field acts as a driving force on the oscillator and we can set up the equation of motion for the electrons with mass m and charge $-e$ as

$$m\ddot{\mathbf{r}} + m\gamma_\mathrm{L}\dot{\mathbf{r}} + m\omega_0^2\mathbf{r} = -e\mathbf{E}(t). \tag{2.15}$$

We assume an electric field oscillating with frequency ω and amplitude $\mathbf{E}_0$ as $\mathbf{E}(t) = \mathbf{E}_0 \exp(-\mathrm{i}\omega t)$. Therefore, the differential equation can be solved for the position $\mathbf{r}$ by Fourier transformation (2.7). In frequency domain we obtain for the equation of motion

$$-\omega^2\mathbf{r} - \mathrm{i}\omega\gamma_\mathrm{L}\mathbf{r} + \omega_0^2\mathbf{r} = -\frac{e}{m}\mathbf{E}_0, \tag{2.16}$$

and the solution in frequency domain reads

$$\mathbf{r} = \frac{e/m}{\omega^2 + \mathrm{i}\omega\gamma_\mathrm{L} - \omega_0^2}\mathbf{E}_0. \tag{2.17}$$

As consequence the induced dipole moment for one oscillator is $\mathbf{p} = -e\mathbf{r}$. In a further step we can identify the polarizability α of the atom by the relation $\mathbf{p} = \alpha\mathbf{E}$ as

$$\alpha(\omega) = \frac{e^2/m}{\omega_0^2 - \omega^2 - \mathrm{i}\omega\gamma_\mathrm{L}}. \tag{2.18}$$

The contribution of several such dipoles sums up to the polarization $\mathbf{P}(\omega) = n_\mathrm{e}\alpha\mathbf{E}_0$ of the material with electron number density n_e.
In order to obtain the permittivity of such a material, we assume that the density n_e is low, which means in this model we have one electron per atom. Thus, the local field at the dipoles is completely determined by the external electric field since we disregard interaction of the single oscillators between each other. Then, the permittivity can be derived by the relation for the polarization $\mathbf{P} = n_\mathrm{e}\alpha\mathbf{E}_0 = \epsilon_0\chi^{(1)}\mathbf{E}_0$ with the help of the susceptibility in eq. (2.8) as

$$\epsilon_\mathrm{L}(\omega) = \epsilon_\infty + \frac{n_\mathrm{e}e^2}{\epsilon_0 m}\frac{1}{\omega_0^2 - \omega^2 - \mathrm{i}\omega\gamma_\mathrm{L}}. \tag{2.19}$$

Here, we included also a constant background permittivity by ϵ_∞. The second part is a Lorentzian shaped curve which represents the response of the material to an external field around a resonance frequency of an oscillator. This model gives good agreement for systems with atomic transitions in the frequency spectrum. The influence of different atomic transitions can be modeled by adding more Lorentz curves with the respective resonance frequencies to the permittivity. As predicted by the Kramers-Kronig relation the dispersion of the permittivity is accompanied by an imaginary part which causes absorption around the resonance. Real and imaginary part of the permittivity are shown in fig. 2.2.

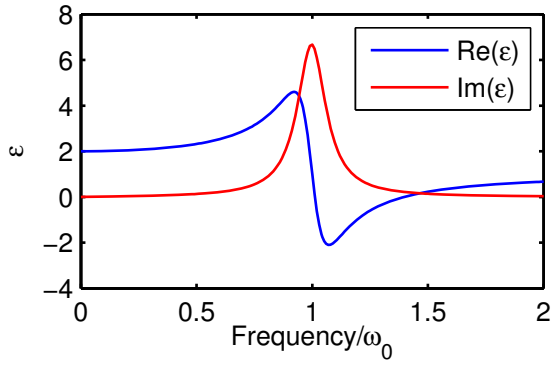

Figure 2.2.: Real and imaginary part of the permittivity in the Lorentz model with $\epsilon_\infty = 1$ and $\gamma_\mathrm{L} = 0.15\omega_0$. The prefactor $n_\mathrm{e}e^2/\epsilon_0 m$ is set equal to ω_0.

Drude Model

In order to obtain an analytical model for the permittivity of metals, we use the so-called Drude model. In this model a metal is described as a material with a positive background charge which is formed by the ions and the free electrons of the metal which can move freely in the whole crystal. To derive the Drude model, we can use the Lorentz model with a few modifications. Since the electrons are no longer bound to the atoms, the restoring force in the Lorentz model vanishes. Formally, we can take care of this by putting the oscillator's resonance frequency ω_0 equal to zero. Thus, we can keep the equation of motion (2.15) and explain the damping phenomenologically. The damping γ_D in the Drude model is also known as the collision frequency. It is the inverse of the mean time between collisions of free electrons.
By regarding the permittivity in the Lorentz model (2.19) with $\omega_0 = 0$ and defining the plasma frequency $\omega_\mathrm{p} = \sqrt{n_\mathrm{e}e^2/\epsilon_0 m}$, we find for the Drude model

$$\epsilon_\mathrm{D}(\omega) = \epsilon_\infty - \frac{\omega_\mathrm{p}^2}{\omega\left(\omega + \mathrm{i}\gamma_\mathrm{D}\right)}. \tag{2.20}$$

Figure 2.3 shows the permittivity in the Drude model. Materials with such a dispersion relation show metallic character for frequencies well below the plasma frequency where the real part of the permittivity is negative. Here, the propagation constant of light

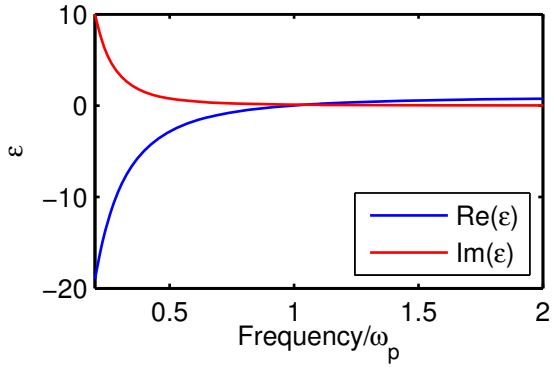

Figure 2.3.: Real and imaginary part of the permittivity in the Drude model with $\epsilon_\infty = 1$ and $\gamma_\mathrm{D} = 0.1\omega_\mathrm{p}$.

obtains a large imaginary part and no propagation over longer distances can take place. Therefore, metals are nontransparent and exhibit a high reflectivity. In the case of $\epsilon_\infty = 1$, the plasma frequency is exactly the frequency at which the real part of the permittivity crosses zero. Above the plasma frequency metals become transparent and behave analogously to dielectrics.
Figure 2.4 shows the experimentally measured data of the permittivity for a gold film [25]. We compare the experimental data with the Drude permittivity. The usual way is to fit the Drude permittivity to the measured one. The plasma frequency, the damping and the background permittivity are used as fit parameters. In the plot, the fitting results of ref. [26] are presented. We can observe that the Drude model is a good description for gold in the infrared, but in the visible spectrum we can detect some deviations. The reason is the interband transitions in gold which are responsible for the

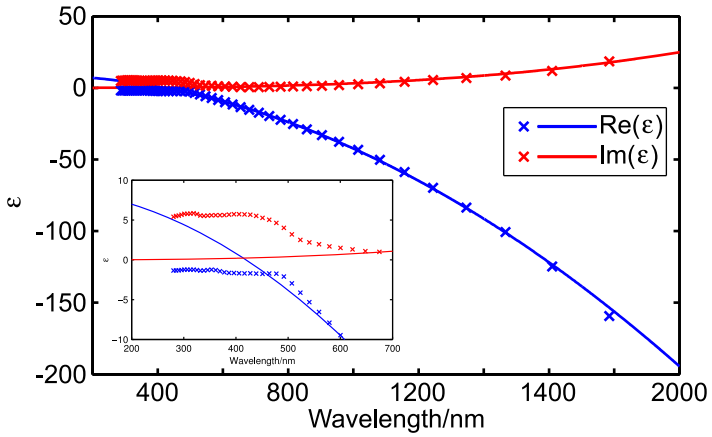

Figure 2.4.: Real and imaginary part of the permittivity for gold plotted over wavelength. The markers show the experimentally measured data by Johnson and Christy [25] and the solid line is the Drude model with parameters $\omega_\mathrm{p} = 1.3544 \times 10^{16}\,\mathrm{s}^{-1}$, $\gamma_\mathrm{D} = 1.1536 \times 10^{14}\,\mathrm{s}^{-1}$ and $\epsilon_\infty = 9.0685$ [26]. The inset shows a zoom into the visible region of the permittivity.

typical yellowish color of gold. The permittivity of such transitions can be explained by the Lorentz model. In order to find a good description for both frequency ranges, the Drude and Lorentz model can be combined to the Drude-Lorentz model [26].

2.3. Reduction to Two Dimensions

In general, we do not need to apply full Maxwell's equations to describe systems exhibiting a translational invariance in one direction. Such systems are considered as two-dimensional. We can orientate the system such that the homogeneous direction is identical to the y-axis. By incidence in the xz-plane, the spatial derivatives of the fields in y-direction are equal to zero. Then, the curl equations (2.2) decouple into two independent sets of equations, if the propagation is restricted to the xz-plane. This splitting is not only valid for isotropic materials but also for anisotropic materials with one principal axis, which corresponds to the y-axis.
The first set is called E-polarization with the electric field pointing in the homogeneous direction

$$-\partial_z E_y = -\partial_t B_x, \tag{2.21a}$$
$$\partial_x E_y = -\partial_t B_z, \tag{2.21b}$$
$$\partial_z H_x - \partial_x H_z = \partial_t D_y, \tag{2.21c}$$

and, respectively, in the second set the magnetic field takes over this role

$$\partial_z E_x - \partial_x E_z = -\partial_t B_y, \tag{2.22a}$$
$$-\partial_z H_y = \partial_t D_x, \tag{2.22b}$$
$$\partial_x H_y = \partial_t D_z. \tag{2.22c}$$

This set of equations represents the H-polarization-case.

2.4. Wave Equation

In this section, we discuss the propagation of light through a transparent medium as in section 2.2.1. For such a material the wave equation can be derived by combining Maxwell's curl equations (2.2). We assume no free currents and charges and obtain the homogeneous wave equation for the electric field

$$\nabla^2 \mathbf{E}(\mathbf{r}, t) + \frac{\epsilon}{c_0^2} \partial_t^2 \mathbf{E}(\mathbf{r}, t) = 0. \tag{2.23}$$

The wave equation for the magnetic field looks the same by exchanging the electric field $\mathbf{E}$ with the magnetic field $\mathbf{H}$. A solution of the wave equation are plane waves

$$\mathbf{E}(\mathbf{r}, t) = \mathbf{E}_0 \mathrm{e}^{\mathrm{i}\mathbf{k}\cdot\mathbf{r} - \mathrm{i}\omega t}, \tag{2.24}$$

with frequency ω and wave vector $\mathbf{k}$. The absolute value of the wave vector k and the frequency are connected via the dispersion relation of this material as

$$\omega = \frac{c_0}{n} k, \tag{2.25}$$

where we introduced the refractive index $n = \sqrt{\epsilon}$ of the material. The field vector $\mathbf{E}_0$ determines the polarization of the wave. For plane waves there are two possible polarization states which span the plane perpendicular to the wave vector. The plane wave possesses also a magnetic field which exhibits the same form as the electric field with the field vector $\mathbf{H}_0$

$$\mathbf{H}(\mathbf{r}, t) = \mathbf{H}_0 \mathrm{e}^{\mathrm{i}\mathbf{k}\cdot\mathbf{r} - \mathrm{i}\omega t}. \tag{2.26}$$

Using eq. (2.2a), we can derive the relation

$$\mathbf{k} \times \mathbf{E}_0 = \mu_0 \omega \mathbf{H}_0 \tag{2.27}$$

to connect the electric and magnetic field vectors.
Since the plane wave solutions form a complete set of basis functions, we can use them to build arbitrary time and space dependent fields by a linear superposition of monochromatic waves as

$$\mathbf{E}(\mathbf{r}, t) = \int_{-\infty}^{\infty} \mathrm{d}^3 k \int_{-\infty}^{\infty} \mathrm{d}\omega \, \mathbf{E}(\mathbf{k}, \omega) \mathrm{e}^{\mathrm{i}\mathbf{k}\cdot\mathbf{r} - \mathrm{i}\omega t}. \tag{2.28}$$

This is also known as the Fourier transform of the electric field $\mathbf{E}(\mathbf{r}, t)$, where the field vector $\mathbf{E}(\mathbf{k}, \omega)$ in the integration is the Fourier space representation of the electric field in time and space.
In addition to the propagating plane waves with real wave vector which have been discussed in the previous, there is also another class of waves which is called evanescent waves. Formally, they can be described by a plane wave as in eq. (2.24), but their wave vector is imaginary. Thus, they are exponentially decaying. Evanescent waves do not transport energy but give an important contribution to near field effects.
In dispersive materials with complex permittivity, the plane wave solution consists of an oscillatory and an evanescent part. These waves can only propagate a finite distance until they are completely absorbed by the medium.

2.5. Poynting's Theorem

With the help of Maxwell's curl equations (2.2) we can also derive Poynting's theorem [27]

$$\partial_t w + \nabla \cdot \mathbf{S} = -\mathbf{J} \cdot \mathbf{E}. \tag{2.29}$$

In this equation two new quantities are defined. The energy density of the electromagnetic field reads

$$w = \mathbf{E} \cdot \partial_t \mathbf{D} + \mathbf{H} \cdot \partial_t \mathbf{B}, \tag{2.30}$$

and the Poynting vector

$$\mathbf{S} = \mathbf{E} \times \mathbf{H} \tag{2.31}$$

is the energy flux of an electromagnetic field which is the amount of energy propagating per time unit through a unit area normal to the direction of $\mathbf{E}$ and $\mathbf{H}$. The Poynting theorem describes the conservation of energy for electromagnetic fields, where the term on the right-hand side is the work of the electric field on the sources.

By integrating over a volume V and applying Gauss' theorem, we obtain the integral form of the Poynting theorem

$$\int_V \mathrm{d}V\, \partial_t w + \int_{\partial V} \mathrm{d}A\, \mathbf{n}\cdot\mathbf{S} = -\int_V \mathrm{d}V\, \mathbf{J}\cdot\mathbf{E}, \tag{2.32}$$

with the normal vector $\mathbf{n}$ on the closed surface ∂V of the volume V. In this representation of the Poynting theorem, it can be seen that it describes the conservation of energy for electromagnetic fields in the volume V. The term on the right-hand side is the work of the electric field on external currents contained in the volume whereas the left-hand side is determined by the macroscopic fields. The first term on the left-hand side describes the change of the energy stored in the fields. Here, also dispersive materials contribute which are time dependent as seen in the general constitutive relation (2.6). The dispersion gives a contribution of the material to the energy density by the imaginary part of the permittivity which acts as absorber or radiator of energy [19]. The second term is the integrated Poynting vector over the surface which presents the power radiated out of or into the volume V. Thus, the power of the electromagnetic field can be defined as

$$P = \int_{\partial V} \mathrm{d}A\, \mathbf{n}\cdot\mathbf{S}, \tag{2.33}$$

which is the amount of energy flowing through the surface per unit time.
If we consider time-harmonic fields, we are no longer interested in the Poynting vector as defined in eq. (2.31), but rather use the time-averaged Poynting vector defined as

$$<\mathbf{S}>= \frac{1}{2}\mathrm{Re}\left(\mathbf{E}\times\mathbf{H}^*\right), \tag{2.34}$$

where the asterisk * denotes the complex conjugate. If we talk about the Poynting flux later, we use this expression. In the case of the plane waves, introduced in the previous section, the Poynting flux is $<\mathbf{S}>= \frac{1}{2\mu_0\omega}\left|\mathbf{E}_0\right|^2\mathbf{k}$.

2.6. Electromagnetic Waves at Boundaries

Until now, we considered only the interaction of light with a single material. If we have a second material in the system, we have to create an interface between these two media. By means of Maxwell's equations the behavior of the fields at material interfaces is obtained with the help of Gauss' and Stokes' theorem [19]. Let us investigate an interface between material 1 and material 2 with normal vector $\mathbf{n}$. Then, the components of the electric and magnetic fields tangential to the surface are related by

$$\mathbf{n}\times(\mathbf{E}_1-\mathbf{E}_2) = 0, \tag{2.35}$$
$$\mathbf{n}\times(\mathbf{H}_1-\mathbf{H}_2) = \mathbf{J}_\mathrm{s}, \tag{2.36}$$

where $\mathbf{J}_\mathrm{s}$ denotes the surface current density. The subscripts denote the fields in the respective materials. The normal field components of the dielectric displacement field and magnetic induction are given on both sides of the boundary as

$$\mathbf{n}\cdot(\mathbf{D}_1-\mathbf{D}_2) = \sigma, \tag{2.37}$$
$$\mathbf{n}\cdot(\mathbf{B}_1-\mathbf{B}_2) = 0, \tag{2.38}$$

with the surface charge density σ. These relations show that in systems without free charges and currents the tangential components of the electric and magnetic field are continuous such as the normal components of the magnetic inductance and the dielectric displacement. In this case, we can also specify exactly the jump discontinuity of the normal components of the electric field at the material interface between isotropic materials as

$$\mathbf{n} \cdot \mathbf{E}_1 = \frac{\epsilon_2}{\epsilon_1} \mathbf{n} \cdot \mathbf{E}_2. \tag{2.39}$$

With this knowledge we can determine analytically exact the behavior of an incident plane wave impinging onto a planar material interface.

Reflectance and Transmittance

If we consider a linearly polarized plane wave which is incident on a planar interface at $z = 0$, one part of the incident wave is reflected and the other part is transmitted. The situation is sketched in fig. 2.5. Since the materials are assumed to be isotropic and homogeneous, we can use a plane wave ansatz to describe the reflected and transmitted wave, as well. In medium 1 with refractive index $n_1 = \sqrt{\epsilon_1}$ ($z < 0$) the electric field with the incident and reflected part is

$$\mathbf{E}_1(\mathbf{r}, t) = \mathbf{E}_{0,\text{in}} \mathrm{e}^{\mathrm{i}\mathbf{k}_{\text{in}} \cdot \mathbf{r} - \mathrm{i}\omega t} + \mathbf{E}_{0,\text{refl}} \mathrm{e}^{\mathrm{i}\mathbf{k}_{\text{refl}} \cdot \mathbf{r} - \mathrm{i}\omega t} \tag{2.40}$$

and the transmitted wave in medium 2 with $n_2 = \sqrt{\epsilon_2}$ for $z > 0$ is

$$\mathbf{E}_2(\mathbf{r}, t) = \mathbf{E}_{0,\text{trans}} \mathrm{e}^{\mathrm{i}\mathbf{k}_{\text{trans}} \cdot \mathbf{r} - \mathrm{i}\omega t}. \tag{2.41}$$

The same equations can be set up for the corresponding magnetic fields which are related to the electric fields by eq. (2.27). The magnitudes of the wave vectors in the different materials are $k_{\text{in}} = k_{\text{refl}} = \omega n_1 / c_0$ and $k_{\text{trans}} = \omega n_2 / c_0$. As the tangential

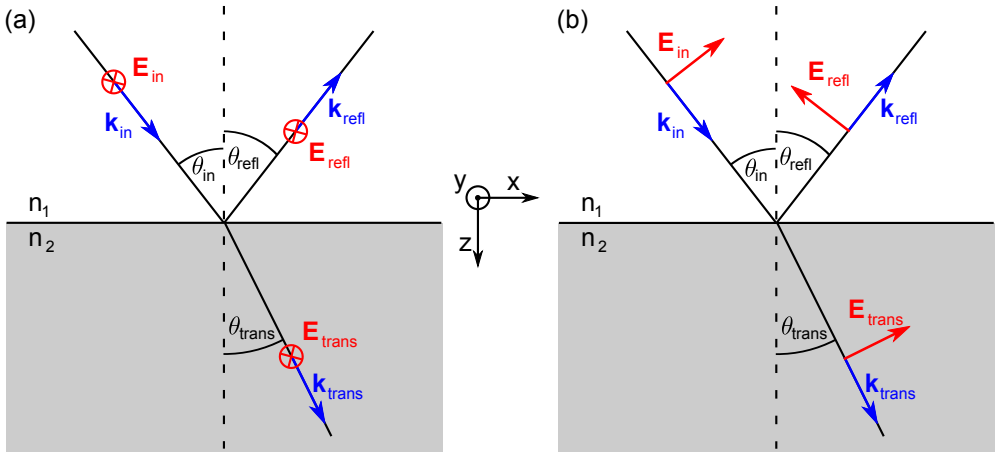

Figure 2.5.: Reflection and refraction of a plane wave at a planar interface for the case of (a) s-polarization and (b) p-polarization.

components of the electric field have to be continuous at all points on the interface, the phase factors of the three plane waves have to be the same,

$$(\mathbf{k}_{\text{in}} \cdot \mathbf{r})_{z=0} = (\mathbf{k}_{\text{refl}} \cdot \mathbf{r})_{z=0} = (\mathbf{k}_{\text{trans}} \cdot \mathbf{r})_{z=0}. \tag{2.42}$$

With this relation we obtain, on the one hand, that the angle of incidence θ_{in} and the angle of the reflected light θ_{refl} are identical. On the other hand, we obtain Snell's law which gives the refraction of the transmitted light at the interface

$$n_1 \sin\theta_{\text{in}} = n_2 \sin\theta_{\text{trans}}. \tag{2.43}$$

The amount of the reflected and transmitted light does not only depend on the incident angle but also on the polarization of the incident plane wave. We distinguish between s- and p-polarized light: The electric field vector of an s-polarized plane wave (also TE: transversal electric) points perpendicular to the plane of incidence, which is spanned by the wave vector of the incident wave and the normal vector to the interface. Accordingly, p-polarized light (also TM: transversal magnetic) has an electric field vector lying in the plane of incidence. Thus, we can decompose the arbitrarily polarized incident wave into a s- and p-polarized wave which can be treated separately. Both cases are illustrated in fig. 2.5.
Applying the boundary conditions for the electric and magnetic field, we can derive the Fresnel equations. These express the reflection coefficient r and transmission coefficient t of the field amplitudes for the two polarizations [24, 28]. In case of s-polarization, we obtain

$$r_{\text{s}} = \frac{E_{0,\text{refl}}}{E_{0,\text{in}}} = \frac{n_2 \cos\theta_{\text{trans}} - n_1 \cos\theta_{\text{in}}}{n_1 \cos\theta_{\text{in}} + n_2 \cos\theta_{\text{trans}}}, \tag{2.44}$$

$$t_{\text{s}} = \frac{E_{0,\text{trans}}}{E_{0,\text{in}}} = \frac{2n_1 \cos\theta_{\text{in}}}{n_1 \cos\theta_{\text{in}} + n_2 \cos\theta_{\text{trans}}}, \tag{2.45}$$

and, in case of p-polarization,

$$r_{\text{p}} = \frac{E_{0,\text{refl}}}{E_{0,\text{in}}} = \frac{\epsilon_1 n_2 \cos\theta_{\text{trans}} - \epsilon_2 n_1 \cos\theta_{\text{in}}}{\epsilon_1 n_2 \cos\theta_{\text{in}} + \epsilon_2 n_1 \cos\theta_{\text{trans}}}, \tag{2.46}$$

$$t_{\text{p}} = \frac{E_{0,\text{trans}}}{E_{0,\text{in}}} = \frac{2\epsilon_2 n_1 \cos\theta_{\text{in}}}{\epsilon_2 n_1 \cos\theta_{\text{in}} + \epsilon_1 n_2 \cos\theta_{\text{trans}}} \sqrt{\frac{\epsilon_1}{\epsilon_2}}. \tag{2.47}$$

The field directions can be deduced from fig. 2.5. The coefficients are also valid for incidence on a material with complex permittivity. In that case, the transmitted waves decay.
In order to determine the amount of energy which is reflected and transmitted, the reflectance R and transmittance T are defined. They depict the ratio between the reflected/transmitted power and the incident power. We calculate the power by eq. (2.33). Since we consider only plane waves, we can replace the Poynting vector by the time-averaged Poynting vector (2.34). As volume V we choose a box around the interface with faces parallel to the material interface as shown in fig. 2.6. Thus, we only have to calculate the flux through the top and bottom area, since the contributions from

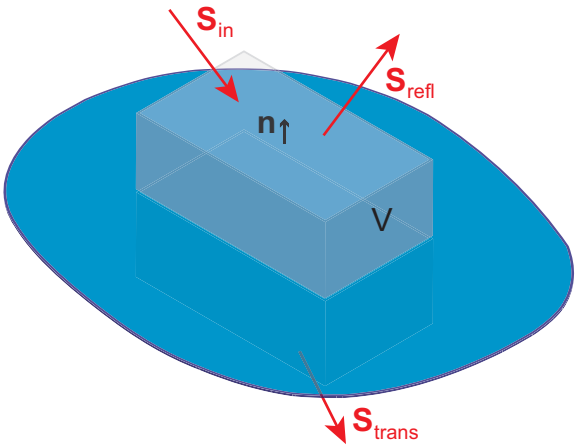

Figure 2.6.: Box with volume V for integration around the interface to determine the incident, reflected and transmitted electromagnetic power. The red arrows denote the Poynting flux in and out of the box.

the other faces cancel each other. Therefore, we only need the z-component of the Poynting vector. The height of the box is not important for us since we consider here the transmittance and reflectance for materials with purely real refractive indices. We obtain

$$R = \frac{P_{\text{refl}}}{P_{\text{in}}} = |r|^2, \tag{2.48a}$$

$$T = \frac{P_{\text{trans}}}{P_{\text{in}}} = \frac{n_2 \cos\theta_{\text{trans}}}{n_1 \cos\theta_{\text{in}}} |t|^2. \tag{2.48b}$$

In this system we do not have absorption. Thus, the energy is conserved. This is expressed by the condition

$$R + T = 1, \tag{2.49}$$

which is always fulfilled for both polarizations and follows directly from the Poynting theorem (2.32).
We discuss briefly two effects which can occur for reflectance and transmittance at an interface. With Snell's law we can directly obtain, that in the case of incidence from an optically denser material ($n_1 > n_2$) there is no transmittance for too large angles of incidence. Then, the transmitted electric field is evanescent. This effect is called total internal reflection and the critical angle can be directly derived from eq. (2.43) as $\theta_c = \arcsin \frac{n_2}{n_1}$.
A polarization dependent effect in reflection is the Brewster angle

$$\theta_B = \arctan \frac{n_2}{n_1}. \tag{2.50}$$

If the incidence angle is equal to θ_B and the plane wave is p-polarized, the reflection is equal to zero. Since the angle between reflected and transmitted light is exactly 90°, the electric dipoles which are excited at the boundary cannot radiate energy in the direction of the reflection. Thus, light propagation for p-polarization along this

direction is totally suppressed. Arbitrarily polarized light impinging at the Brewster angle will be purely s-polarized in reflection. This effect can be used for polarization filters.

2.7. Maxwell's Equations in Covariant Formulation

Since Maxwell's equations state the fundamental laws in electromagnetism, they are valid independently of the coordinate system we use to describe physics. This means, we can write Maxwell's equations in a mathematical form which is invariant under coordinate transformations. This property is called covariance. Later in this thesis, we want to use Maxwell's equations in curvilinear coordinates. Thus, we give a short introduction to curvilinear coordinates, here.

2.7.1. Curvilinear Coordinates

In our case, the starting point is always the Cartesian coordinate system $Oxyz$ which is called $O\bar{x}^1\bar{x}^2\bar{x}^3$, here. The Cartesian system is spanned by the basis vectors $\bar{\mathbf{b}}_1$, $\bar{\mathbf{b}}_2$ and $\bar{\mathbf{b}}_3$. A vector in this system is described by its components $\bar{x}^1$, $\bar{x}^2$ and $\bar{x}^3$ as

$$\mathbf{r} = \bar{x}^i \bar{\mathbf{b}}_i, \tag{2.51}$$

where we assume Einstein's sum convention with summation over upper and lower index $i = 1, 2, 3$.
With the help of a coordinate transformation, we change to the curvilinear coordinate system $Ox^1x^2x^3$. This is connected to the Cartesian system by

$$\bar{x}^1 = \bar{x}^1(x^1, x^2, x^3), \tag{2.52a}$$
$$\bar{x}^2 = \bar{x}^2(x^1, x^2, x^3), \tag{2.52b}$$
$$\bar{x}^3 = \bar{x}^3(x^1, x^2, x^3). \tag{2.52c}$$

As requirement the coordinate transformation has to be locally invertible at each point. With a covariant transformation we can derive the basis vectors $\mathbf{b}_i$ in the curvilinear space as [19]

$$\mathbf{b}_i = \frac{\partial \bar{x}^k}{\partial x^i} \bar{\mathbf{b}}_k. \tag{2.53}$$

Due to this transformation the basis vectors with lower index are called covariant basis vectors. They are tangents on the coordinate curves which is illustrated in fig. 2.7 for a two-dimensional system. With the covariant derivative $\partial_i = \partial/\partial x^i$ the covariant basis vectors in the curvilinear coordinate can also be written as $\mathbf{b}_i = \partial_i \mathbf{r}$.
In general, the covariant basis vectors are used to span the real space of the system. In addition to the covariant basis vectors there are also the contravariant basis vectors which span the dual space. In our case, the dual space is identical to the reciprocal space. The contravariant basis vectors, written with upper index, can be calculated by the relations

$$\mathbf{b}^1 = \frac{\mathbf{b}_2 \times \mathbf{b}_3}{|J|}, \quad \mathbf{b}^2 = \frac{\mathbf{b}_3 \times \mathbf{b}_1}{|J|}, \quad \mathbf{b}^3 = \frac{\mathbf{b}_1 \times \mathbf{b}_2}{|J|}. \tag{2.54}$$

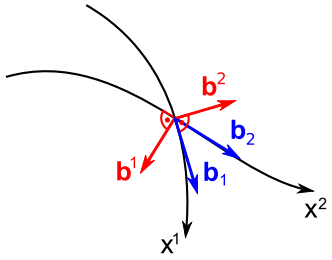

Figure 2.7.: Covariant basis vectors (blue) and contravariant basis vectors (red) in a two-dimensional curvilinear system. The curvilinear coordinate lines are plotted in the Cartesian system.

J is the Jacobian matrix, which contains the first-order partial derivatives of the coordinates

$$J = \frac{\partial(\bar{x}^1, \bar{x}^2, \bar{x}^3)}{\partial(x^1, x^2, x^3)} = \begin{pmatrix} \partial_1\bar{x}^1 & \partial_2\bar{x}^1 & \partial_3\bar{x}^1 \\ \partial_1\bar{x}^2 & \partial_2\bar{x}^2 & \partial_3\bar{x}^2 \\ \partial_1\bar{x}^3 & \partial_2\bar{x}^3 & \partial_3\bar{x}^3 \end{pmatrix}, \tag{2.55}$$

and the determinant can be calculated directly by $|J| = \mathbf{b}_1 \cdot (\mathbf{b}_2 \times \mathbf{b}_3)$. The determinant is never equal to zero since we demand that the coordinate transformation is invertible. Thus, we obtain the reciprocal relation $\mathbf{b}^i\mathbf{b}_j = \delta^i_j$, where δ^i_j is the Kronecker delta symbol.
From this, we can easily deduce that the contravariant basis vectors are normal on the coordinate surfaces as shown in fig. 2.7. In the Cartesian system this means that the covariant and contravariant basis vectors are identical. The transformation behavior of the contravariant basis vectors differs from the covariant basis vectors

$$\mathbf{b}^i = \frac{\partial x^i}{\partial \bar{x}^k}\bar{\mathbf{b}}^k = \nabla x^i, \tag{2.56}$$

with the gradient ∇ in Cartesian space. This type of transformation is called contravariant.
The components of a vector in the covariant basis transform in contravariant manner and are denoted by upper index. Correspondingly, the covariant vector components are paired with contravariant basis vectors. For completeness, we state here also the transformation of the co- and contravariant vector components

$$F_i = \frac{\partial \bar{x}^k}{\partial x^i}\bar{F}_k \quad \text{and} \quad F^i = \frac{\partial x^i}{\partial \bar{x}^k}\bar{F}^k. \tag{2.57}$$

The vector $\mathbf{F}$ can be presented in two ways as

$$\mathbf{F} = F^i\mathbf{b}_i = F_i\mathbf{b}^i. \tag{2.58}$$

The contravariant components are the projections of the vector $\mathbf{F}$ onto the respective contravariant basis vectors $F^i = \mathbf{F} \cdot \mathbf{b}^i$. The same is valid for the covariant components by $F_i = \mathbf{F} \cdot \mathbf{b}_i$.

In order to change between the co- and contravariant formulation one can define a metric for the coordinate system by

$$F^i = g^{ij} F_j. \tag{2.59}$$

The metric in Cartesian space is a unit matrix. In the curvilinear system, the metric can be calculated in co- and contravariant formulation by

$$g_{ij} = \frac{\partial \bar{x}^k}{\partial x^i} \frac{\partial \bar{x}^l}{\partial x^j} \bar{g}_{kl} = \mathbf{b}_i \mathbf{b}_j, \tag{2.60a}$$

$$g^{ij} = \frac{\partial x^i}{\partial \bar{x}^k} \frac{\partial x^j}{\partial \bar{x}^l} \bar{g}^{kl} = \mathbf{b}^i \mathbf{b}^j. \tag{2.60b}$$

The contravariant metric is the inverse of the covariant metric $g_{ij} g^{jk} = \delta_i^k$ and the determinant is $|g_{ij}| = g = |J|^2$.
From now on we try to formulate the problems with the co- and contravariant basis vectors. The Cartesian coordinates $Oxyz$ are always used as reference system to give a simplified view on the presented problem.

2.7.2. Maxwell's Equations

Now, we want to re-write Maxwell's equations (2.1) and (2.2) in the co- and contravariant formalism. We obtain [29]

$$\partial_i D^i = \rho, \tag{2.61a}$$

$$\partial_i H^i = 0, \tag{2.61b}$$

$$\xi^{ijk} \partial_j E_k = -\partial_t B^i, \tag{2.61c}$$

$$\xi^{ijk} \partial_j H_k = \partial_t D^i + J^i, \tag{2.61d}$$

with the Levi-Civita tensor ξ. In this form, Maxwell's equations are invariant under general coordinate transformations in space. In the curl equations, the electric and magnetic field components transform covariantly. In contrast, the components of the dielectric displacement and magnetic induction are contravariant in their transformation behavior.
The linear constitutive relations in general curvilinear coordinates are

$$B^i = \mu_0 \mu^{ij} H_j, \tag{2.62a}$$

$$D^i = \epsilon_0 \epsilon^{ij} E_j. \tag{2.62b}$$

The tensors ϵ^{ij} and μ^{ij} for permittivity and permeability in the curvilinear space do not only depend on the medium as in section 2.2 but also on the geometry of the problem. They are defined in general coordinates for an anisotropic material in the Cartesian space, $\bar{\epsilon}^{kl}$ and $\bar{\mu}^{kl}$, as

$$\epsilon^{ij} = \sqrt{g} \frac{\partial x^i}{\partial \bar{x}^k} \frac{\partial x^j}{\partial \bar{x}^l} \bar{\epsilon}^{kl}, \tag{2.63a}$$

$$\mu^{ij} = \sqrt{g} \frac{\partial x^i}{\partial \bar{x}^k} \frac{\partial x^j}{\partial \bar{x}^l} \bar{\mu}^{kl}. \tag{2.63b}$$

As indicated by the upper indices at the permittivity and permeability tensors, they transform contravariantly [30]. In order to keep the original form of Maxwell's equations in the curvilinear coordinate system we let them absorb the factor $\sqrt{g}$.
For isotropic media in the Cartesian system we can assume $\bar{\epsilon}^{ij} = \bar{\epsilon}\delta^{ij}$ and $\bar{\mu}^{ij} = \bar{\mu}\delta^{ij}$. Then, we obtain for the permittivity and permeability in the transformed space

$$\epsilon^{ij} = \sqrt{g}\bar{\epsilon}g^{ij}, \tag{2.64a}$$
$$\mu^{ij} = \sqrt{g}\bar{\mu}g^{ij}, \tag{2.64b}$$

with the contravariant metric tensor (2.60b).
Thus, we simply have to consider Maxwell's equations with anisotropic materials in the curvilinear coordinates. The coordinate information is completely absorbed in the permittivity and permeability. Also with permittivity in real space $\bar{\mu} = 1$ we obtain a permeability which is anisotropic.
The property of the coordinate transformation is used the other way round in transformation optics, which is the basis for cloaking. Here one intends to influence the path of light through a system by using appropriate material distributions. The desired path can be translated into new coordinates such that the light is propagating straight in this new coordinate system. However, in the original coordinates it travels the desired path. In the case of cloaking, the light is bent around an object. These new coordinates are curvilinear coordinates and can be realized by creation of the corresponding anisotropic material [9, 10]. In this material the light is passed around an object such that the observer cannot see the object because he "is looking around" this object.
In order to complete the treatment of Maxwell's equations in curvilinear coordinates we also state the curl equations with harmonic time dependence for the fields (2.11) and without free sources and currents [30]

$$\xi^{ijk}\partial_j E_k = \mathrm{i}\omega\mu_0\mu^{ij}H_j, \tag{2.65a}$$
$$\xi^{ijk}\partial_j H_k = -\mathrm{i}\omega\epsilon_0\epsilon^{ij}E_j. \tag{2.65b}$$

Later, we use Maxwell's equations for materials with anisotropic permeability and permittivity, to keep the formulation independent of the coordinate system.

2.8. Optics in Periodic Systems

Since we treat in this thesis periodic structures, we give a short introduction into some properties which refer to the periodicity of the system. In our case, the periodicity occurs in the permittivity distribution as

$$\epsilon(\mathbf{r}) = \epsilon(\mathbf{r} + \mathbf{R}), \tag{2.66}$$

with the lattice vector

$$\mathbf{R} = l_1 d_1 \mathbf{b}_1 + l_2 d_2 \mathbf{b}_2 + l_3 d_3 \mathbf{b}_3, \quad l_i = 0, \pm 1, \pm 2, \ldots. \tag{2.67}$$

The basis vectors of the real space $\mathbf{b}_i$ are the covariant basis vectors (2.53) as already mentioned in the previous section. Together with the lattice constants d_i for the three

spatial directions, they represent the lattice. The smallest unit cell of the lattice is given by the Wigner-Seitz cell [31]. Thus, we only need the permittivity distribution in this cell (or another cell with the same size) to describe the whole system. The cell can be further reduced by the symmetry of the permittivity distribution in the unit cell and the lattice.
In fig. 2.8, the basis vectors in a nonrectangular lattice are shown together with the corresponding reciprocal lattice.

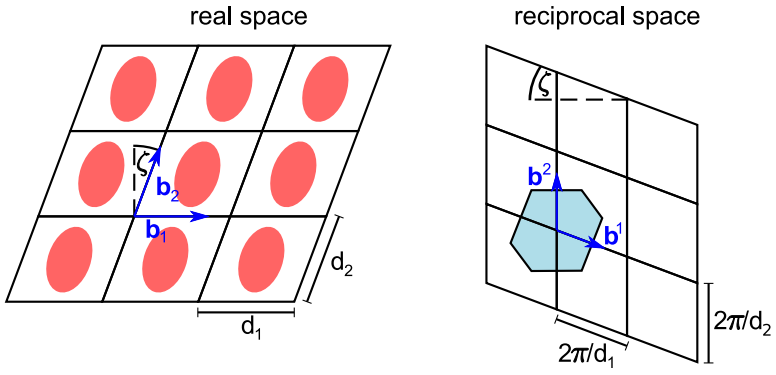

Figure 2.8.: Real space (left) and reciprocal space (right) for a two-dimensional periodic system with a nonrectangular lattice. The angle ζ denotes the angle which the nonrectangular system forms with the Cartesian coordinate system. In the reciprocal space the first Brillouin zone is depicted by the light blue area.

The reciprocal lattice is described by the reciprocal lattice vectors

$$\mathbf{G} = m_1 \frac{2\pi}{d_1}\mathbf{b}^1 + m_2 \frac{2\pi}{d_2}\mathbf{b}^2 + m_3 \frac{2\pi}{d_3}\mathbf{b}^3, \quad m_i = 0, \pm 1, \pm 2, \ldots \tag{2.68}$$

with the contravariant basis vectors $\mathbf{b}^i$ (2.56). The primitive unit cell in the reciprocal lattice is called the first Brillouin zone (FBZ, see fig. 2.8) and is constructed in the same way as the Wigner-Seitz cell in the real space lattice. The unit cells in both spaces are reciprocal to each other. The larger the real space unit cell is, the smaller is the first Brillouin zone.
Real space and reciprocal space are connected by a Fourier transformation. Thus, we can easily switch between these two spaces. As consequence, we can give the permittivity of the system (2.66) also in the reciprocal space by a Fourier transformation on the lattice

$$\epsilon_m = \frac{1}{d_1 d_2 d_3} \int_0^{d_1} \mathrm{d}x^1 \int_0^{d_2} \mathrm{d}x^2 \int_0^{d_3} \mathrm{d}x^3 \, \epsilon(x^1, x^2, x^3) \mathrm{e}^{-\mathrm{i}\left(m_1 \frac{2\pi}{d_1} x^1 + m_2 \frac{2\pi}{d_2} x^2 + m_3 \frac{2\pi}{d_3} x^3\right)}, \tag{2.69}$$

where we denote by the index m a reciprocal lattice point which is described by the triple $\{m_1, m_2, m_3\}$. Correspondingly, we have to sum over all reciprocal lattice points to perform the back transformation

$$\epsilon(x^1, x^2, x^3) = \sum_m \epsilon_m \mathrm{e}^{\mathrm{i}\left(m_1 \frac{2\pi}{d_1} x^1 + m_2 \frac{2\pi}{d_2} x^2 + m_3 \frac{2\pi}{d_3} x^3\right)}. \tag{2.70}$$

The periodic permittivity is the basis in the theory of photonic crystals and gratings. These systems are investigated in detail in this thesis. However, for performing numerical calculations we use only properties of the periodicity in two dimensions. In the next section, we recall the general form of eigensolutions in periodic systems such as reflectance and transmittance properties.

2.8.1. Bloch Theorem

The wave propagation in periodic media can be compared with solutions of the Schrödinger equation in periodic potentials [31]. Due to the translational symmetry of the problem, the wave functions $\psi_{\mathbf{k}}(\mathbf{r})$ exhibit the same periodicity up to a phase factor. This is stated in the Bloch theorem for a wave function $\psi_{\mathbf{k}}(\mathbf{r})$

$$\psi_{\mathbf{k}}(\mathbf{r}) = \mathrm{e}^{\mathrm{i}\mathbf{k}\cdot\mathbf{r}} u_{\mathbf{k}}(\mathbf{r}), \tag{2.71}$$

with the lattice periodic function $u_{\mathbf{k}}(\mathbf{r}) = u_{\mathbf{k}}(\mathbf{r}+\mathbf{R})$ and the plane wave envelope function with the wave vector $\mathbf{k}$. Together, they form the Bloch wave. In contrast to the case of plane waves, the wave vector is restricted to the first Brillouin zone, since it can always be back-folded by the reciprocal lattice vector $\mathbf{G}$ as defined in eq. (2.68). Thus, the system can be completely characterized by the solutions in the first Brillouin zone. By the Bloch theorem we obtain the relation

$$\psi_{\mathbf{k}+\mathbf{G}}(\mathbf{r}) = \psi_{\mathbf{k}}(\mathbf{r}). \tag{2.72}$$

Another formulation of the Bloch theorem is

$$\psi_{\mathbf{k}}(\mathbf{r}+\mathbf{R}) = \psi_{\mathbf{k}}(\mathbf{r})\mathrm{e}^{\mathrm{i}\mathbf{k}\mathbf{R}}, \tag{2.73}$$

which shows that the wave function at two points connected by a lattice vector $\mathbf{R}$ only differ in a phase factor. This means, that the intensity distribution $\propto |\psi|^2$ shows the same periodicity as the system.

2.8.2. Diffraction

In section 2.6, we described the reflectance and transmittance behavior of a plane wave on a planar interface between two homogeneous materials. Now, we modify the problem and add a periodic structure between the two materials as illustrated in fig. 2.9. The structured region shall exhibit periodicity in a plane which is oriented parallel to the surface. This situation corresponds to a diffraction grating between two homogeneous half-spaces which are called the superstrate with refractive index n_1 and the substrate with n_2. Due to the periodicity, the boundary condition for the parallel components of wave vector (2.42) is conserved up to a reciprocal lattice vector $\mathbf{G}$. Hence, we do not only have one single plane wave in reflection and not only one in transmittance. The reflected and transmitted wave split up in several diffraction orders which are called Bragg orders or spatial harmonics. The same effect can also be observed in crystal optics where X-rays are diffracted by the crystal lattice. In order to see this effect, the lattice constant has to be of the same order as the wavelength of the incident light.

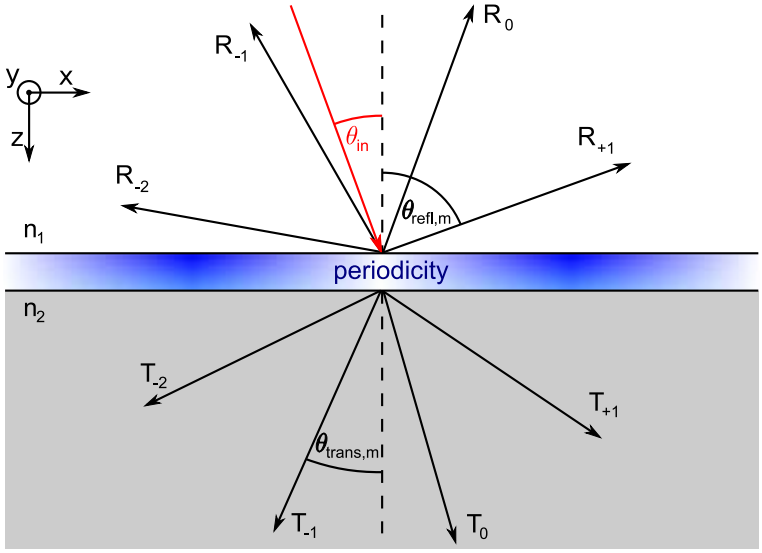

Figure 2.9.: Reflectance and transmittance on a periodic plane. The incident light is marked red and impinges with the angle θ_{in} to the normal on the periodic plane. The reflected and transmitted diffraction orders are presented by black arrows.

Since we know the periodicity and the vacuum wavelength of the incident plane wave λ_0, we can determine the reflected and transmitted orders analytically. In general we consider gratings with two-dimensional periodicity and the periodic plane is described with the basis vectors $\mathbf{b}_1$ and $\mathbf{b}_2$ as shown in fig. 2.8. Such gratings are known as crossed gratings, and gratings with only one-dimensional periodicity are called lamellar gratings.
The light impinges on the grating with the wave vector $\mathbf{k}_{\text{in}} = \alpha_0\mathbf{b}^1 + \beta_0\mathbf{b}^2 + \gamma_0\mathbf{b}^3$. Since the tangential components have to be conserved up to reciprocal lattice vectors, we can write the first and second component of the transmitted and reflected wave vector by

$$\alpha_{m_1} = \alpha_0 + m_1\frac{2\pi}{d_1}, \tag{2.74a}$$

$$\beta_{m_2} = \beta_0 + m_2\frac{2\pi}{d_2}. \tag{2.74b}$$

The factors $m_1 = 0, \pm1, \pm2, \ldots$ and $m_2 = 0, \pm1, \pm2, \ldots$ determine the possible diffraction order. The third component of the wave vectors can be determined by the equation

$$g^{ij}k_ik_j = \left(\frac{2\pi n}{\lambda_0}\right)^2, \tag{2.75}$$

which states that the frequency of the diffracted waves does not change. n is the refractive index of either the superstrate or substrate. The covariant components k_i are only used for short notation and are simply the components of the wave vector. The condition has to be fulfilled by each diffracted wave with $k_1 = \alpha_{m_1}$, $k_2 = \beta_{m_2}$ and $k_3 = \gamma_{m=\{m_1,m_2\}}$. Thus, we obtain a finite number of diffracted waves which have a

purely real third component. The others are purely imaginary and describe evanescent waves.
Then, the electric field can be expressed by the Rayleigh expansion [32] in the superstrate

$$\mathbf{E}_1(\mathbf{r},t) = \mathbf{E}_{\text{in}} \mathrm{e}^{\mathrm{i}\alpha_0 x^1 + \mathrm{i}\beta_0 x^2 + \mathrm{i}\gamma_0 x^3 - \mathrm{i}\omega t} + \sum_{m=\{m_1,m_2\}} \mathbf{E}_{\text{refl},m} \mathrm{e}^{\mathrm{i}\alpha_{m_1} x^1 + \mathrm{i}\beta_{m_2} x^2 - \mathrm{i}\gamma_m x^3 - \mathrm{i}\omega t} \tag{2.76}$$

and the substrate

$$\mathbf{E}_2(\mathbf{r},t) = \sum_{m=\{m_1,m_2\}} \mathbf{E}_{\text{trans},m} \mathrm{e}^{\mathrm{i}\alpha_{m_1} x^1 + \mathrm{i}\beta_{m_2} x^2 + \mathrm{i}\gamma_m x^3 - \mathrm{i}\omega t}. \tag{2.77}$$

By the summation over the pairs $m = \{m_1, m_2\}$, all reciprocal lattice vectors in the two-dimensional space are included. The sum is not limited and thus the expansion contains all propagating and evanescent waves which can be excited due to the lattice effect. The number of propagating plane waves in the homogeneous regions depends on the ratio between wavelength and lattice constant as well as on the material of the super- or substrate. In the wavelength region $\lambda_0 > n d_i$ with lattice constant $d_i, i = 1, 2$ there exists no diffraction for perpendicular incidence on the grating. The smaller the wavelength in comparison to the lattice constant becomes, the more diffraction orders can be observed.
By changing the wavelength continuously, diffraction orders can vanish or appear in transmittance and reflectance. Exactly, at the wavelengths where new diffraction orders appear a resonance can be observed in the spectrum which is known as Rayleigh anomaly (or also Wood's anomaly) [33]. It is explained by the redistribution of the energy into another number of propagating modes.
The transmittance T_n and reflectance R_n into the different diffraction orders, as indicated in fig. 2.9, can be calculated similar to the transmittance and reflectance in section 2.6 on a planar interface. There, we obtained only one reflected and transmitted plane wave. Nevertheless, we can also apply eqs. (2.48) to each reflected and transmitted diffraction order separately, since each diffraction order is a plane wave. Thus, the sum over all propagating orders is $\sum_n T_n + R_n = 1$ in the case of non-absorbing systems.
Photonic crystals can be considered as diffraction gratings which exhibit additional periodicity in the permittivity in the third direction. Thus, also the transmitted and reflected field of a photonic crystal can be described by the Rayleigh expansion. However, the strength of the reflected and transmitted fields cannot be determined analytically. This depends strongly on the periodic structure. To solve this problem is the main part of this thesis.

2.9. Rescaled Variables

By examining Maxwell's curl equations (2.2), we recognize that there is no fundamental length scale in these equations. We also apply this property and scale all lengths in the system to the length a which is finally set equal to the lattice constant d_1. Thus,

we introduce new dimensionless variables

$$\begin{aligned} \nu' &= \frac{\omega a}{2\pi c_0} = \frac{a}{\lambda}, & \omega' &= \frac{\omega a}{c_0}, \\ \lambda' &= \frac{\lambda}{a}, & k' &= ka, \\ x' &= \frac{x}{a}, & t' &= \frac{c_0}{a}t, \end{aligned} \tag{2.78}$$

which are denoted by a prime $'$. The dispersion relation of homogeneous space is in the rescaled system $\omega' = k'/n$. Additionally, we scale the electric and magnetic fields to

$$\mathbf{E}' = \sqrt{\epsilon_0}\mathbf{E}, \tag{2.79a}$$
$$\mathbf{H}' = \sqrt{\mu_0}\mathbf{H}. \tag{2.79b}$$

Thus, we can write the time-harmonic curl equations (2.65) as

$$\xi^{ijk}\partial_j E_k = \mathrm{i}\omega\mu^{ij}H_j, \tag{2.80a}$$
$$\xi^{ijk}\partial_j H_k = -\mathrm{i}\omega\epsilon^{ij}E_j, \tag{2.80b}$$

where we omitted already the primes. From here on, we use Maxwell's equations always with the scaled variables. This form of Maxwell's equations is useful for our simulations since we do not have to operate with the vacuum permittivity and permeability such as the vacuum speed of light. Additionally, in the case of nondispersive materials, the calculation does not depend on the wavelength but only on the ratio of the wavelength to the structure size.
To compare with real values, we simply have to multiply the rescaled results with the appropriate factors according to the scaling rules in eqs. (2.78) and (2.79).

3. Numerical Methods in Diffractive Optics

In this thesis, we are interested in the simulation of periodic nanostructures by the Fourier Modal Method (FMM).
Originally, the FMM was developed to investigate the incidence of a plane wave on a grating in order to obtain the transmitted and reflected plane waves in the several spatial harmonics, as already discussed in section 2.8.2. Since the crucial prerequisite is the periodicity of the system in the grating plane, the FMM can also be applied to the investigation of photonic crystals and metamaterials.
In this chapter, we start with a short overview on the development of the method. Then, we present the FMM for three-dimensional systems. We introduce the systems which can be investigated. In the FMM, the periodic region is divided into a stack of two-dimensional subsystems via the so-called staircase approximation. These subsystems can be solved independently as eigenvalue problems. The individual solutions are finally combined to form the complete system by a scattering matrix approach. Thus, we can calculate the reflectance and transmittance as well as the fields in the periodic structures. We also show how the FMM can be extended to investigate non-periodic structures. Besides, point sources may be introduced into the grating region and can serve as internal light sources instead of an external illumination by an incident plane wave. Finally, we shortly present the Chandezon method, which solves the grating problem by transforming it into curvilinear coordinates. This method is of relevance since similar techniques are used in chapter 5, where we formulate the FMM in curvilinear coordinates.

3.1. Historical Review

One of the first methods for the numerical investigation of gratings has been the differential method [16]. The method is mainly applied to calculate the interaction of light with gratings. More precisely, a plane wave is impinging on a grating as in section 2.8.2 and the aim is to obtain the electric and magnetic fields in- and outside the grating structure. Thus, only time-harmonic Maxwell's equations are considered – the method belongs to the class of frequency domain methods.
The grating system is divided into three regions: (i) The homogeneous superstrate above the grating, (ii) the structured grating region, and (iii) the homogeneous substrate region as shown in fig. 3.1(a). Due to the periodicity of the grating, the solutions in the homogeneous super- and substrate are given by the Rayleigh expansion (see eqs. (2.76) and (2.77)). The fields in the grating region can be expanded in Fourier se-

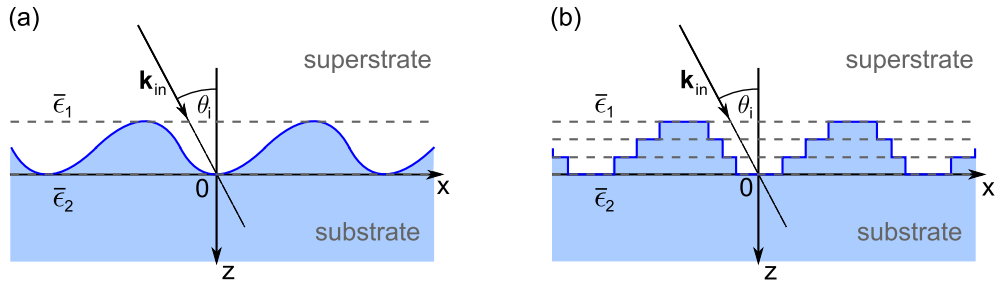

Figure 3.1.: (a) Grating with homogeneous superstrate half-space, structured grating region and the homogeneous substrate half-space. (b) Same grating as in (a) but built of three stacked lamellar gratings by means of the staircase approximation.

ries along the periodic directions according to the Bloch theorem (2.71). By inserting the expansion for the grating region in Maxwell's curl equations (2.80), we obtain a set of differential equations for the coefficients which determine the propagation of the light perpendicular to the grating plane. Together with the Rayleigh expansions in the super- and substrate, the differential equations form a boundary value problem. In the classical differential method this is solved via the so-called shooting method [16].
Since these problems are solved with computers, the infinite series of the expansions have to be truncated. This can cause convergence problems which already arise for purely two-dimensional metallic gratings in H-polarization. Additionally, the method becomes unstable for deep gratings [16]. By trying to find alternative approaches, new methods, such as the Rigorous Coupled Wave Analysis (RCWA)[34, 35], have been developed. Here, the grating profile is approximated by a stack of lamellar gratings by the staircasing technique as illustrated in fig. 3.1(b). In this case, each lamellar grating can be solved independently by an eigenvalue technique. Originally, the different gratings are connected at the interfaces using the continuity condition of the tangential electric and magnetic fields through the transfer matrix method. Unfortunately, again the convergence of metallic gratings for H-polarization was not satisfactory and for deep gratings numerical instabilities have been observed [36].
A first step towards stable and reliable results was made by introducing the scattering matrix algorithm. It replaces the transfer matrix method [37] and removes the inherent instabilities. The superiority of the scattering matrix is due to the careful treatment of the evanescent modes when matching the individual lamellar gratings.
At the same time the convergence for lamellar metallic gratings in the RCWA for H-polarization has been improved [38, 39]. The explanation was found in the convergence behavior of the truncated Fourier series for continuous and discontinuous functions and is named correct Fourier factorization [40]. Using this technique a new formulation of the RCWA for crossed gratings was established by Li that is called the FMM [18]. It is the fundamental method of this thesis.
Clearly, the correct Fourier factorization was also useful for the differential method and improved the convergence behavior [41]. The resulting algorithm is called the Fast Fourier Factorization method. Of course, the scattering matrix algorithm was also

included in the differential method to avoid the unstable behavior for deep gratings [16].
Another method which evolved from the differential method was the Chandezon method [17, 42]. Here, the grating problem is solved by transforming the grating surface into a planar surface. Then, in this curvilinear coordinates the system consists of two homogeneous regions, where the Rayleigh expansion can be applied. However, this method exhibits similarly bad convergence properties for grating profiles with sharp edges as the RCWA for H-polarization. Since the origin is the same this could be also improved by the correct Fourier factorization rules [43].
In the following, we present the Fourier Modal Method as developed by Li and also provide an introduction to the Chandezon method as an example of a numerical method formulated in curvilinear coordinates.

3.2. Fourier Modal Method

3.2.1. System

Before we start to explain the FMM, we specify the systems which are investigated. As in fig. 3.1, we orient the grating in the Cartesian system such that the $\bar{x}^3$-axis (which is the z-axis in the figure) is perpendicular to the grating plane. The substrate region below the grating consists of a material with permittivity ϵ_{out} and the region above the grating, the superstrate, has permittivity ϵ_{in}. The periodic directions in the x^1x^2-plane do not need to be orthogonal. Thus, we work in a nonrectangular coordinate system $Ox^1x^2x^3$ that is defined by the lattice vectors. The lattice vectors in real and reciprocal space are defined as in eqs. (2.67) and (2.68). They are connected to the Cartesian coordinates $Oxyz = O\bar{x}^1\bar{x}^2\bar{x}^3$ by the relation [18]

$$\bar{x}^1 = x^1 + x^2 \sin\zeta, \tag{3.1a}$$
$$\bar{x}^2 = x^2 \cos\zeta, \tag{3.1b}$$
$$\bar{x}^3 = x^3, \tag{3.1c}$$

where ζ is the angle between the $\bar{x}^2$- and x^2-axis. The x^1-axis is parallel to the $\bar{x}^1$-axis. The basis vectors can be derived as described in section 2.7.1. Thus, we obtain the contravariant metric tensor

$$g^{ij} = \begin{pmatrix} \sec^2\zeta & -\tan\zeta\sec\zeta & 0 \\ -\tan\zeta\sec\zeta & \sec^2\zeta & 0 \\ 0 & 0 & 1 \end{pmatrix}, \tag{3.2}$$

with the inverse determinant $g = \cos^2\zeta$. Hence, in the nonrectangular coordinates the permittivity is anisotropic (2.64a). Since we assume isotropic materials in the Cartesian system, all anisotropic components of the permittivity in the nonrectangular coordinates show the same spatial variation, but the strength is determined by a geometry-dependent factor. The permeability (2.64b) becomes anisotropic, too. However, each component is constant since in the original Cartesian system the permeability tensor is equal to the unit matrix. In the following, we prefer formulating Maxwell's equations

with the permeability terms though they contain only angle-dependent factors as the metric tensor g^{ij} in eq. (3.2).
Since the coordinate transformation is performed only in the grating plane, the anisotropy exhibits a principal axis along the x^3-axis. In comparison to completely anisotropic systems, this property simplifies the method later in section 3.2.3.
First, we present the incident field in the superstrate. Then, we explain how to treat the structured region in the FMM. Thereafter, we handle the homogeneous super- and substrate regions of the system which can be treated as special cases of the structured region.

3.2.2. Incident Plane Wave

The light impinges as a linearly polarized plane wave on the grating from the superstrate region. This is not a restriction since we can decompose arbitrarily-shaped waves into plane waves (2.28) and solve each component independently. In the nonrectangular coordinates we obtain for the covariant field components of the plane wave E_σ and H_σ with $\sigma = 1, 2, 3$

$$E_\sigma(x^1, x^2, x^3) = E_{0,\sigma} \mathrm{e}^{\mathrm{i}(\alpha_0 x^1 + \beta_0 x^2 + \gamma_0^{\mathrm{in}} x^3)}, \tag{3.3a}$$
$$H_\sigma(x^1, x^2, x^3) = H_{0,\sigma} \mathrm{e}^{\mathrm{i}(\alpha_0 x^1 + \beta_0 x^2 + \gamma_0^{\mathrm{in}} x^3)}. \tag{3.3b}$$

The components of the incident wave vector are

$$\alpha_0 = k^{\mathrm{in}} \sin\theta \cos\phi, \tag{3.4a}$$
$$\beta_0 = k^{\mathrm{in}} \sin\theta \sin(\phi + \zeta), \tag{3.4b}$$
$$\gamma_0^{\mathrm{in}} = k^{\mathrm{in}} \cos\theta, \tag{3.4c}$$

which is denoted in fig. 3.1 by $\mathbf{k}_{\mathrm{in}} = (\alpha_0, \beta_0, \gamma_0^{\mathrm{in}})$ with $k^{\mathrm{in}} = \sqrt{\epsilon_{\mathrm{in}}} k_0$. k_0 is the wave vector in vacuum. The direction of incidence is determined by the azimuth angle θ and the polar angle ϕ. The polarization of the incident plane wave can be arbitrary. However, we always calculate two orthogonal polarizations. Thus, by superposition, arbitrarily polarized incident plane waves can be generated. On the one hand, we choose a s-polarized plane wave as introduced in section 2.6. The components of the electric and magnetic field are [44]

$$\begin{aligned} E_{0,1} &= E_0 \sin\phi, & H_{0,1} &= E_0 \sqrt{\epsilon_{\mathrm{in}}} \cos\theta \cos\phi, \\ E_{0,2} &= -E_0 \cos(\phi + \zeta), & H_{0,2} &= E_0 \sqrt{\epsilon_{\mathrm{in}}} \cos\theta \sin(\phi + \zeta), \\ E_{0,3} &= 0, & H_{0,3} &= -E_0 \sqrt{\epsilon_{\mathrm{in}}} \sin\theta. \end{aligned}$$

On the other hand, we calculate a p-polarized incident plane wave with

$$\begin{aligned} E_{0,1} &= E_0 \cos\theta \cos\phi, & H_{0,1} &= -E_0 \sqrt{\epsilon_{\mathrm{in}}} \sin\phi, \\ E_{0,2} &= E_0 \cos\theta \sin(\phi + \zeta), & H_{0,2} &= E_0 \sqrt{\epsilon_{\mathrm{in}}} \cos(\phi + \zeta), \\ E_{0,3} &= -E_0 \sin\theta, & H_{0,3} &= 0. \end{aligned}$$

3.2.3. Structured Region

In the FMM, the structured region is divided into several subsystems by the staircase approximation. This means the subsystems are slices perpendicular to the x^3-axis [35]. The individual slices are homogeneous in x^3-direction and they are periodic in the slicing plane. As illustrated in fig. 3.2, arbitrarily shaped systems can be approximated by stacks of such slices. Due to the homogeneity in one direction, the dimensionality of the problem is reduced and we only have to solve two-dimensional subsystems which can be treated independently of each other. This is a significant advantage of the method since slices which appear several times in the structure have to be calculated only once. Additionally, systems which can be divided into thick slices can be treated particularly efficiently because only the number of slices is relevant.

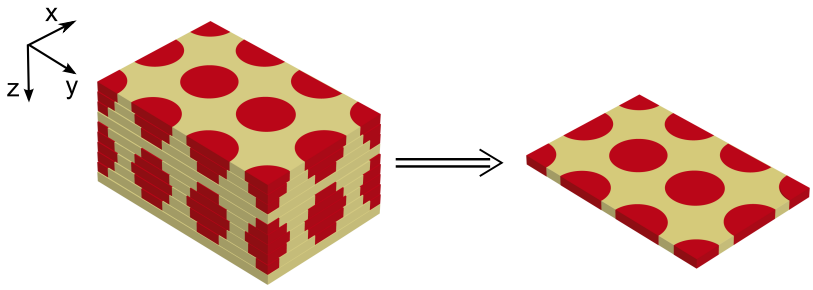

Figure 3.2.: Sliced crystal with single slice to the right.

As next step, we have to solve Maxwell's equations in the individual slices. In the two-dimensional plane, the fields in the slices have to fulfill the Bloch theorem (2.71). The lattice periodic function of the Bloch wave is Fourier transformed. Therefore, the fields are expanded in Fourier-Floquet series. This expansion can be regarded as an extension of the Rayleigh expansion (see section 2.8.2) and we obtain

$$F_\sigma(x^1, x^2, x^3) = \sum_m f_{\sigma m}(x^3) \mathrm{e}^{\mathrm{i}\alpha_{m_1} x^1 + \mathrm{i}\beta_{m_2} x^2}. \tag{3.5}$$

F_σ stands for any one of the six components of the electric and magnetic field. The components $f_{\sigma m}$ are the x^3-dependent Fourier coefficients which have to be determined via Maxwell's equations. The wave vector components α_{m_1} and β_{m_2} are defined as in eq. (2.74). The summation runs over the points in the two-dimensional reciprocal space which are denoted by the pairs $m = \{m_1, m_2\}$. This sum has to be truncated since we can only handle a finite number of coefficients. The reciprocal space can be truncated to parallelogram or circular shape as illustrated in fig. 3.3. The number of points in the truncated space is denoted by N. In this thesis, we usually apply the truncation on a circular area.
We also have to transform the permittivity and permeability in each slice into Fourier space. Because of the truncation of the reciprocal space we do not simply want to use the Fourier expansion of the permittivity as denoted in eq. (2.70). In order to obtain fast convergence, the expansion has to be performed by carefully considering Li's Fourier Factorization rules [40], which are presented in appendix A.1. With these

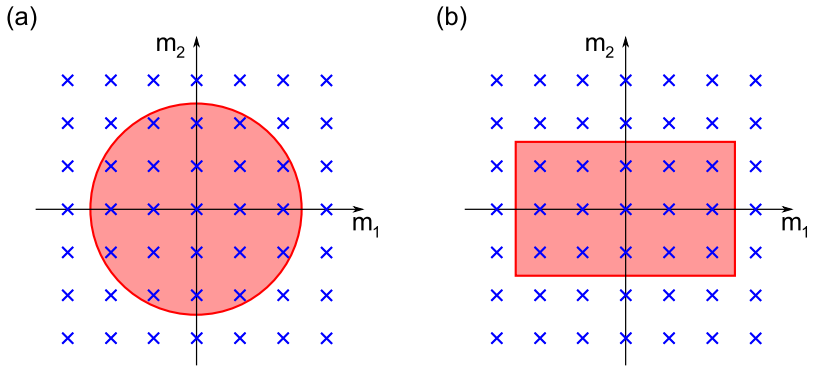

Figure 3.3.: Reciprocal space of the transformed system with truncation on a (a) circular and (b) parallelogram-shaped area.

rules the permittivity has to be Fourier transformed by considering the constitutive relation

$$D^i = \epsilon^{ij} E_j.$$

The exact calculation in the nonrectangular coordinate system is given in appendix A.2. In Fourier space we obtain for the constitutive relation

$$\mathbf{d}^i = [\![\epsilon^{ij}]\!]\, \mathbf{e}_j$$

with the Toeplitz matrix of the permittivity as defined in eq. (A.14), the Fourier vectors for the electric field $\mathbf{e}$ and the dielectric displacement field $\mathbf{d}$. The Fourier vectors contain the Fourier coefficients of the Fourier-Floquet expansions in eq. (3.5).
After inserting the field expansion and the Toeplitz matrices, Maxwell's curl equations (2.80) read

$$\begin{aligned}
\hat{\beta}\mathbf{e}_3 + \mathrm{i}\partial_3 \mathbf{e}_2 &= \omega \left([\![\mu^{11}]\!]\, \mathbf{h}_1 + [\![\mu^{12}]\!]\, \mathbf{h}_2 \right), && \text{(3.6a)}\\
-\mathrm{i}\partial_3 \mathbf{e}_1 - \hat{\alpha}\mathbf{e}_3 &= \omega \left([\![\mu^{21}]\!]\, \mathbf{h}_1 + [\![\mu^{22}]\!]\, \mathbf{h}_2 \right), && \text{(3.6b)}\\
\hat{\alpha}\mathbf{e}_2 - \hat{\beta}\mathbf{e}_1 &= \omega\, [\![\mu^{33}]\!]\, \mathbf{h}_3, && \text{(3.6c)}
\end{aligned}$$

and

$$\begin{aligned}
\hat{\beta}\mathbf{h}_3 + \mathrm{i}\partial_3 \mathbf{h}_2 &= -\omega \left([\![\epsilon^{11}]\!]\, \mathbf{e}_1 + [\![\epsilon^{12}]\!]\, \mathbf{e}_2 \right), && \text{(3.7a)}\\
-\mathrm{i}\partial_3 \mathbf{h}_1 - \hat{\alpha}\mathbf{h}_3 &= -\omega \left([\![\epsilon^{21}]\!]\, \mathbf{e}_1 + [\![\epsilon^{22}]\!]\, \mathbf{e}_2 \right), && \text{(3.7b)}\\
\hat{\alpha}\mathbf{h}_2 - \hat{\beta}\mathbf{h}_1 &= -\omega\, [\![\epsilon^{33}]\!]\, \mathbf{e}_3. && \text{(3.7c)}
\end{aligned}$$

$\hat{\alpha}$ and $\hat{\beta}$ are diagonal matrices with the entries $\alpha_{mn} = \alpha_{m_1}\delta_{mn}$ and $\beta_{mn} = \beta_{m_2}\delta_{mn}$. We eliminate $\mathbf{e}_3$ and $\mathbf{h}_3$ via eqs. (3.7c) and (3.6c), respectively. Then, we cast eq. (3.6) in the form

$$\partial_3 \mathbf{e}_\parallel = \mathrm{i} F \mathbf{h}_\parallel \tag{3.8}$$

with the matrix

$$F = \begin{pmatrix} \omega\, [\![\mu^{11}]\!] - \frac{1}{\omega}\hat{\beta}\, [\![\epsilon^{33}]\!]^{-1}\, \hat{\beta} & \omega\, [\![\mu^{12}]\!] + \frac{1}{\omega}\hat{\beta}\, [\![\epsilon^{33}]\!]^{-1}\, \hat{\alpha} \\ \omega\, [\![\mu^{21}]\!] + \frac{1}{\omega}\hat{\alpha}\, [\![\epsilon^{33}]\!]^{-1}\, \hat{\beta} & \omega\, [\![\mu^{22}]\!] - \frac{1}{\omega}\hat{\alpha}\, [\![\epsilon^{33}]\!]^{-1}\, \hat{\alpha} \end{pmatrix}. \tag{3.9}$$

The Fourier coefficients of the fields parallel to the slices are denoted by the vectors

$$\mathbf{e}_\parallel = \begin{pmatrix} -\mathbf{e}_2 \\ \mathbf{e}_1 \end{pmatrix} \quad \text{and} \quad \mathbf{h}_\parallel = \begin{pmatrix} \mathbf{h}_1 \\ \mathbf{h}_2 \end{pmatrix}. \tag{3.10}$$

In the same manner we reformulate eq. (3.7) as

$$\partial_3 \mathbf{h}_\parallel = \mathrm{i} G \mathbf{e}_\parallel, \tag{3.11}$$

with the matrix

$$G = \begin{pmatrix} \omega \left[\!\left[\epsilon^{22}\right]\!\right] - \frac{1}{\omega}\hat{\alpha} \left[\!\left[\mu^{33}\right]\!\right]^{-1} \hat{\alpha} & -\omega \left[\!\left[\epsilon^{21}\right]\!\right] - \frac{1}{\omega}\hat{\alpha} \left[\!\left[\mu^{33}\right]\!\right]^{-1} \hat{\beta} \\ -\omega \left[\!\left[\epsilon^{12}\right]\!\right] - \frac{1}{\omega}\hat{\beta} \left[\!\left[\mu^{33}\right]\!\right]^{-1} \hat{\alpha} & \omega \left[\!\left[\epsilon^{11}\right]\!\right] - \frac{1}{\omega}\hat{\beta} \left[\!\left[\mu^{33}\right]\!\right]^{-1} \hat{\beta} \end{pmatrix}. \tag{3.12}$$

By merging the two eqs. (3.8) and (3.11), we obtain a second order differential equation for the Fourier coefficients of the parallel electric field components

$$-\partial_3^2 \mathbf{e}_\parallel = FG\mathbf{e}_\parallel. \tag{3.13}$$

It is this equation which we have to solve in each slice.
Since the slices are homogeneous in x^3-direction we can apply a simple plane-wave ansatz for the x^3-dependence of the electric field as

$$\mathbf{e}_\parallel(x^3) = \mathbf{\Phi} \mathrm{e}^{\mathrm{i}qx^3}. \tag{3.14}$$

The propagation constant along the x^3-direction is q and the corresponding field vector is denoted by $\mathbf{\Phi}$. With the help of this ansatz we obtain the eigenvalue problem

$$q^2 \mathbf{\Phi} = FG\mathbf{\Phi}, \tag{3.15}$$

which yields $2N$ eigenvectors and eigenvalues. The eigenvectors represent the eigenmodes in the two-dimensional periodic subsystem. These solutions are two-dimensional Bloch waves. The corresponding eigenvalue q^2 is the squared propagation constant in x^3-direction. For each eigenmode we obtain two propagation constants by taking the square root of the eigenvalue. The two propagation constants describe the eigenmode propagating on the one hand downwards and on the other hand upwards in the slice. We define the propagation constant q such that $\mathrm{Im}(q) \geq 0$, which is the downward propagating case in direction of the positive x^3-axis.
Then, the electric field in the slice is expanded into the eigenstates $\mathbf{\Phi}$

$$\mathbf{e}_\parallel = \sum_{n=1}^{2N} \mathbf{\Phi}_n \left(\mathrm{e}^{\mathrm{i}q_n x^3} a_n + \mathrm{e}^{\mathrm{i}q_n (d - x^3)} b_n \right), \tag{3.16}$$

with the coefficients a_n (b_n) for the downward (upward) propagating modes. We set the phase of the downward propagating mode to zero at the lower end of the slice and the phase of the upward propagating mode at the upper end according to ref. [44]. The slice has thickness d as illustrated in fig. 3.4.

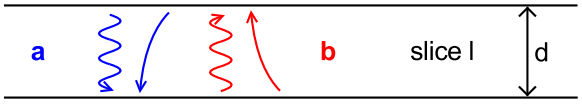

Figure 3.4.: Amplitudes of downward (**a**) and upward (**b**) propagating modes in a single slice l with thickness d.

The magnetic field is determined by eq. (3.11) as

$$\mathbf{h}_{\parallel} = G \sum_{n=1}^{2N} \mathbf{\Phi}_n q_n^{-1} \left(\mathrm{e}^{\mathrm{i}q_n x^3} a_n - \mathrm{e}^{\mathrm{i}q_n (d-x^3)} b_n \right). \tag{3.17}$$

In matrix form the expansions of the electric and magnetic fields are

$$\begin{pmatrix} \mathbf{e}_{\parallel} \\ \mathbf{h}_{\parallel} \end{pmatrix} = \begin{pmatrix} W_1 & W_1 \\ W_2 & -W_2 \end{pmatrix} \begin{pmatrix} \hat{f}(x^3)\mathbf{a} \\ \hat{f}(d-x^3)\mathbf{b} \end{pmatrix}, \tag{3.18}$$

with the two matrices

$$W_1 = \Phi, \tag{3.19a}$$
$$W_2 = G\Phi\hat{q}^{-1}, \tag{3.19b}$$

and the phase matrices $\hat{f}(x^3)$. The phase matrices are diagonal matrices with entries $f_n(x^3) = \mathrm{e}^{\mathrm{i}q_n x^3}$. These entries mimic the propagation of the mode through the slice. Φ denotes the matrix with all eigenvectors $\mathbf{\Phi}_n$. By this representation we can easily couple the solutions of adjacent slices at their mutual interface.

3.2.4. Homogeneous Regions

In the homogeneous super- and substrate region we can represent the electric and magnetic fields by the Rayleigh expansion due to the periodicity of the grating as already discussed in section 2.8.2 by eqs. (2.76) and (2.77).
In the superstrate region we obtain for the covariant components of the electric field

$$E_{\sigma}^{\mathrm{sup}}(x^1, x^2, x^3) = E_{0,\sigma} \mathrm{e}^{\mathrm{i}\alpha_0 x^1 + \mathrm{i}\beta_0 x^2 + \mathrm{i}\gamma_0 x^3} + \sum_m E_{\sigma,m}^{\mathrm{refl}} \mathrm{e}^{\mathrm{i}\alpha_{m_1} x^1 + \mathrm{i}\beta_{m_2} x^2 - \mathrm{i}\gamma_m^{\mathrm{in}} x^3} \tag{3.20}$$

with the incident plane wave and the reflected spatial harmonics. In the substrate we only have the transmitted light in its different diffraction orders

$$E_{\sigma}^{\mathrm{sub}}(x^1, x^2, x^3) = \sum_m E_{\sigma,m}^{\mathrm{trans}} \mathrm{e}^{\mathrm{i}\alpha_{m_1} x^1 + \mathrm{i}\beta_{m_2} x^2 + \mathrm{i}\gamma_m^{\mathrm{out}} x^3}. \tag{3.21}$$

The reflected and transmitted field amplitudes are denoted by $E_{\sigma,m}^{\mathrm{refl}}$ and $E_{\sigma,m}^{\mathrm{trans}}$, respectively. The summation runs over the same reciprocal space as in the case of the structured slices in eq. (3.5). The wave vector components α_{m_1} and β_{m_2} are defined as

in eq. (2.74) and the third component γ_m is given by eq. (2.75). In the nonrectangular coordinate system with the metric (3.2) we obtain in both homogeneous regions

$$\gamma_m^{\text{in/out}} = \sqrt{\epsilon^{\text{in/out}} k_0^2 - \sec^2\zeta \left(\alpha_{m_1}^2 + \beta_{m_2}^2 - 2\alpha_{m_1}\beta_{m_2}\sin\zeta\right)}. \tag{3.22}$$

The permittivity is always real in the super- and substrate of the systems, since we consider only non-absorbing materials in these regions. Thus, the wave vector components are either purely real or purely imaginary. They describe either propagating waves or evanescent waves.
With the resulting reflected and transmitted fields we determine the reflectance and transmittance into the different diffraction orders as in section 2.8.2. We either directly calculate the Poynting vector for each diffraction order by the electric fields via eq. (2.34) or we determine the transmittance and reflectance with the amplitudes of each propagating plane wave by eq. (2.48). The resulting values are identical.
We also obtain the Rayleigh solutions of the homogeneous super- and substrate region by solving the eigenvalue problem (3.15) numerically with the corresponding Toeplitz matrices. However, we solve the eigenvalue problem analytically in order to treat the possible degeneracy of the eigenvalues correctly. Then, the eigenvector matrix Φ is a unit matrix $\mathbb{1}$ and the eigenvalues are given by $q^2 = \left(\gamma_m^{\text{in/out}}\right)^2$. The degenerate eigenvectors are treated such that the field vectors represent the Rayleigh expansion as in eqs. (3.20) and (3.21). Thus, the solutions of the eigenvalue problems in the super- and substrate region are expressed in the same form as the solutions in the structured layers. This simplifies the formalism later. The electric field expansion in these regions can then be written down as in eq. (3.16). With the help of the G-matrix (3.12), we can directly determine the corresponding magnetic fields by eq. (3.17). In the calculation, the thickness d of the super- and substrate region can be chosen arbitrarily since the two regions should not contain absorbing materials. Therefore, the propagation length does not play a role. Finally, we can write the solution in the form of eq. (3.18) and we can treat all slices identical when we connect the solutions in the different slices in the following.

3.2.5. Scattering Matrix

Until now we know the eigensolutions in the individual slices. As illustrated in fig. 3.5 we have $L+2$ slices: L slices in the structured region plus one slice each for the super- and substrate regions. Now, we have to rebuild the complete system by stacking these $L+2$ slices on top of each other (see fig. 3.5). Adjacent slices can be connected at the interfaces by the tangential field components which have to be continuous.
Thus, if we consider the interface between slice l and slice $l+1$, we have to equate the fields in slice l on the bottom at $x^3 = d_l$ with fields in slice $l+1$ on top at $x^3 = 0$

$$\begin{pmatrix} \mathbf{e}_\parallel^{(l)} \\ \mathbf{h}_\parallel^{(l)} \end{pmatrix} (x^3 = d_l) = \begin{pmatrix} \mathbf{e}_\parallel^{(l+1)} \\ \mathbf{h}_\parallel^{(l+1)} \end{pmatrix} (x^3 = 0). \tag{3.23}$$

Now, we can determine an interface matrix to connect the amplitudes in the adjacent

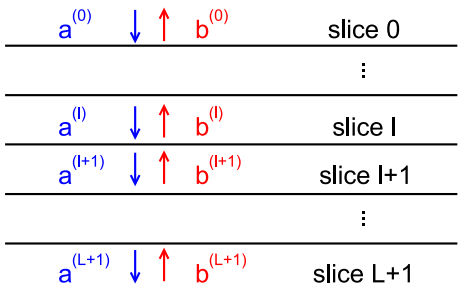

Figure 3.5.: Connection of neighboring slices at the interfaces by the tangential fields components in order to couple the amplitudes in the first and last slice.

slices by a transfer matrix

$$\begin{pmatrix} \hat{f}^{(l)}(d_l)\mathbf{a}^{(l)} \\ \mathbf{b}^{(l)} \end{pmatrix} = I(l, l+1) \begin{pmatrix} \mathbf{a}^{(l+1)} \\ \hat{f}^{(l+1)}(d_{l+1})\mathbf{b}^{(l+1)} \end{pmatrix}. \tag{3.24}$$

This matrix is illustrated in fig. 3.6. The interface matrix $I(l, l+1)$ can be easily expressed by the W_1 and W_2 matrices [45, 46]

$$I(l, l+1) = \frac{1}{2} \begin{pmatrix} Q_1(l, l+1) + Q_2(l, l+1) & Q_1(l, l+1) - Q_2(l, l+1) \\ Q_1(l, l+1) - Q_2(l, l+1) & Q_1(l, l+1) + Q_2(l, l+1) \end{pmatrix}, \tag{3.25}$$

where $Q_i(l, l+1) = \left(W_i^{(l)}\right)^{-1} W_i^{(l+1)}$.
In other words, the interface matrix propagates the field from one slice to the adjacent slice by relating the amplitudes in slice l to the amplitudes in slice $l+1$. Following this line of thought, we can construct a matrix which connects the amplitudes in the superstrate slice with the amplitudes in the substrate slice by simple matrix multiplications. This corresponds to the transfer matrix algorithm. Unfortunately, it turns out that this algorithm is numerically unstable [37, 47] since it allows the fields to grow exponentially. This can be a problem when the slices become too thick. Therefore, we use the scattering matrix algorithm which relates the incoming amplitudes to the outgoing amplitudes on the interface and we can rewrite eq. (3.24) in the form of a scattering matrix

$$\begin{pmatrix} \mathbf{a}^{(l+1)} \\ \mathbf{b}^{(l)} \end{pmatrix} = S(l, l+1) \begin{pmatrix} \mathbf{a}^{(l)} \\ \mathbf{b}^{(l+1)} \end{pmatrix}. \tag{3.26}$$

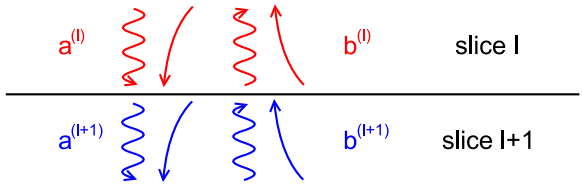

Figure 3.6.: Matching of evanescent and propagating modes at a layer interface via the transfer matrix. The modes in slice l are marked in blue and the ones in slice $l+1$ are red.

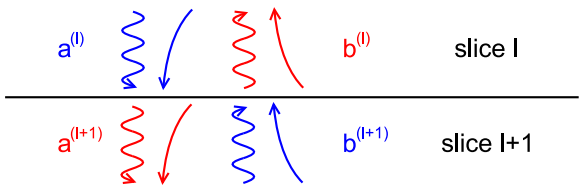

Figure 3.7.: Matching of evanescent and propagating modes at a layer interface via the scattering matrix. The incoming waves to the interface are marked in blue and the outgoing waves are red.

This approach is numerically stable since it guarantees that the evanescent field components are only incorporated as decaying waves and not the inverse way where they would experience an exponential growth. This behavior is illustrated in fig. 3.7 in contrast to fig. 3.6: The incoming evanescent waves (blue) always decay in direction of the interface and the outgoing evanescent waves (red) always decay away from the interface. The scattering matrix deals with the amplitudes by connecting the evanescent waves to the solutions in the neighboring slice at their decaying tails.
In order to build the scattering matrix for the complete system, we successively add new slices to the scattering matrix. Thus, we start in slice $l = 0$ with the scattering matrix $S(0,0) = \mathbb{1}$ and add slice $l = 1$ with the help of the interface matrix $I(0,1)$ and obtain the scattering matrix $S(0,1)$. Then, we add all slices step by step until we reach the last slice, the substrate. In general, we can describe the recursive scattering matrix algorithm by appending the slice $l+1$ to the already existing scattering matrix $S(0,l)$. The latter connects the amplitudes in slice 0 with slice l according to

$$\begin{pmatrix} \mathbf{a}^{(l)} \\ \mathbf{b}^{(0)} \end{pmatrix} = S(0,l) \begin{pmatrix} \mathbf{a}^{(0)} \\ \mathbf{b}^{(l)} \end{pmatrix} = \begin{pmatrix} S(0,l)_{11} & S(0,l)_{12} \\ S(0,l)_{21} & S(0,l)_{22} \end{pmatrix} \begin{pmatrix} \mathbf{a}^{(0)} \\ \mathbf{b}^{(l)} \end{pmatrix}. \tag{3.27}$$

The new scattering matrix $S(0,l+1)$ is constructed by the following instruction [37, 44]

$$\begin{aligned}
S(0,l+1)_{11} &= (I_{11} - \hat{f}(d_l) S(0,l)_{12} I_{21})^{-1} \hat{f}(d_l) S(0,l)_{11}, && \text{(3.28a)} \\
S(0,l+1)_{12} &= (I_{11} - \hat{f}(d_l) S(0,l)_{12} I_{21})^{-1} \ldots \\
&\quad \left[\hat{f}(d_l) S(0,l)_{12} I_{22} \hat{f}(d_{l+1}) - I_{12} \hat{f}(d_{l+1}) \right], && \text{(3.28b)} \\
S(0,l+1)_{21} &= S(0,l)_{21} + S(0,l)_{22} I_{21} S(0,l+1)_{11}, && \text{(3.28c)} \\
S(0,l+1)_{22} &= S(0,l)_{22} \left[I_{21} S(0,l+1)_{12} + I_{22} \hat{f}(d_{l+1}) \right]. && \text{(3.28d)}
\end{aligned}$$

Finally, after having appended all slices, we obtain for the scattering matrix of the complete system the equation

$$\begin{pmatrix} \mathbf{a}^{(L+1)} \\ \mathbf{b}^{(0)} \end{pmatrix} = S(0,L+1) \begin{pmatrix} \mathbf{a}^{(0)} \\ \mathbf{b}^{(L+1)} \end{pmatrix}. \tag{3.29}$$

The matrix $S(0,L+1)$ relates the amplitudes in the superstrate ($l = 0$) and the substrate ($l = L+1$) as shown in fig. 3.8.

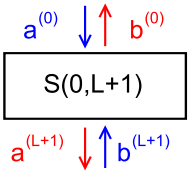

Figure 3.8.: Complete scattering matrix $S(0, L+1)$ of the system which relates the incoming amplitudes $\mathbf{a}^{(0)}$, $\mathbf{b}^{(L+1)}$ with the outgoing amplitudes $\mathbf{a}^{(L+1)}$, $\mathbf{b}^{(0)}$.

We assume an incident plane wave from the superstrate side of the system with the amplitude $\mathbf{a}^{(0)}$. The incidence from the substrate is set to zero $\mathbf{b}^{(L+1)} = 0$. Thus, we can determine the reflected $\mathbf{b}^{(0)}$ and transmitted amplitudes $\mathbf{a}^{(L+1)}$ by the scattering matrix

$$\mathbf{a}^{(L+1)} = S(0, L+1)_{11}\mathbf{a}^{(0)}, \tag{3.30}$$
$$\mathbf{b}^{(0)} = S(0, L+1)_{21}\mathbf{a}^{(0)}. \tag{3.31}$$

If we are interested in the transmittance and reflectance, we can simplify the computation since we need only half of the scattering matrix. Therefore, we reverse the system, meaning that the light impinges from slice $l = L+1$ with the amplitude $\mathbf{b}^{(L+1)}$. Then, we only need to calculate the matrices $S(0, L+1)_{12}$ and $S(0, L+1)_{22}$. As can be easily seen in eqs. (3.28), these two matrices can be calculated without knowledge of the other two matrices. This can be realized by building the scattering matrix with the substrate slice first [37].
A benefit of the scattering matrix approach is that we can decompose the system into blocks. For each of them we may construct the corresponding scattering matrix and then compose the system's full scattering matrix from these building blocks. This is especially useful if the system consists of repeating blocks which then do not have to be calculated twice. Thus, we define the multiplication of two scattering matrices as $S(0, N+1) = S(0, l) * S(l, N+1)$ which is calculated by [37]

$$S(0,N+1)_{11} = S(l,N+1)_{11}(\mathbb{1} - S(0,l)_{12}S(l,N+1)_{21})^{-1}S(0,l)_{11}, \tag{3.32a}$$
$$S(0,N+1)_{12} = S(l,N+1)_{12} + \ldots \tag{3.32b}$$
$$S(l,N+1)_{11}(\mathbb{1} - S(0,l)_{12}S(l,N+1)_{21})^{-1}S(0,l)_{12}S(l,N+1)_{22},$$
$$S(0,N+1)_{21} = S(0,l)_{21} + \ldots \tag{3.32c}$$
$$S(0,l)_{22}S(l,N+1)_{21}(\mathbb{1} - S(0,l)_{12}S(l,N+1)_{21})^{-1}S(0,l)_{11},$$
$$S(0,N+1)_{22} = S(0,l)_{22}\left[\mathbb{1} + S(l,N+1)_{21}\ldots\right.$$
$$\left.(\mathbb{1} - S(0,l)_{12}S(l,N+1)_{21})^{-1}S(0,l)_{12}\right]S(l,N+1)_{22}. \tag{3.32d}$$

Another possibility to define a scattering matrix is to directly connect the Fourier coefficients of the tangential fields rather than the amplitudes of the eigenmodes. Hence, for each slice we can establish a scattering matrix $S_{\mathrm{F}}^{(l)}$ which is independent of the adjacent slices

$$\begin{pmatrix} \mathbf{e}_{\parallel}^{(l)}(x^3 = d^{(l)}) \\ \mathbf{h}_{\parallel}^{(l)}(x^3 = 0) \end{pmatrix} = S_{\mathrm{F}}^{(l)} \begin{pmatrix} \mathbf{e}_{\parallel}^{(l)}(x^3 = 0) \\ \mathbf{h}_{\parallel}^{(l)}(x^3 = d^{(l)}) \end{pmatrix}. \tag{3.33}$$

The scattering matrices of the slices can be connected to the scattering matrix of the complete system by simply multiplying the scattering matrices according to eq. (3.32). The advantage of this formulation is that the scattering matrix directly gives the electric and magnetic fields. However, the forward and backward propagating amplitudes of the different diffraction orders in reflectance and transmittance need to be determined from the fields and cannot be calculated directly. Thus, if one is mainly interested in calculating the fields in the structures, this formulation is preferable. However, in this thesis, we stick to the scattering matrix for the amplitudes as defined in eq. (3.29).

3.2.6. Calculating the Field Distribution

The FMM does not only provide the transmittance and reflectance coefficients (see preceding section) but also the field distribution in the structure. In this section we will show how to determine the fields inside each individual slice.
The plane in which we calculate the fields is located in a certain slice l. Thus, we determine the amplitudes of the forward and backward propagating modes $a_n^{(l)}$ and $b_n^{(l)}$, respectively. Therefore, we need two scattering matrices: (i) $S(0,l)$ relating the superstrate slice with slice l and (ii) $S(l,N+1)$ relating slice l with the substrate slice. With these two matrices we obtain the desired amplitudes

$$\begin{aligned}
\mathbf{a}^{(l)} &= \left(\mathbb{1} - S(0,l)_{12}S(l,N+1)_{21}\right)^{-1}\ldots \\
&\quad \left(S(0,l)_{11}\mathbf{a}^{(0)} + S(0,l)_{12}S(l,N+1)_{22}\mathbf{b}^{(N+1)}\right), \qquad (3.34a)\\
\mathbf{b}^{(l)} &= \left(\mathbb{1} - S(l,N+1)_{21}S(0,l)_{12}\right)^{-1}\ldots \\
&\quad \left(S(l,N+1)_{21}S(0,l)_{11}\mathbf{a}^{(0)} + S(l,N+1)_{22}\mathbf{b}^{(N+1)}\right), \qquad (3.34b)
\end{aligned}$$

as functions of the incident fields from the super- and substrate half-space. Then, the Fourier coefficients of the electric and magnetic field components in the plane are obtained with eq. (3.18). The calculated field in the slice at the designated x^3-position follows from the phase factors for the particular modes in the expansion. The out-of-plane field component is given by

$$\begin{aligned}
\mathbf{e}_3 &= -\frac{1}{\omega}\left[\!\left[\epsilon^{33}\right]\!\right]^{-1}\left(\hat{\alpha}\mathbf{h}_2 - \hat{\beta}\mathbf{h}_1\right), \qquad (3.35a)\\
\mathbf{h}_3 &= \frac{1}{\omega}\left[\!\left[\mu^{33}\right]\!\right]^{-1}\left(\hat{\alpha}\mathbf{e}_2 - \hat{\beta}\mathbf{e}_1\right). \qquad (3.35b)
\end{aligned}$$

In order to facilitate plotting of the field, we transform it back to the Cartesian coordinate system

$$\begin{aligned}
\mathbf{f}_x &= \mathbf{f}_1, \qquad (3.36a)\\
\mathbf{f}_y &= -\tan\zeta\mathbf{f}_1 + \sec\zeta\mathbf{f}_2, \qquad (3.36b)\\
\mathbf{f}_z &= \mathbf{f}_3, \qquad (3.36c)
\end{aligned}$$

where $\mathbf{f}$ stands for both the electric and the magnetic fields.
Along these lines we can determine the fields at any point in space. We only have to transform the Fourier representation of the field components back into real space by eq. (3.5) which provides the field in the xy-plane of the system.

3.2.7. Extensions to the Fourier Modal Method

The FMM has proven to be a powerful tool for calculating transmittance, reflectance and near field distributions of periodic structures which are illuminated by plane waves. However, it is interesting to investigate the optical properties of non-periodic systems, too. Such non-periodic systems include, for instance, optical resonators [48], individual metallic nano-particles [49], photonic crystal fibers [50] and photonic crystal waveguides [51]. Furthermore, in photonic systems the emission characteristics of quantum dots can be altered drastically [6, 52]. Thus, in this section, we address two different extensions to the FMM which have been established recently.
First, we explain how the restriction to periodic structures can be removed allowing for simulations of non-periodic structures. The other extension makes it possible to include dipole sources. Hence, the system cannot only be excited from outside by a plane wave but also directly from within the structure, mimicking, e.g., quantum dots in a photonic system. These two extensions increase the application range of the FMM. Consequently, our method develops toward a generally applicable simulation tool in electrodynamics.

Perfectly Matched Layers

In order to simulate non-periodic systems, we have to model open boundaries instead of periodic ones. A simple way to truncate the infinite periodic system volume to a finite simulation volume is to wrap the system with an absorbing layer. This technique can be easily incorporated into the FMM by adding absorbing layers at the boundaries of the unit cells [53]. Consequently, the light which is scattered by the structure in the unit cell and travels towards the neighboring unit cells is absorbed by this layer and the fields at the unit cell boundary shall decrease nearly to zero. Hence, the interaction between the periodically arranged structures is suppressed and the single unit cells can be regarded as isolated systems. The new pseudo-periodic system is shown in fig. 3.9 (a).

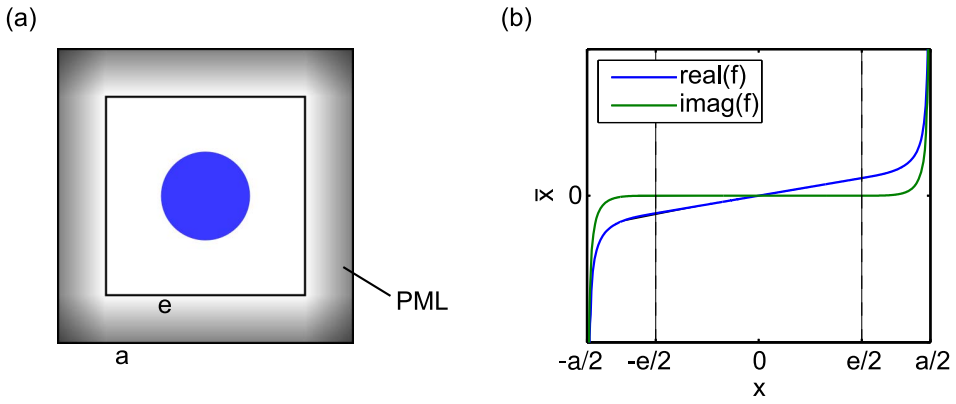

Figure 3.9.: (a) Isolated unit cells with absorbing layers. The region of interest has length e. Including the absorbing layers the size of the unit cell increases to a. (b) Complex coordinate transformation with $\gamma = 0.5 + 0.5\mathrm{i}$.

The material layer around the system shall not only be absorptive but also reflectionless for arbitrary angles of incidence, polarizations and frequencies of the impinging waves. Such a layer is called perfectly matched layer (PML). PMLs were originally introduced for the finite-difference time-domain (FDTD) method [12, 54, 55]. One possible realization is the introduction of an absorbing material with anisotropic permittivity and permeability [56, 57].
An equivalent formulation of the PMLs can be obtained by a coordinate transformation [58, 59]. As we have shown in section 2.7.2, any coordinate transformation can be described by anisotropic material equations (2.64) in the transformed space. By the coordinate transformation we can map the infinite space around the structure to a finite region. In order to include absorption, we analytically continue the equations on the complex plane in the infinite space. Thus, oscillating waves are altered to evanescent waves without reflection.
The proposed complex coordinate transformation for the FMM reads [58]

$$\bar{x}^i(x^i) = \begin{cases} x^i & ,|x^i| < e/2 \\ \frac{x^i}{|x^i|}\left(\frac{e}{2} + \frac{q}{\pi(1-\gamma)}\left\{\tan\left(\pi\frac{|x^i|-e/2}{q}\right)\ldots\right.\right. & \\ \left.\left. -\frac{\gamma}{\sqrt{1-\gamma}}\arctan\left[\sqrt{1-\gamma}\tan\left(\pi\frac{|x^i|-e/2}{q}\right)\right]\right\}\right) & ,e/2 < |x^i| < a/2, \end{cases}$$

for $i = 1, 2$. The transformation is plotted in fig. 3.9 (b). By this transformation, we obtain a unit cell for the FMM with lattice constant a. In the transformed space the mapped region has a width of $q = (a-e)/2$. Thus, the simulation region is located in the middle of the unit cell with side length e. The complex nature of the transformation is given by the complex parameter γ. Hence, the infinite region $\bar{x}^i \to \pm\infty \pm \mathrm{i}\infty$, according to the analytical continuation, is mapped on the finite unit cell $x^i \to \pm a/2$, respectively.
Since the open system is mapped on independent unit cells, we can expand the fields in Fourier-Floquet series (3.5) and apply the FMM as usual. Then, waveguide problems can be calculated by illuminating the waveguide with one of its fundamental modes. The fundamental mode is just one of the eigenmodes in the first slice of the system and the reflectance and transmittance in this or other waveguide modes can be determined. Furthermore, we can also imagine to use the PML formulation for calculation of the interaction of light with individual nanostructures. A measure for this is the scattering and absorption cross-section of the structure [49]. Hence, the structure is wrapped with the absorbing layers and illuminated by a plane wave. Thus, for each frequency, the scattered field can be determined by putting a contour between the PML region and the structure which collects the scattered field.

Dipole Sources

Instead of illuminating the system by an incident plane wave from outside, we can also excite the system by an electric dipole which is located inside the system at a point in space (x_0^1, x_0^2, x_0^3) [60, 61, 62]. Then, the system is divided into slices such that the dipole source is located in a plane between two slices (e.g. slice l and $l+1$).

The point source is simulated by an oscillating point dipole, modeled by the current density

$$\mathbf{J}(x^1, x^2, x^3) = \mathbf{P}(x^1, x^2, x_0^1, x_0^2)\delta(x^3 - x_0^3). \tag{3.37}$$

Strength, position and orientation of the radiating source is determined by the amplitude vector $\mathbf{P}$. The current density can be included into Maxwell's curl equations (2.2) and this can be translated into the FMM. The difference to the illumination by a plane wave is, that the system is excited from inside. Hence, the amplitudes which would excite the system from outside, $\mathbf{a}^{(0)}$ and $\mathbf{b}^{(N+1)}$, are set equal to zero. Thus, we have to build the scattering matrices in front of and behind the source position, $S(0, l)$ and $S(l+1, N)$. Then, we have to determine the amplitudes of the source at the interface layer which describes the emission of the dipole source. Due to the source term, the tangential fields are not continuous at this interface. Thus, we have to modify the scattering matrix algorithm as we have to include the source by an additional jump discontinuity in the system. The field matching condition (3.23) at the interface is modified to

$$\begin{pmatrix} \mathbf{e}_\parallel^{(l)} \\ \mathbf{h}_\parallel^{(l)} \end{pmatrix}(x^3 = d_l) + \begin{pmatrix} \mathbf{j}_3 \\ \mathbf{j}_3 \\ \mathbf{j}_2 \\ -\mathbf{j}_1 \end{pmatrix}(x^3 = d_l) = \begin{pmatrix} \mathbf{e}_\parallel^{(l+1)} \\ \mathbf{h}_\parallel^{(l+1)} \end{pmatrix}(x^3 = 0), \tag{3.38}$$

with the source representation in Fourier space $\mathbf{j}_\sigma, \sigma = 1, 2, 3$. Additionally, we have to reform the equation for the scattering matrix (3.27) such that we obtain relations between the amplitudes, which account for the missing incident light from outside the system

$$\mathbf{a}^{(l)} = S(0, l)_{12}\mathbf{b}^{(l)}, \quad \mathbf{b}^{(l+1)} = S(l+1, N)_{21}\mathbf{a}^{(l+1)}. \tag{3.39}$$

With these equations the amplitudes at the source interface can be determined. Together with the scattering matrices we can calculate the emitted field of the dipole source.

We can build two different types of dipole sources: Either a single source in the periodic system or a plane of incoherently emitting sources. Due to the periodicity in the FMM, the source appears automatically in all neighboring unit cells. By performing an integration over several sources with different wave vectors we can, due to destructive interference, cancel contributions from all but one source. Consequently, we can effectively simulate a single source in the infinitely periodic system. Similarly, we can locate sources in each unit cell such that we obtain a complete light emitting plane in the system. Since the sources shall emit light incoherently, we skip the part of the integration over the first Brillouin zone. The remaining part of the integration is a sum over the reciprocal lattice vectors. This is the computationally cheaper case, since there is no need for an integration over the wave vector in the first Brillouin zone which would eliminate the neighboring sources.

The single source can be used to describe a quantum dot in a periodic system and the incoherently emitting sources might describe a quantum well layer [61].

If we wrap the unit cell with the source in perfectly matched layers, we can use the computationally "cheaper" incoherently emitting sources to obtain a single point source

per unit cell. Due to the suppressed interaction between the unit cells in this case the source appears as a single point source.

3.3. Chandezon Method

In this section, we discuss another numerical method in the field of diffractive optics, especially in the computation of grating problems. The Chandezon method [17, 63] solves grating problems by transforming the grating surface to a planar interface (see fig. 3.10). Thus, the system is solved in curvilinear coordinates. In these coordinates the grating consists only of two homogeneous regions (below and above the grating). Here, the Rayleigh expansion can be used to describe the fields in these regions.
Therefore, in the Chandezon method the solution of the individual regions is simple. As in the FMM, the fields in the two different regions have to be connected at the interface in order to describe the complete system.
Here, we briefly present the Chandezon method for lamellar gratings which can be treated as two-dimensional systems. The surface of the grating is described by the periodic function $a(x^1)$. Thus, the transformation between the two coordinate systems can be written as

$$\bar{x}^1 = x^1, \tag{3.40a}$$
$$\bar{x}^2 = x^2, \tag{3.40b}$$
$$\bar{x}^3 = x^3 + a(x^1). \tag{3.40c}$$

The metric of the system as defined in eq. (2.60b) is then

$$g^{ij} = \begin{pmatrix} 1 & 0 & -\partial_1 a \\ 0 & 1 & 0 \\ -\partial_1 a & 0 & 1 + (\partial_1 a)^2 \end{pmatrix}. \tag{3.41}$$

In two dimensional systems Maxwell's equations decouple in E- and H-polarization (see section 2.3). Since Maxwell's equations are solved in the homogeneous regions, we can write the equations for both polarizations with one notation in the curvilinear space

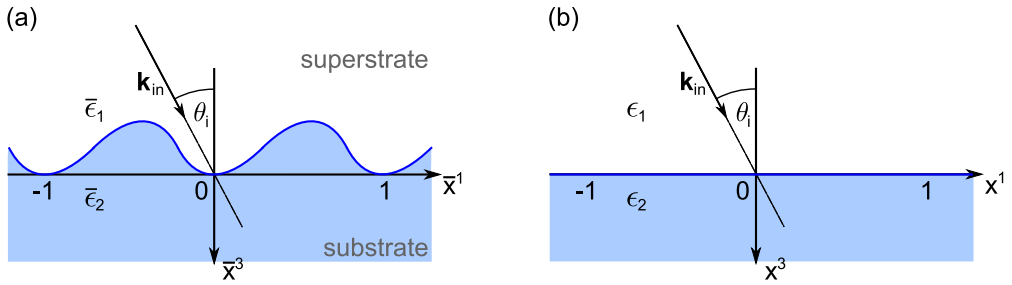

Figure 3.10.: (a) Grating in the Cartesian system $O\bar{x}^1\bar{x}^2\bar{x}^3$. (b) Transformed grating in the curvilinear coordinate system $Ox^1x^2x^3$ where the grating surface is a plane.

as

$$\begin{aligned} \partial_3 G - \partial_1 G' &= \mathrm{i}\bar{\epsilon}\omega^2 F, && (3.42a)\\ -\partial_3 F &= -\mathrm{i}G + \mathrm{i}(\partial_1 a)G', && (3.42b)\\ \partial_1 F &= \mathrm{i}(\partial_1 a)G - \mathrm{i}\left(1 + (\partial_1 a)^2\right) G'. && (3.42c) \end{aligned}$$

In these equations the permittivity $\bar{\epsilon}$ is given in the Cartesian system instead of the curvilinear one and therefore marked with the bar $^-$. The fields for both polarizations are described by the parameters F, G and G' as

- $F = E_2$, $G = -\omega H_1$ and $G' = -\omega H_3$ for E-polarization,
- $F = H_2$, $G = \bar{\epsilon}\omega E_1$ and $G' = \bar{\epsilon}\omega E_3$ for H-polarization.

With this notation we can solve the eigenvalue equation for both polarizations in one calculation. As in the FMM we transform the fields with the Rayleigh expansion into Fourier space (see eq. (3.5))

$$\begin{aligned} F(x^1, x^3) &= \sum_{m=1}^{N} f_m(x^3)\mathrm{e}^{\mathrm{i}\alpha_m x^1}, && (3.43a)\\ G(x^1, x^3) &= \sum_{m=1}^{N} g_m(x^3)\mathrm{e}^{\mathrm{i}\alpha_m x^1}, && (3.43b)\\ G'(x^1, x^3) &= \sum_{m=1}^{N} g'_m(x^3)\mathrm{e}^{\mathrm{i}\alpha_m x^1} && (3.43c) \end{aligned}$$

and truncate the Fourier space to a total of N coefficients.
Via the correct Fourier factorization [43, 64] we obtain for Maxwell's equations in Fourier space

$$\begin{aligned} \partial_3 \mathbf{g} - \mathrm{i}\hat{\alpha}\mathbf{g}' &= \mathrm{i}\bar{\epsilon}\omega^2 \mathbf{f}, && (3.44a)\\ -\partial_3 \mathbf{f} &= -\mathrm{i}\mathbf{g} + \mathrm{i}\left[\!\left[\partial_1 a\right]\!\right]\mathbf{g}', && (3.44b)\\ \hat{\alpha}\mathbf{f} &= \left[\!\left[\partial_1 a\right]\!\right]\mathbf{g} - \left(\mathbb{1} + \left[\!\left[\partial_1 a\right]\!\right]\left[\!\left[\partial_1 a\right]\!\right]\right)\mathbf{g}'. && (3.44c) \end{aligned}$$

These three equations can be combined to a single second order differential equation

$$\left(\mathbb{1} + \left[\!\left[\partial_1 a\right]\!\right]\left[\!\left[\partial_1 a\right]\!\right]\right)\partial_3\left(-\mathrm{i}\partial_3 \mathbf{f}\right) - \left(\left[\!\left[\partial_1 a\right]\!\right]\hat{\alpha} + \hat{\alpha}\left[\!\left[\partial_1 a\right]\!\right]\right)\partial_3 \mathbf{f} = \mathrm{i}\hat{\gamma}^2 \mathbf{f} \tag{3.45}$$

with

$$\hat{\gamma}^2 = \bar{\epsilon}\omega^2 - \hat{\alpha}^2. \tag{3.46}$$

In order to linearize this second order differential equation to a first order eigenvalue problem, we introduce the new parameter $\mathbf{f}'$ which is the derivative of the field $\mathbf{f}$ as

$$\mathbf{f}' = -\mathrm{i}\partial_3 \mathbf{f}, \tag{3.47}$$

and we build the eigenproblem matrix by eqs. (3.45) and (3.47) as

$$\frac{1}{q}\begin{pmatrix}\mathbf{f}\\ \mathbf{f}'\end{pmatrix} = M\begin{pmatrix}\mathbf{f}\\ \mathbf{f}'\end{pmatrix}, \tag{3.48}$$

with the matrix

$$M = \begin{pmatrix} -(\hat{\gamma}^2)^{-1}\left(\llbracket\partial_1 a\rrbracket\,\hat{\alpha} + \hat{\alpha}\,\llbracket\partial_1 a\rrbracket\right) & (\hat{\gamma}^2)^{-1}\left(\mathbb{1} + \llbracket\partial_1 a\rrbracket\,\llbracket\partial_1 a\rrbracket\right)\\ \mathbb{1} & 0\end{pmatrix}. \tag{3.49}$$

By the ansatz $(\mathbf{f},\mathbf{f}') = \mathbf{\Phi}\mathrm{e}^{\mathrm{i}qx^3}$, we can write eq. (3.48) as following eigenproblem

$$\frac{1}{q}\mathbf{\Phi} = M\mathbf{\Phi}. \tag{3.50}$$

We solve this eigenvalue problem in the super- and substrate region and receive for each region $2N$ eigenvalues q^{-1} in the curvilinear system. N eigenvalues belong to the modes propagating upwards and N modes propagate downwards. The eigenvalues converge for large N to the inverse of the analytical values γ_n, which are the components of the diagonal matrix $\hat{\gamma}$ in eq. (3.46).
In order to improve the convergence of the method and for easier identification of the propagating modes in the reflected and transmitted fields with the spatial harmonics, we determine the propagating modes in the super- and substrate region of the system by the exact values. This means, that we replace all real eigensolutions by their Rayleigh counterparts which garantees convergence of these solutions [63, 64].
Thus, we divide the eigenmodes into two groups: one consisting of the propagating modes U and the other one of the evanescent modes V. Then, the field expansion in eq. (3.43a) reads

$$F = \sum_{n\in U} A_n \mathrm{e}^{\mathrm{i}\alpha_n\bar{x}^1 + \mathrm{i}\gamma_n\bar{x}^3} + \sum_{m=1}^{N}\mathrm{e}^{\mathrm{i}\alpha_m x^1}\sum_{n\in V}\Phi_{mn}C_n\mathrm{e}^{\mathrm{i}q_n x^3}, \tag{3.51}$$

with the amplitudes A_n of the propagating modes and C_n of the evanescent modes. In this equation, the expansion of the propagating modes is written in the Cartesian space. The remaining modes, which are the evanescent modes, are taken directly by the solution of the eigenvalue problem Φ in eq. (3.50) which is solved in the curvilinear space. For the calculation (especially for the field matching at the interface), we have also to transform the contribution of the propagating modes in the curvilinear space, i.e.,

$$F(x^1,x^2,x^3) = \sum_{m=1}^{N}\mathrm{e}^{\mathrm{i}\alpha_m x^1}\left(\sum_{n\in U}L_{m-n}(\gamma_n)A_n\mathrm{e}^{\mathrm{i}\gamma_n x^3} + \sum_{n\in V}\Phi_{mn}C_n\mathrm{e}^{\mathrm{i}pq_n x^3}\right) \tag{3.52}$$

with the operator

$$L_m(t) = \int_0^1 \mathrm{d}u\,\mathrm{e}^{\mathrm{i}ta(u)-\mathrm{i}2\pi mu}. \tag{3.53}$$

This operator performs the change of the Fourier basis from the Cartesian to the curvilinear system.
In order to match the fields at the interface, we use the continuity of the F component. However, we need a second field component, since we have more than N unknown coefficients, which have to be determined. Consequently, we use a second continuous component which is G. The Fourier vector of G is determined by eqs. (3.44) and (3.47) as

$$\mathbf{g} = -[\![\partial_1 a]\!]\,\hat{\alpha}\mathbf{f} + (\mathbb{1} + [\![\partial_1 a]\!]\,[\![\partial_1 a]\!])\,\mathbf{f}'. \tag{3.54}$$

At the interface we have to distinguish between the two different polarizations of the incident light. In the case of E-polarization G, is continuous while in the case of H-polarization $G/\bar{\epsilon}$ is continuous. Similarly to the Fourier Modal Method, we match the corresponding fields at the interface and calculate an interface matrix which couples the amplitudes at this interface.
In order to obtain transmitted and reflected fields, we have to determine the incident plane wave in the curvilinear system, as well. It reads

$$\begin{aligned} F^{\text{inc}} &= F_0 \mathrm{e}^{\mathrm{i}k_{\text{in}}\bar{x}^3\cos\theta_{\text{i}} + \mathrm{i}k_{\text{in}}\bar{x}^1\sin\theta_{\text{i}}} \\ &= F_0 \sum_{m=1}^{N} L_m(\beta_0)\mathrm{e}^{\mathrm{i}\left(\alpha_m x^1 + \beta_0 x^3\right)}, \end{aligned} \tag{3.55}$$

with $L_m(\beta_0)$ defined by eq. (3.53). Thus, we can also determine the G component of the incident light as

$$G^{\text{inc}} = \sum_{m=1}^{N} \left(\beta_0 - \frac{\alpha_0}{\beta_0} mK\right) L_m(\beta_0)\mathrm{e}^{\mathrm{i}(\alpha_m x^1 + \beta_0 x^3)}. \tag{3.56}$$

If we have a multilayer system, we have to build a scattering matrix in order to ensure numerical stability of the system [47]. By the scattering matrix, we can determine the reflected and transmitted fields of the system as in the FMM.
In the case of multilayer systems, the interfaces can have different shapes. Thus, each interface determines its own coordinate transformation [42]. Due to the different curvilinear coordinates in the system, the computation of such gratings means additional computational costs for the Chandezon method, since we have to transform between these coordinates to match the fields at the interfaces.
The advantage of the Chandezon method over the Fourier modal method is to avoid slicing and to reduce the number of eigenvalue problems which have to be solved due to the slicing. However, in the case of multilayer gratings with arbitrary shapes the change between the different coordinate systems can be very expensive in the computations.

3.4. Discussion

Finally, we conclude this chapter with a short discussion about the Fourier Modal Method, its applications and a comparison with the Chandezon method. First, we address the slicing in the FMM which is performed by the staircase approximation.

In the case of metallic systems, e.g., metallic gratings with the shape as illustrated in fig. 3.1, the staircase approximation can lead to many sharp corners which cause lightning rod effects as known in the FDTD method [65]. Thus, we have to be careful with the slicing in metallic systems and check the results carefully if the observed effect is not an artifact due to the slicing. In such a system the Chandezon method would circumvent this effect by avoiding the slicing. Unfortunately, the Chandezon method needs an analytical form of the grating surface to perform the coordinate transformation which restricts the general use of this method.
The staircase approximation is a crucial part of the FMM when dividing the system into the smaller subsystems, the slices. This approximation is also applied in the Fourier transformation, when the structure in the slice is mapped on a zigzag contour to perform the Fourier transform in the x^1x^2-plane as shown in fig. A.2. This effect is reduced in chapter 5 by the application of special coordinates which are adapted to the geometry of the problem.
In this chapter, we have shown that the FMM enables us to calculate the reflectance and transmittance spectra for periodic nanostructures as well as the field distributions in these structures. However, the field computation can become very expensive, since we have to calculate the scattering matrix before and behind each slice inside which we want to obtain the field distribution (see section 3.2.6).
Thus, slicing reduces our problem to two-dimensional subsystems which can save an enormous amount of computer memory in comparison to volume methods. However, the layer-by-layer calculations become very time consuming for systems with many slices. As a compensation of this disadvantage, the FMM performs all computations in frequency domain. Consequently, single frequencies of the spectrum can be calculated independently on several machines. Thus, entire spectra can be obtained within reasonable time frames, if sufficient computer resources are provided, even if the calculation of individual frequencies takes very long.

4. Photonic Crystals

In the following, we use the FMM for the investigation of the optical properties of photonic crystals. For such systems the FMM is particularly well suited since they can be assumed as infinitely periodic in a plane whilst being finite in the third direction. Thus, we can obtain the optical properties of such systems irradiated along the third direction with a plane wave.
We start this chapter with a short general introduction to photonic crystals. Then, we discuss two example structures: Woodpile and opal photonic crystals. The investigated woodpile photonic crystals are made of silicon and with a proper design, they can exhibit a complete photonic band gap. Furthermore, it is possible to incorporate functional elements, such as cavities and waveguides, into such photonic crystals. The aim is to design optical circuits, by combining these building blocks. We show numerically calculated results of such elements with the FMM. In order to ensure the required periodicity of the FMM, we perform supercell calculations. Finally, we also compare calculated results with measured spectra of an experimentally realized woodpile photonic crystal exhibiting a band gap at 1.5μm and of a waveguide in a woodpile photonic crystal. Towards the end of this chapter, we also investigate the polarization properties of opal photonic crystals and compare the results to measurements on such opal films.

4.1. Fundamentals of Photonic Crystals

In 1987, a new type of artificial optical material was suggested which later became generally known as photonic crystals. E. Yablonovitch suggested that dielectric systems which exhibit a full three-dimensional spatial periodicity can inhibit spontaneous emission [2] and S. John discussed that such materials can be used to demonstrate Anderson localization for photons [1].
Photonic crystals are dielectric structures with a periodic permittivity distribution. The periodicity can exist in one, two or even all three spatial directions. The modulation is on a length scale comparable to the desired wavelength of operation. This periodicity influences the propagation properties of light in the crystal. The waves existing inside the crystal have to obey the Bloch theorem (see section 2.8.1). By multiple interference of waves scattered from each unit cell of the structure, stopbands may open. This means, light with specified frequencies is prevented from propagating in at least one direction inside the crystal. If the stopbands overlap for all propagation directions, the frequency region is called a photonic band gap.
Spectral regions for which no propagation is allowed in all directions and, additionally, for both polarizations are called complete photonic band gaps. There, no propagating

electromagnetic modes exist inside the photonic crystal. Whether a band gap opens depends on the considered geometry as well as on the permittivity contrast of the crystal. Also, the band gap's frequency range depends on these properties.
Such nanostructured materials are also found in nature where this type of material is responsible for e.g. the colorful appearance of some butterflies. Their wings are made of natural photonic crystals [66]. Also the beautiful appearance of natural opals is attributed to the diffraction by the lattice of spheres [67].
Since photonic crystals are fabricated artificially, they can be designed to meet some desired optical properties. We discuss in this chapter two examples for three-dimensional photonic crystals: woodpile photonic crystals in section 4.2 and opal photonic crystals in section 4.3.

4.2. Woodpile Photonic Crystals

The woodpile structure has been suggested in 1994 by Ho *et al.* [68]. Bandstructure calculations show that woodpiles can exhibit a complete photonic band gap if the refractive index contrast of the two materials is larger than 1.9. As illustrated in fig. 4.1, the structure consists of periodically stacked rods. In this case, the rods form a fcc lattice with two-atomic basis.

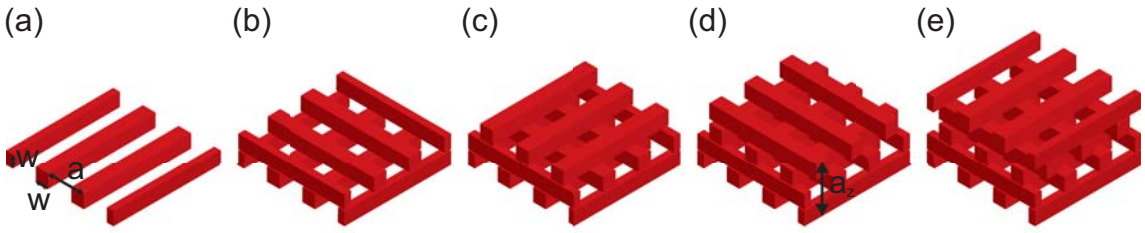

Figure 4.1.: Woodpile photonic crystal consisting of bars with quadratic cross section.

First, we consider a woodpile photonic crystal made of silicon rods ($\epsilon = 11.9$) with quadratic cross sections (see fig. 4.1). The corresponding bandstructure is shown in fig. 4.2. The dark-blue shaded area depicts the complete photonic band gap.
In the calculation, we use a center-to-center separation of the parallel quadratic rods of $a = 1000$nm which is also the lattice constant in the unit cell of the FMM. Thus, the lattice constant in the fcc lattice is $a_{\text{fcc}} = \sqrt{2}a \approx 1414.2$nm. The rods are stacked on top of each other. Due to the fcc geometry the rods have a width and height of $w = \frac{a}{2\sqrt{2}} \approx 353.6$nm. Thus, the period of the system in z-direction is $a_z = \sqrt{2}a$. Woodpiles with quadratic rod cross-section are fabricated in the Noda group by a stacking technique [69].
Alternatively, woodpile photonic crystals with elliptical rod cross-section can also exhibit a complete photonic band gap [70] (see also section 4.2.4). Such structures can be realized by direct laser writing as reported in ref. [71]. Here, the directly written woodpile is a polymer template with refractive index $n = 1.56$ of the rods. Thus, it does not possess the desired band gap. However, by a double inversion process the polymer can be replaced by silicon [72]. This structure finally exhibits a complete

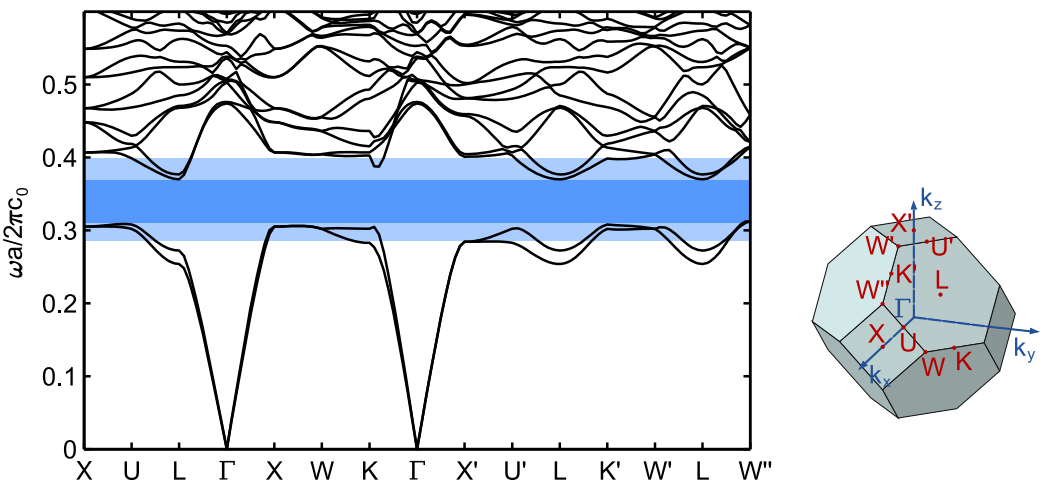

Figure 4.2.: Bandstructure of woodpile photonic crystal with silicon bars, calculated by Christian Wolff with the plane wave method, and corresponding first Brillouin zone.

photonic band gap. Alternative fabrication methods of woodpiles with elliptical rod cross-sections have also been presented. In refs. [73, 74] woodpile photonic crystals have been fabricated by laser interference lithography.
Both, woodpiles with quadratic and elliptical rod cross-section show closely similar effects. The difference in the calculation by the FMM is the slicing: In the elliptical rod case we use many equidistant slices, whereas in the quadratic rod case, we can use the natural slicing given by the four rods per period in z-direction.
In section 4.2.4, we discuss woodpiles consisting of elliptical rods. Here, we calculate the spectrum for a woodpile with a complete band gap at telecommunication wavelengths [75]. Additionally, we investigate a waveguide in such a woodpile which we compare to experimentally realized structures [76]. However, first we study woodpiles with quadratic rods and incorporated cavities and waveguides built by these cavities.

4.2.1. Linear Optical Properties

In transmittance and reflectance calculations with the FMM, we investigate a woodpile which is finite in z-direction. The bars are oriented along the x- and y-direction. Then, the unit cell is formed by stacking four rods on top of each other (see fig. 4.1). Here, the first rod in the unit cell is oriented along the y-axis. Finally, we stack 5 of these unit cells on top of each other, leading to a woodpile consisting of 20 rod layers. In the lateral direction, we use a Fourier expansion with 97 Fourier coefficients, to obtain converged results. The z-direction in our calculation corresponds to perpendicular incidence. In the first Brillouin zone we can identify the perpendicular incidence with wave vectors orientated along the $\Gamma X'$-direction.
The crystal is completely surrounded by vacuum. Thus, the spectra for perpendicular incidence in x- and y-polarization are identical. In fig. 4.3, one can see the stopband of

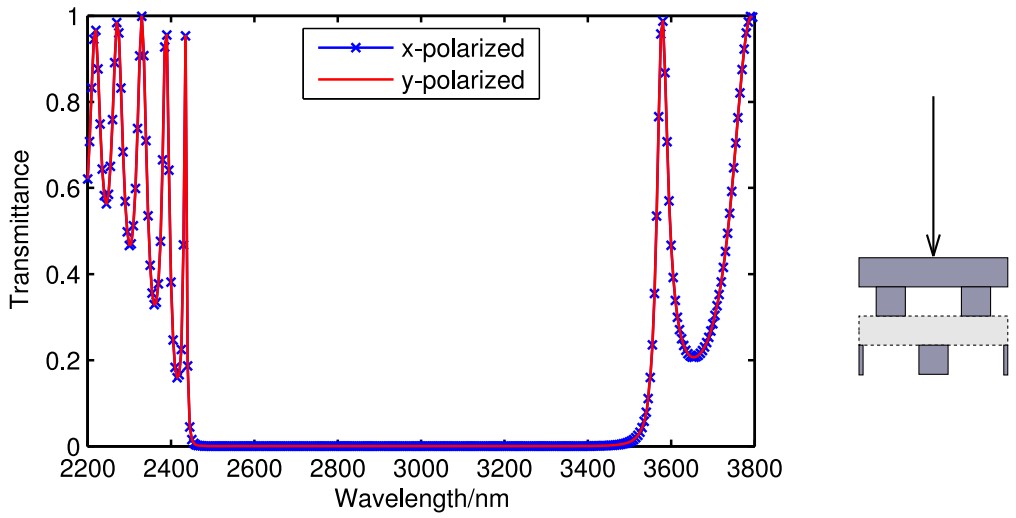

Figure 4.3.: Transmittance spectrum for perpendicular incidence on a woodpile in vacuum.

the woodpile in $\Gamma X'$- direction as well as the Fabry-Pérot oscillations on both sides of the stopband due to the finite structure in propagation direction. The position of the stopband changes, if we alter the angle of incidence, e.g., to $\theta = 30^o$. We obtain two different stopbands for s- and p-polarized light as shown in fig. 4.4 (a). Additionally, the edges of the stopband shift with respect to the normal incidence case in fig. 4.3.
If the woodpile is placed on a glass substrate, the symmetry in the x- and y-polarization for perpendicular incidence is broken. Additionally, in fig. 4.4 (b), we can observe a small shift in the Fabry-Pérot oscillations. The glass substrate is approximated by a glass half-space with permittivity $\epsilon = 2.25$.

4.2.2. Cavities

A point defect in a photonic crystal can act as cavity, supporting discrete modes within the band gap. The mode frequencies show up in the bandstructure as flat bands with frequencies located inside the band gap. Additionally in contrast to the infinitely extended Bloch modes, the mode profiles of these bands are localized at the cavity. These cavity modes can be seen in the transmittance spectrum as resonance peaks in the band gap of the photonic crystal [77]. If the incident light can couple to the parts of the mode which leak out of the cavity, it can propagate through the finite crystal although the frequency is located in the band gap. The localization of the mode in the cavity is measured by the quality factor Q. It is a measure for the energy loss out of the cavity, that can be determined as described in the following section.

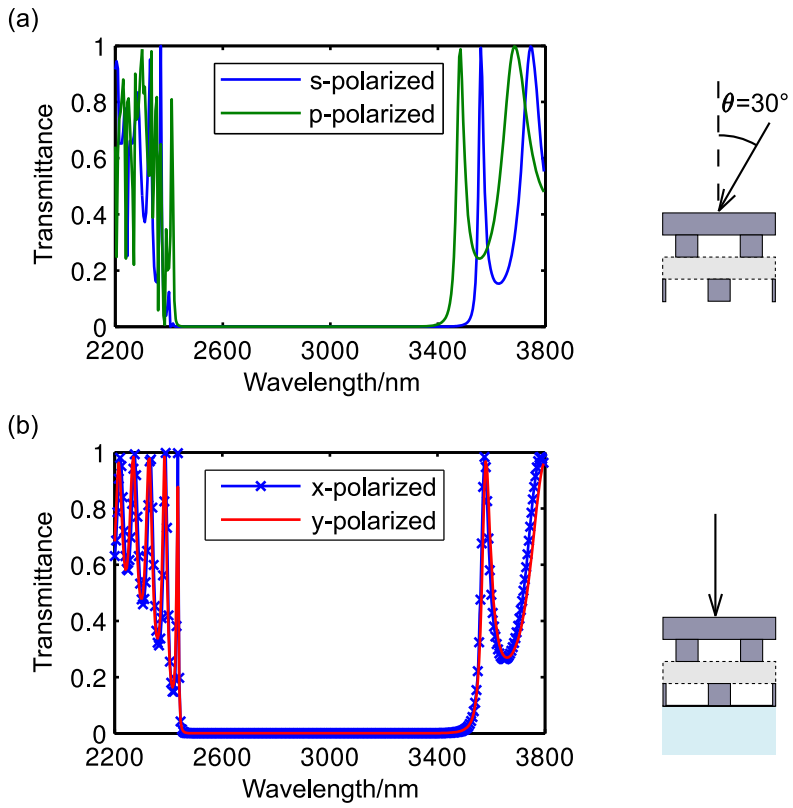

Figure 4.4.: (a) Transmittance spectrum for oblique incidence with $\theta = 30^o$ on woodpile in vacuum. (b) Transmittance spectrum for perpendicular incidence on woodpile situated on a glass substrate.

Quality Factor

The resonance observed in the spectrum can be easily fit to a Lorentzian shape (see fig. 4.5) which is given by

$$g(\nu) = \frac{\Delta\nu}{2\pi} \frac{1}{(\nu - \nu_o)^2 + (\Delta\nu/2)^2}. \tag{4.1}$$

The full width at half maximum of the curve is given by $\Delta\nu$, and ν_o describes the resonance frequency. These parameters can be obtained by fitting the numerical transmittance data. The quality factor is defined as

$$Q = \frac{\nu_o}{\Delta\nu}. \tag{4.2}$$

FMM Calculations

Since a point defect destroys the periodicity, which is a necessity of the FMM, we use the supercell method. This means, we arrange the defect on a periodic lattice with N_{sc}-times larger lattice constant than in the undisturbed photonic crystal. By choosing

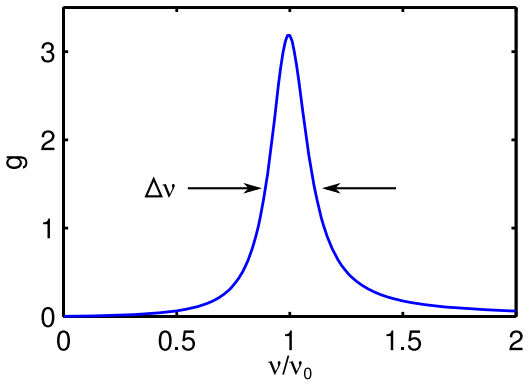

Figure 4.5.: Lorentzian shaped resonance with resonance frequency ν_0 and width $\Delta\nu = 0.2\nu_o$.

the supercell large enough, we ensure that the cavity mode is localized to the cavity and does not interact with the neighboring cavity modes. This means the cavities which are arranged on a periodic lattice can be regarded as isolated cavities in the system. In fig. 4.6 we have illustrated supercells with $N_{\text{sc}} = 3, 4$ and 5. Always, one cell of the supercell contains a defect. Compared to the ordinary unit cell, we need more Fourier coefficients in the Fourier expansion of the individual slices, because the ratio of bar thickness and unit cell size decreases, due to the increased unit cell. In detail, we use a total of 1185 Fourier coefficients for a 5×5 supercell in the following calculations. The increase of the unit cell by the supercell factor results also in a decrease of the first Brillouin zone in the reciprocal space by the same factor. The reciprocal lattice vectors become shorter (2.68). Thus, we obtain in the transmittance and reflectance

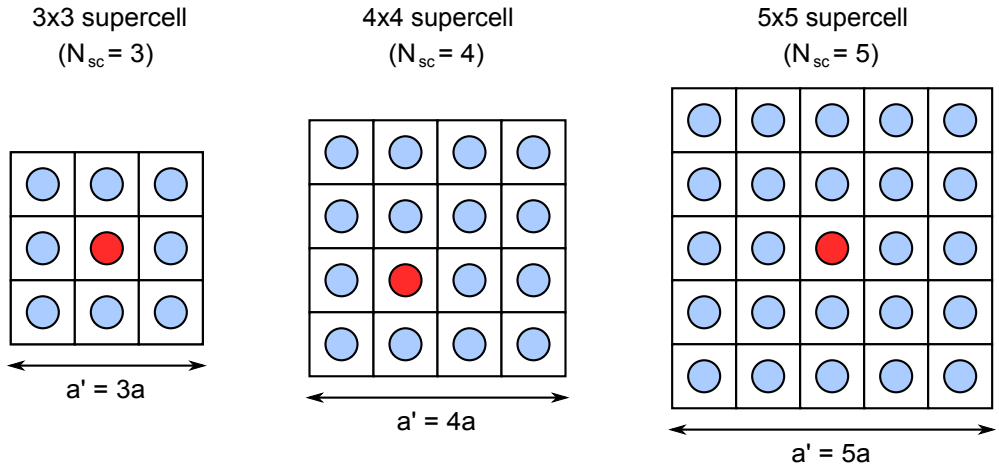

Figure 4.6.: Different supercells with red marked defect in a single cell. a' denotes the lattice constant of the supercell and a is the lattice constant of the conventional unit cell.

spectra additional higher diffraction orders as can be deduced from eq. (3.22).

Point Defect in Woodpile Photonic Crystal

Design

As point defect we choose to remove a rod crossing in the woodpile. The defect size is 500nm corresponding to half of the lattice constant as depicted in fig. 4.7.

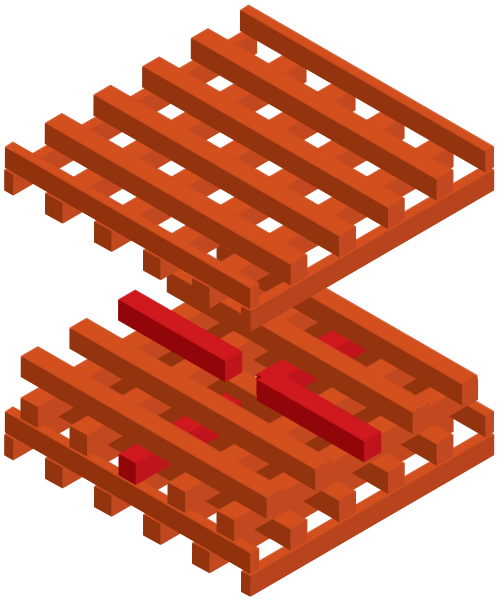

Figure 4.7.: 5×5 supercell ($N_{\mathrm{sc}} = 5$) of a woodpile photonic crystal with a missing rod crossing in the middle acting as cavity.

Bandstructure

First, we discuss the bandstructure for the woodpile with the included cavity. Here, we also apply the supercell method leading to an increased unit cell by a factor of $N_{\mathrm{sc}} = 5$ in all three periodic directions.
The calculated bandstructure, shown in fig. 4.8, reveals the existence of three defect bands. In the plot only two defect states are visible but the mode at higher frequency is doubly degenerate. Since the Brillouin zone in this bandstructure is N_{sc}-times smaller than the one of the primitive unit cell, the bands are folded back into the smaller zone of the supercell which leads to the appearance of so many bands below and above the band gap.

Spectrum

In order to calculate the spectrum we use a supercell of $N_{\mathrm{sc}} = 5$ as in the bandstructure calculations. The defect is placed in the middle of the woodpile, meaning that the two rods with the point defect are in the 10th and 11th rod layer of the woodpile. Thus, the point defect is surrounded by nine layers on top and nine layers on bottom. We choose

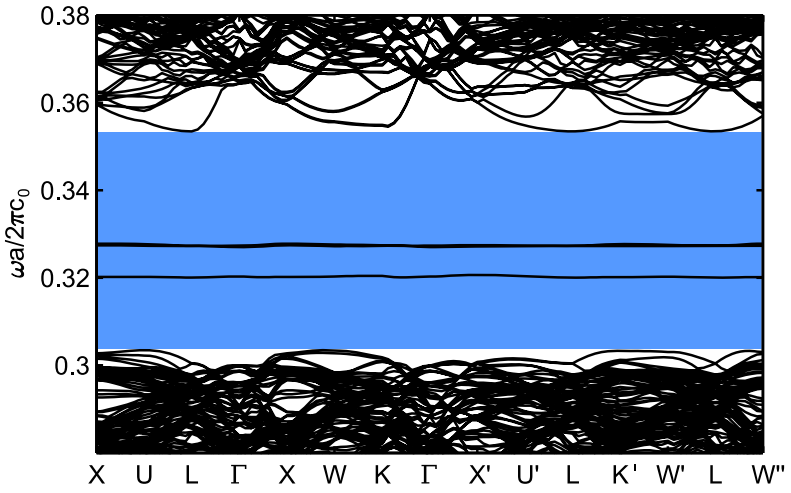

Figure 4.8.: Calculated band structure for a woodpile photonic crystal with a cavity ($N_{sc} = 5$). Within the band gap (blue-shaded area) three defect bands occur. The calculation has been performed by Christian Wolff.

that the first rod with the defect, in the 10th rod layer of the woodpile, is oriented along the x-axis. Consequently, the lower rod with defect (in the 11th rod layer) points along the y-axis.
The spectrum of the woodpile with a point defect for perpendicular incidence shown in fig. 4.9 exhibits a peak in the middle of the stopband. The transmittance into the

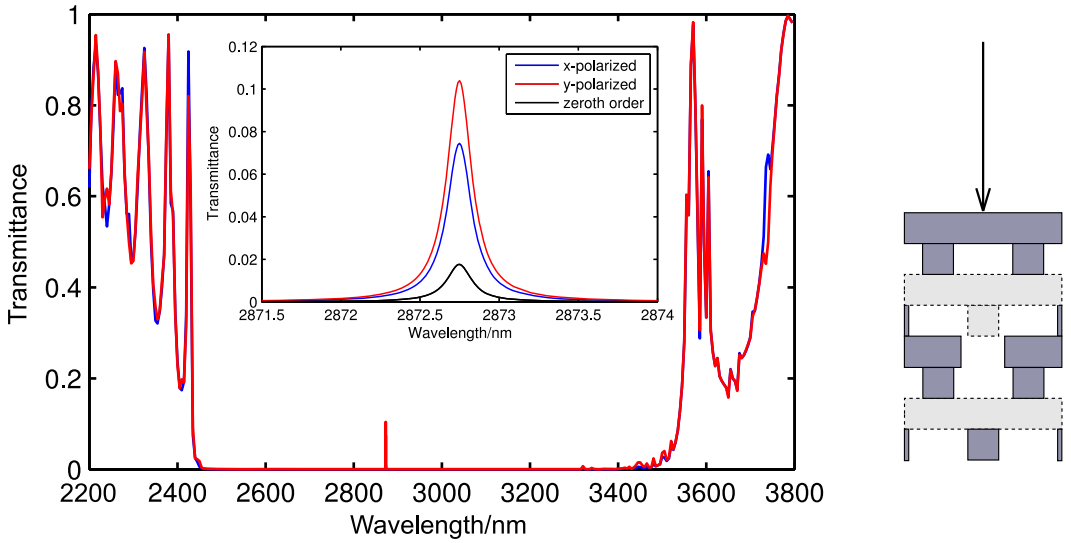

Figure 4.9.: Spectrum for perpendicular incidence of the woodpile with a point defect. The inset shows a zoom-in to the resonance. The light scattered into zeroth diffraction order is depicted by the black line.

zeroth order is identical for x- and y-polarization (black curve), but the transmittance summed over all diffraction orders is larger for x-polarized incidence (blue curve) than for y-polarized incidence (red curve). In most experiments the transmittance into the zeroth order is the relevant quantitiy. The resonance wavelength for both polarizations is $\lambda = 2872.75\text{nm}$ and for the quality factor we obtain $Q = 15\,000$.
Figure 4.10 and 4.11 show the electric field distribution inside the photonic crystal. The

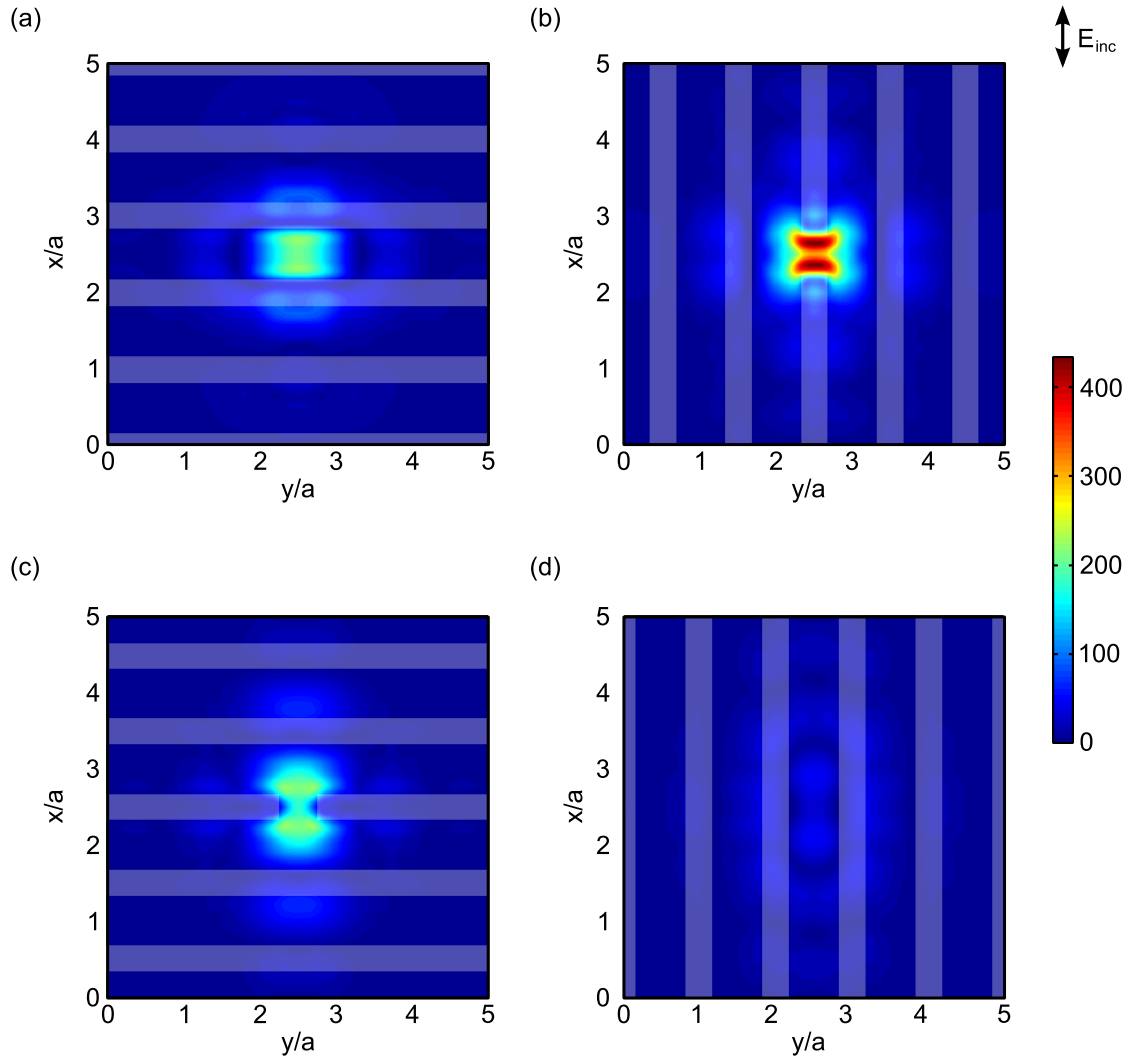

Figure 4.10.: Electric field strength $|\mathbf{E}|$ relative to the electric field strength of the incident plane wave $|\mathbf{E}_{\text{inc}}|$ (see colorbar) in the 5×5 supercell with the cavity in the middle. The wavelength is $\lambda = 2872.75\text{nm}$ for x-polarized incident light as indicated by the black arrow. (a) shows the field distribution in the layer above the first defect layer. (b) shows the field in the upper defect rod, (c) in the lower defect rod, and (d) in the rod layer below the point defect.

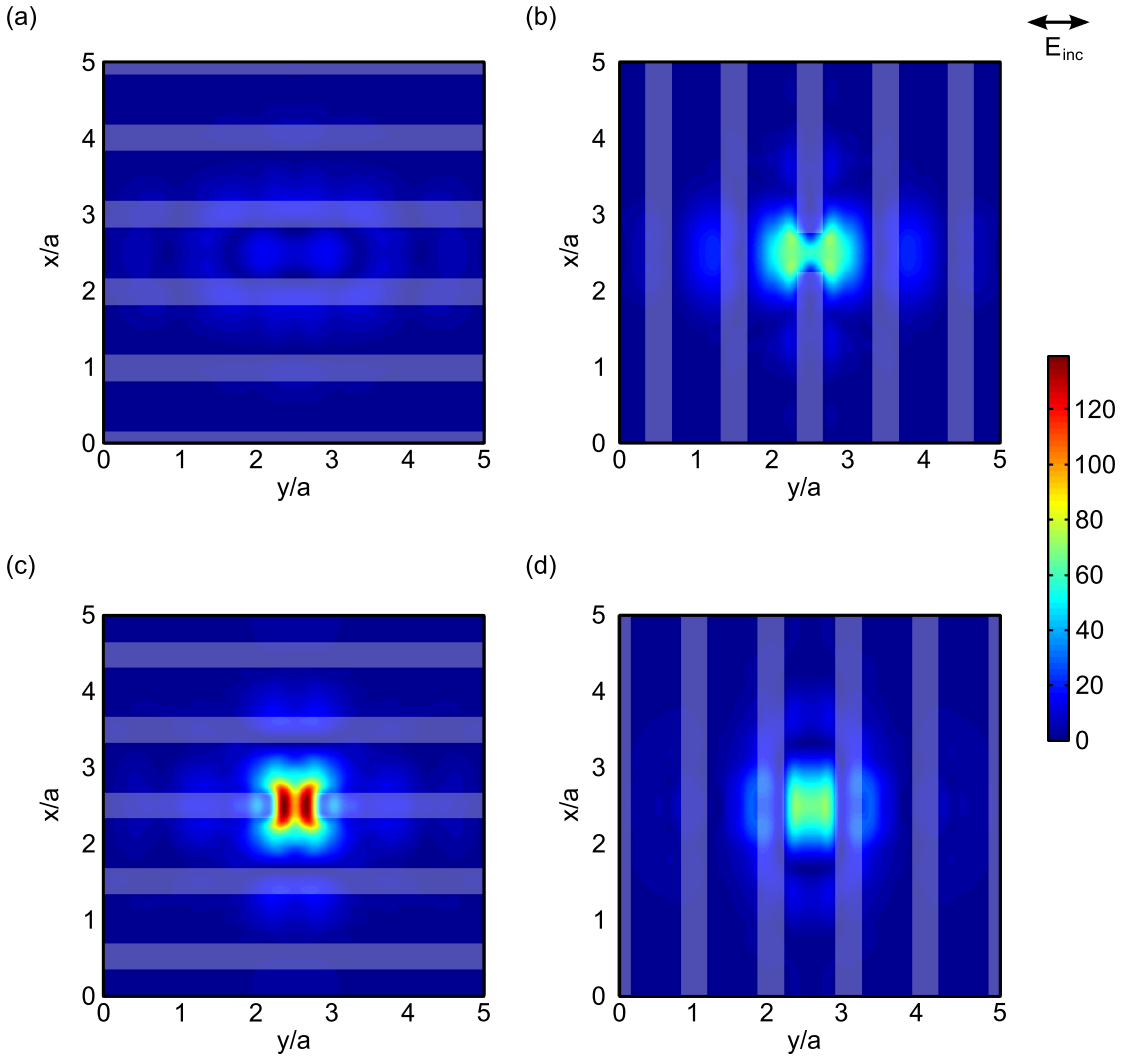

Figure 4.11.: Relative electric field strength as in fig. 4.10 but for y-polarized incident light indicated by the black arrow.

fields are calculated in the middle of the rod layers related to the point defect. If the cavity mode is excited with an x-polarized incident plane wave, the electric field has its maximum in the upper rod of the point defect (fig. 4.10). Because this cavity mode is degenerate (as we know from bandstructure calculations), we can couple to the second mode by y-polarized light (fig. 4.11). This mode has its field maximum in the lower part of the defect. As the transmittance through the cavity is higher for x-polarized light, also the field in the cavity is roughly a factor of three higher as compared to the field excited by y-polarized light.
Due to the bandstructure calculation and the mode profiles obtained from these calculations (not shown here), we anticipate that the third defect mode can only be excited by an electric field with field components pointing in z-direction. In order to obtain

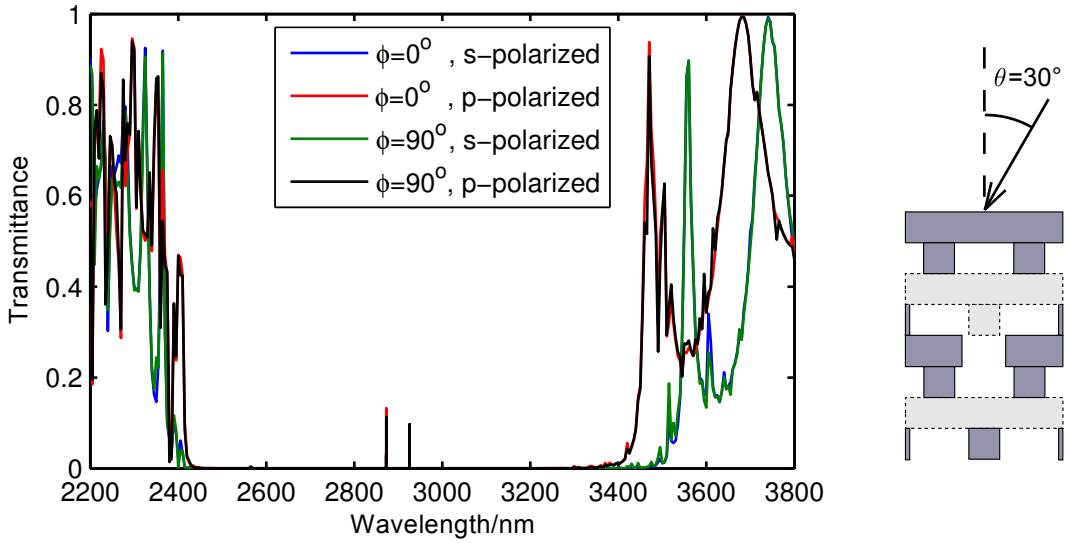

Figure 4.12.: Defect spectrum for oblique incidence with $\theta = 30^o$ on woodpile in vacuum as marked in the small figure on the right hand side of the spectrum.

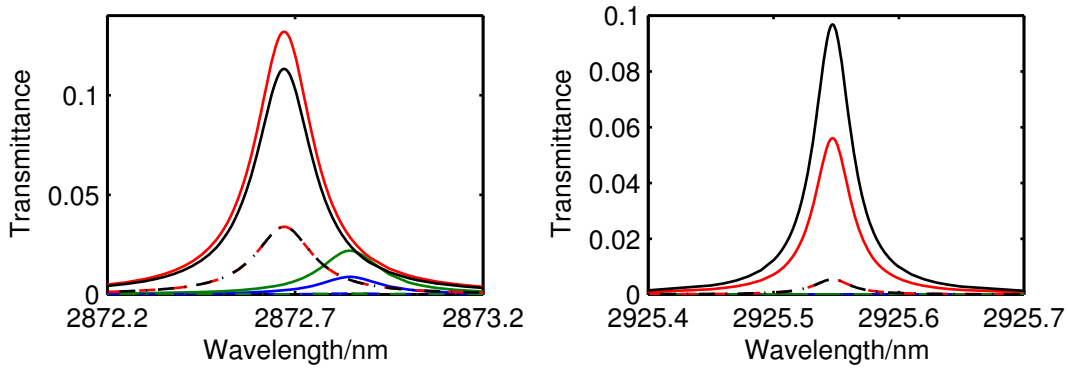

Figure 4.13.: Zoom into the spectral region of the two resonances for oblique incidence with $\theta = 30^o$ on woodpile in vacuum with same color code as in fig. 4.12. The dashed lines show the transmittance into the zeroth order, respectively.

such an electric field by the incident plane wave, the woodpile has to be illuminated with p-polarized light under oblique incidence. As a consequence, the incident electric field vector has a component in z-direction. Figure 4.12 shows the calculated spectra for incidence with $\theta = 30^o$ in p- and s-polarization. In these spectra, two different defect modes are present: (i) the degenerate mode at around $\lambda = 2872.7$nm shown in fig. 4.13 (a) and (ii) the new mode at $\lambda = 2925.547$nm shown in fig. 4.13 (b). Due to the oblique incidence the transmittance into the zeroth order is no longer identical for the different polarizations. We also obtain a small splitting of $\Delta\lambda = 0.175$nm in s- and p-polarized incidence for the degenerate mode. As expected, the new mode is only visible in p-polarization. The quality factor for this mode is $Q = 81\,700$. As shown in

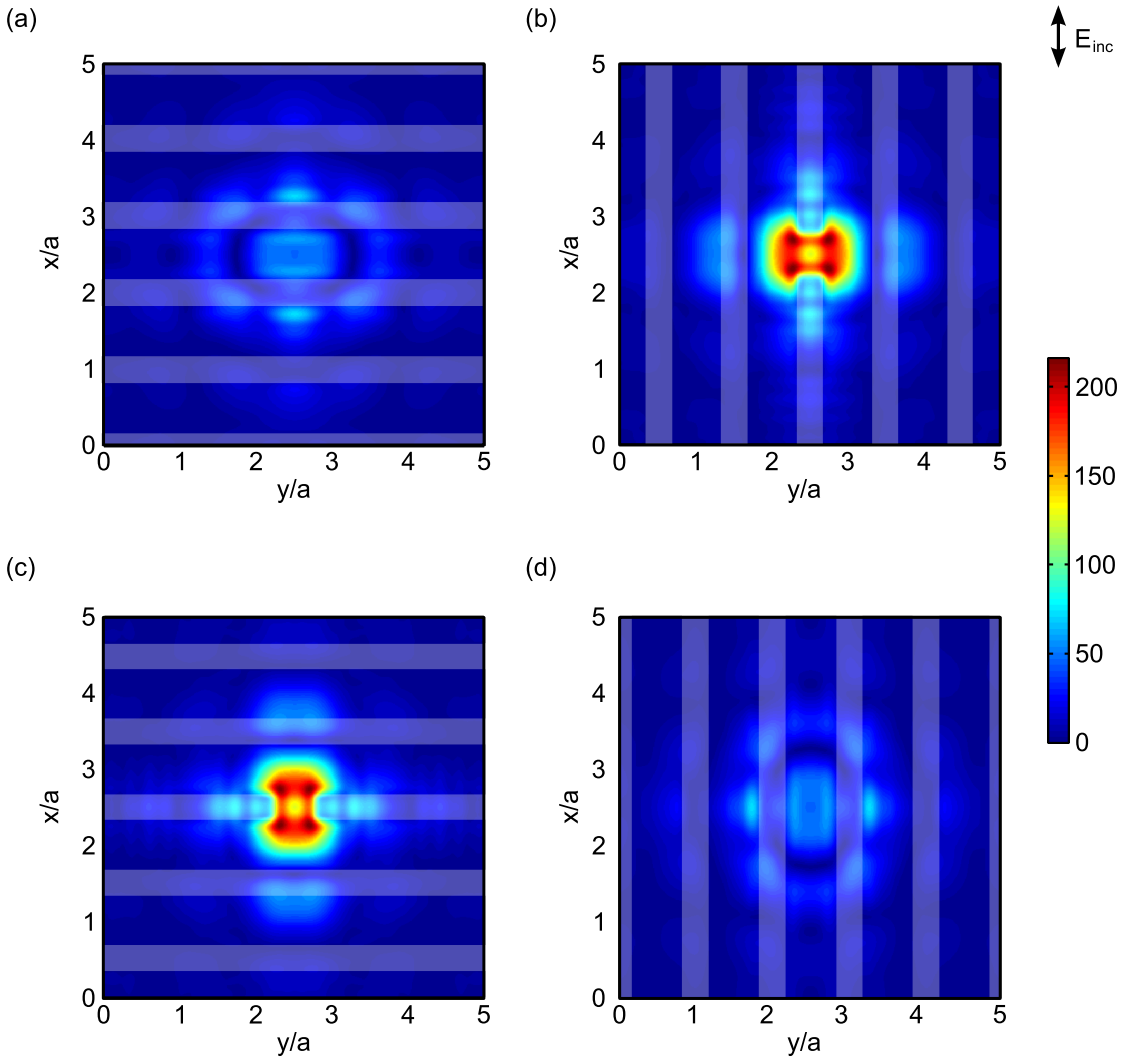

Figure 4.14.: Relative electric field strength as in fig. 4.10 at $\lambda = 2925.547$nm with $\theta = 30^o$ in p-polarization and $\phi = 0^o$ (as indicated by the black arrow).

fig. 4.14, the field distribution of the new mode is quite different from the field of the degenerate modes. The field is equally distributed among the two defect layers.
In experiments the photonic crystals are mainly situated on substrates such as glass substrates with refractive indices different from one. It is important to stress, how this affects the optical properties. As already observed for the undisturbed woodpile in fig. 4.4 (b), the transmittance into zeroth diffraction order is not identical for the two polarizations, anymore. Thus, the degeneracy of the cavity mode is lifted and the resonance frequency is slightly different for both polarizations.
The degeneracy can also be lifted if the point defect is not located in the middle of the woodpile. Consequently, this also leads to a small splitting in the resonance frequency.

4.2.3. Waveguides in Woodpile Photonic Crystal

The cavities of the preceding section can be arranged such that they form a waveguide in the woodpile photonic crystal. Here, we choose to place them directly on top of each other. If we then take a look at the woodpile photonic crystal from the top, we can "look through" the entire system. The waveguide is shown in fig. 4.15. Similar designs have been recently fabricated by the Noda group as shown in ref. [78] with a defect size equal to the center-to-center separation of the bars.

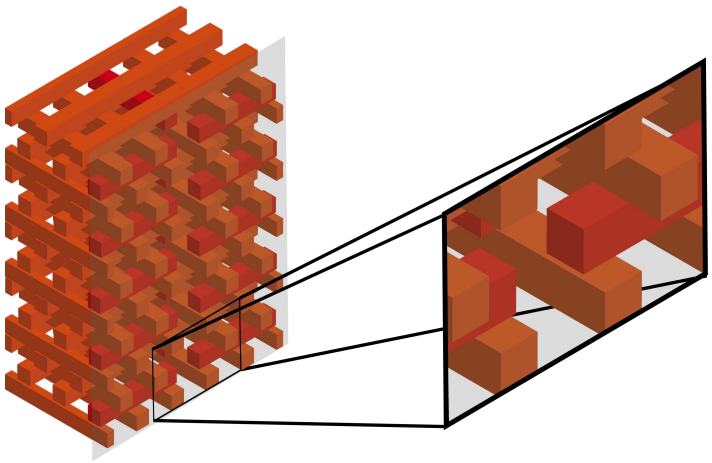

Figure 4.15.: Cut through a 5×5 supercell of a woodpile photonic crystal with a waveguide constructed by vertically aligned point defects.

In contrast to the point defect, the light with a wavelength inside the band gap can propagate along the waveguide through the crystal. Light can couple under perpendic-

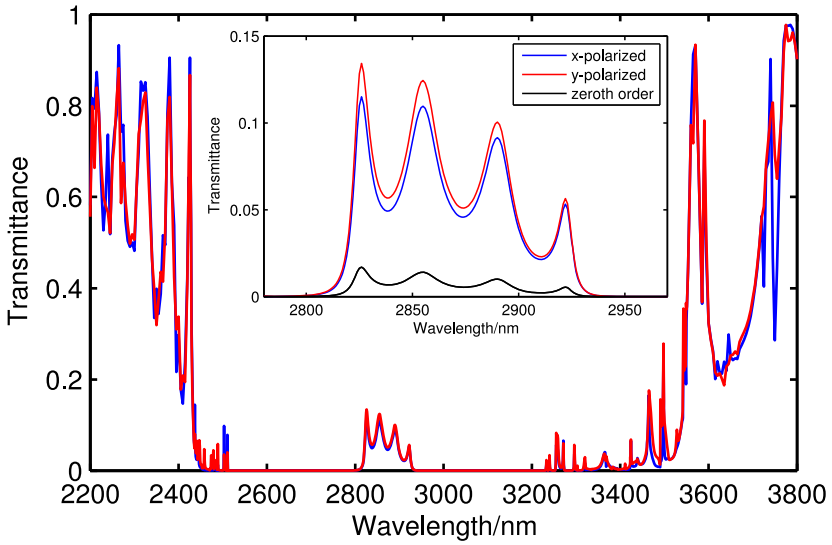

Figure 4.16.: Transmittance spectrum (similar to fig. 4.9) of the waveguide in a woodpile for perpendicular incidence calculated with 1185 Fourier coefficients.

ular incidence to the waveguide mode. Consequently, we obtain in the transmittance spectrum (shown in fig. 4.16) not a narrow but a broad peak between 2820nm and 2930nm. The oscillations within the transmittance peak are due to the dispersion of the waveguide. The number of oscillations depends on the length of the waveguide and increases with longer waveguides. These are Fabry-Pérot oscillations of the waves running back and forth in the waveguide.

4.2.4. Numerical Calculations of Experimentally Realized Woodpile Photonic Crystals

We have also compared our results to woodpile samples experimentally realized via direct laser writing. The results are presented in this section. The structure parameters are directly taken from the microscope pictures of the real woodpiles. In this woodpile structure the rods are not completely filled with silicon. There are air inclusions in the middle of the rods since in the double inversion process occur bottlenecks which are closed first and the silicon cannot reach all desired locations. Since the air holes are not identical in all rods, we do not directly consider these inclusions in the numerical calculations by adapting the structure but we use an averaged permittivity for the rods. The permittivity value is determined for each fabricated sample independently by adapting the edges of the stopband to the measured spectrum. The fabricated woodpiles are all located on a glass substrate. Thus, we use a glass half-space in the calculations with permittivity $\epsilon = 2.25$ as already mentioned in section 4.2.1.
First, we consider a defect-free woodpile which was fabricated such that the complete photonic band gap is centered around $\lambda = 1.55\mu$m [75]. Then, we consider a waveguide realized by direct laser writing [76]. The waveguide is designed in analogy to the one in section 4.2.3. In ref. [70] also calculated results for cavities in such woodpiles are shown. The experimental woodpile structures were realized and characterized by Isabelle Staude in the group of Prof. M. Wegener.

Woodpile with Band Gap at Telecom Wavelengths

The woodpile discussed is shown in fig. 4.17 (a). From the scanning electron micrographs, we extract the following geometric parameters: The woodpile has a lattice constant of $a \approx 566.3$nm and consists of rods with lateral diameter of $d \approx 206.7$nm. The height of the rods is $h \approx 1.46\, d \approx 301.8$nm. In the fabrication process of the polymer template, the structure shrinks in z-direction. Thus, the bar distance in z-direction does not correspond to the exact distance required for fcc-symmetry. As a consequence, this woodpile does not exhibit the fcc-geometry in contrast to the woodpile in section 4.2.1. In this case, the system's lattice constant in z-direction is $a_z \approx 1.15a$. The total height is 16 layers of rods. Due to the air inclusions in the rods as seen in fig. 4.17 (a), we obtain an averaged permittivity for the rods of $\epsilon = 9.9$ by fitting the stopband position to the experimentally measured stopband. The woodpile used for the numerical calculations is visualized in fig. 4.17 (b).
In the FMM calculations, the woodpile is constructed by three different scattering matrices as sketched in fig. 4.17 (b). These scattering matrices are necessary to properly

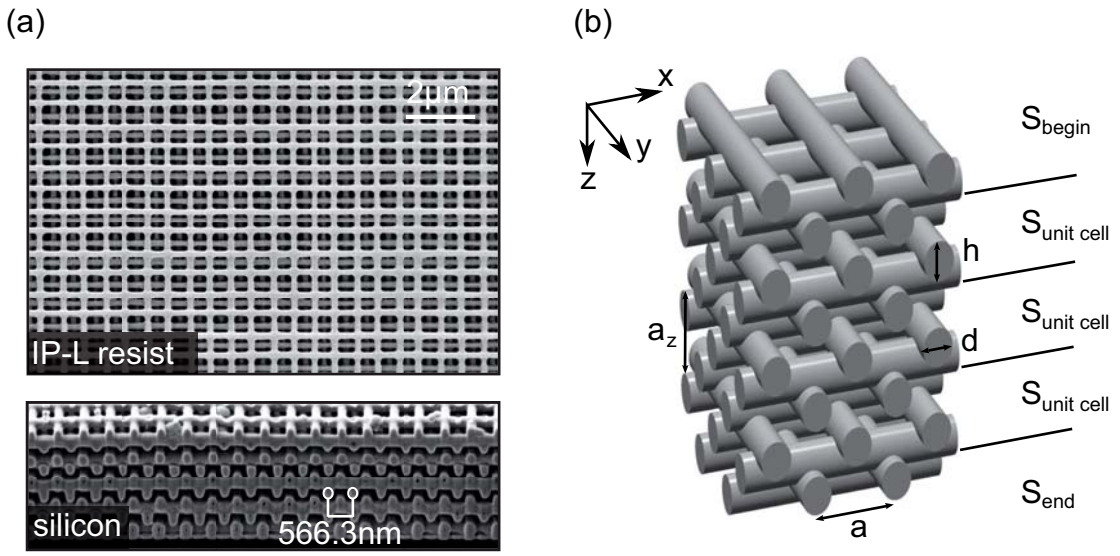

Figure 4.17.: (a) Experimentally realized structure before (top) and after (bottom) the double inversion [75]. (b) Schematic view of woodpile built with 16 elliptical rods. The three different scattering matrices S_{begin}, $S_{\text{unit cell}}$ and S_{end} are marked in the schematic.

model the top and bottom layer of the woodpile. The first scattering matrix describes the very first part of the rods in the crystal. The second one accounts for the middle part of the woodpile. It describes the repeating part of the woodpile system by three stacked unit cells. The third scattering matrix takes account of the remaining parts of the woodpile and the glass substrate.
We discretize the unit cell into 50 slices. Consequently, each slice has a thickness of 13.02nm. In the lateral plane, we perform a Fourier expansion with 197 plane waves. First, we calculate the spectrum of this woodpile for perpendicular incidence. We obtain a stopband between $\lambda = 1300$nm and 1700nm as shown in fig. 4.18.

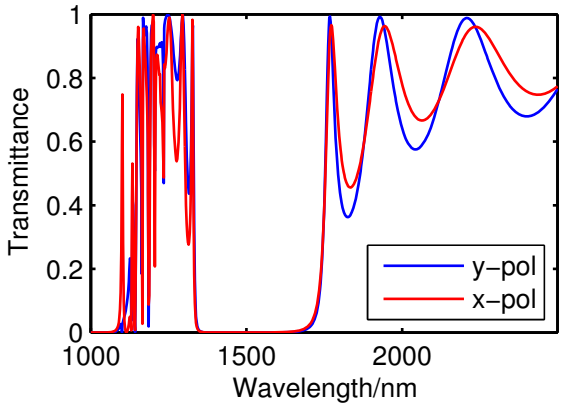

Figure 4.18.: Calculated transmittance spectrum of woodpile for perpendicular incidence in x- and y-polarized light.

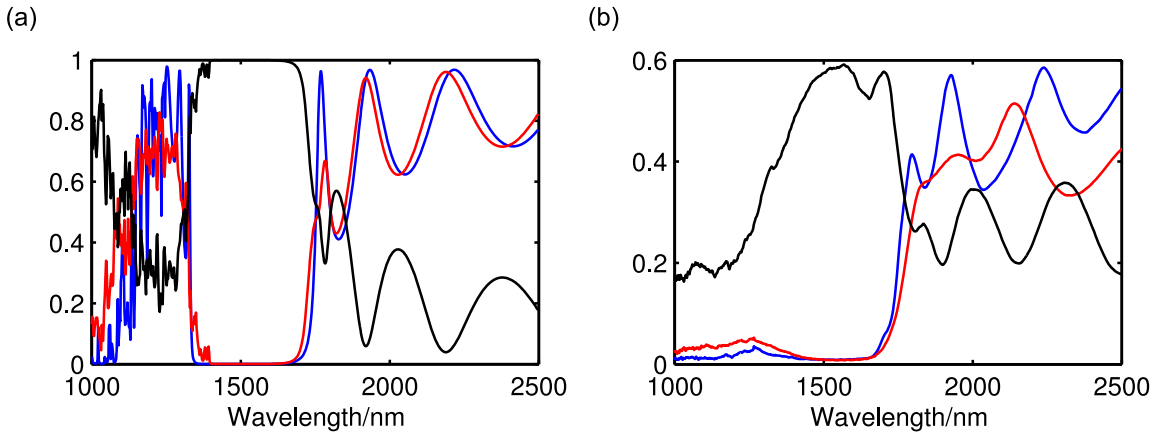

Figure 4.19.: (a) Calculated and (b) measured spectra of woodpile photonic crystal for different illuminations. The black curves are the averaged reflectance with $\theta = 15^o - 30^o$, the red curves show the averaged transmittance with $\theta = 15^o - 30^o$, and the blue ones are the averaged transmittance with $\theta = 0^o - 7.5^o$.

However, the spectrum of the fabricated woodpile is measured by a Cassegrain objective [24]. Due to the opening angle of the objective, the incident light has an angular spread in the azimuth angle θ of 15^o. The spectra obtained are averaged over the opening angle, $15^o \leq \theta \leq 30^o$ with respect to the surface normal and all incoming polarizations. Additionally the woodpile sample is tilted in the measurement with the Cassegrain objective, such that illumination between $\theta = 0^o$ and 7.5^o is achieved and the angular spread is reduced. In order to compare the calculated spectra with the measured ones we perform an averaging procedure: We calculate the spectra for $\theta = 0^o$ to 7.5^o and for $\theta = 15^o$ to 30^o in steps of 2.5^o. Additionally, we perform these calculations for $\phi = 0^o$ and 90^o as well as for s- and p-polarized incidence. Finally, we average over the obtained spectra.
We find that the stopband is centered around $\lambda = 1500$nm. From bandstructure calculations, we know that the complete photonic band gap it located between 1550nm and 1650nm. Thus, the dimensions of this woodpile have been scaled down with respect to ref. [72], such that the telecommunication wavelength 1.55μm is included in the band gap at the air-band edge, which is the short wavelength boundary of the band gap.

Waveguide

The woodpile which hosts the waveguide has bcc-symmetry [76]. Thus, the lattice constant in z-direction is exactly identical to the in-plane lattice constant $a_z = a \approx 782$nm. The rods have a width of $d \approx 219$nm and a height $h \approx 1.3d \approx 284.6$nm. The fabricated woodpile consists of 22 stacked layers of rods located on a glass substrate. As averaged permittivity for the rods with the air inclusions we obtain this time $\epsilon = 11$ such that the measured stopband fits to the calculated stopband. The complete band gap for this woodpile is found between $\lambda = 1.7\mu$m and 2μm.

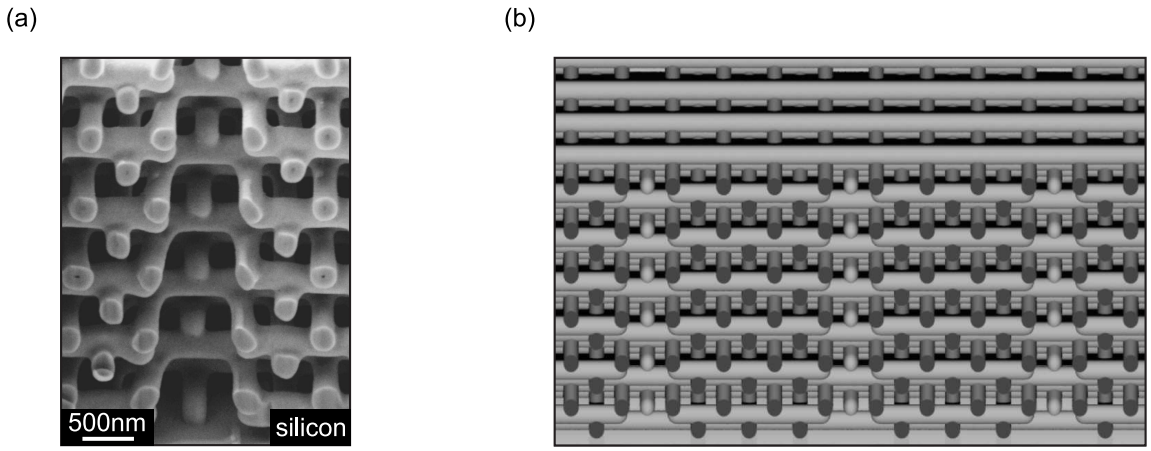

Figure 4.20.: (a) Experimentally realized waveguide structure in arranged in a 4×4 array [76]. (b) Schematic view of waveguide in the elliptical woodpile.

The waveguide which is hosted by this woodpile is similar to the one calculated in section 4.2.3. Due to the fabrication technique by direct laser writing the ends of the bars are not flat but can be assumed to be of ellipsoidal shape. The waveguide has a lateral width of $L \approx 0.72a \approx 563$nm. Thus, the center-to-center position of the first and last ellipsoids is exactly one lattice constant a. The waveguide is fabricated in a supercell with $N_{\mathrm{sc}} = 4$ (as shown in fig. 4.6). Figure 4.20 illustrates a schematic view of the waveguide in this woodpile with the correct dimensions.
The spectrum of the fabricated woodpile is again measured using the Cassegrain ob-

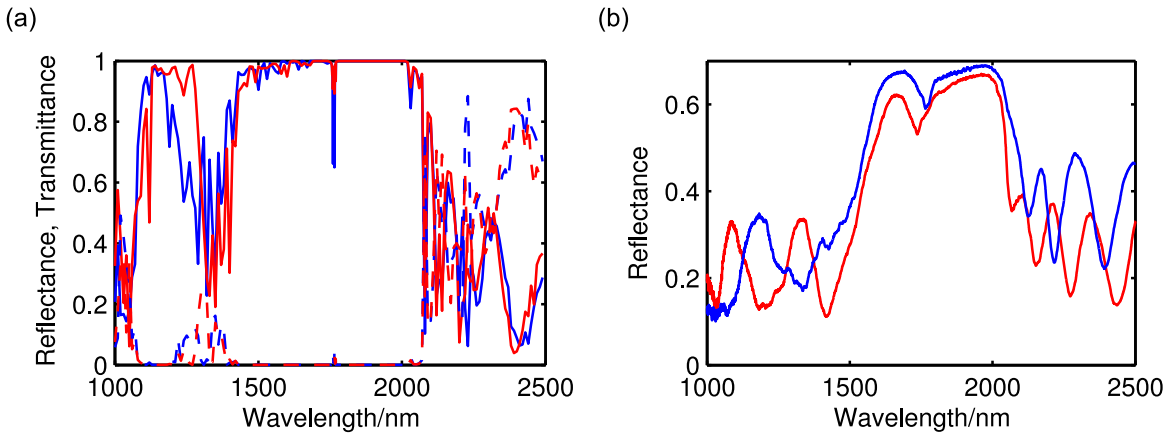

Figure 4.21.: (a) Calculated and (b) measured spectra of the waveguide in a woodpile photonic crystal. The red curve shows the spectrum for x-polarized incident light and the blue curve for y-polarized incident light. Additionally, we show the calculated transmittance spectra in forward direction as dashed lines. The calculated spectra are obtained for perpendicular incidence. In contrast, the measured spectra are averaged over $15^o \leq \theta \leq 30^o$ due to the experimental set-up.

jective [24]. Thus, the measured spectra are again averaged over the incident angle, $15^o \leq \theta \leq 30^o$. By adding a polarizer in the path of the reflected light spectra for light polarized parallel and perpendicular to the most upper rod layer are measured, too. In the numerical calculations, performed with 1185 Fourier coefficients, we obtain the spectrum for perpendicular incidence. We observe an increased transmittance in the complete band gap between $\lambda = 1755$nm and 1770nm reaching a maximum of 5.3% in forward direction. Thus, the waveguide is located in the complete band gap of this woodpile close to the air-band edge. The measured reflectance and the calculated reflectance and transmittance are shown in fig. 4.21.
We find that in the calculated spectrum the reflectance peak caused by the waveguide is roughly located at the same wavelengths for both polarizations. However, in the experiment we measure a small splitting between the two polarizations, centered at the wavelength obtained from the numerical calculation. The effect can be explained by sample imperfections of the cavity width in x- and y-direction causing a symmetry breaking between the two incident polarizations [78]. Additionally, the single cavities in each waveguide differ in size and shape causing a broadening with respect to the calculated reflectance.
By comparing the results of the woodpile with the elliptical rods to the quadratic rod case in section 4.2.3, we can see that, as expected, both systems behave similar which is to be expected due to the shared symmetry of the systems.

4.3. Opal Photonic Crystals

Opal photonic crystals [23, 81, 82] consist of spheres which are arranged in close-packed form. There are two possibilities of periodic stacking: one is the ABABAB

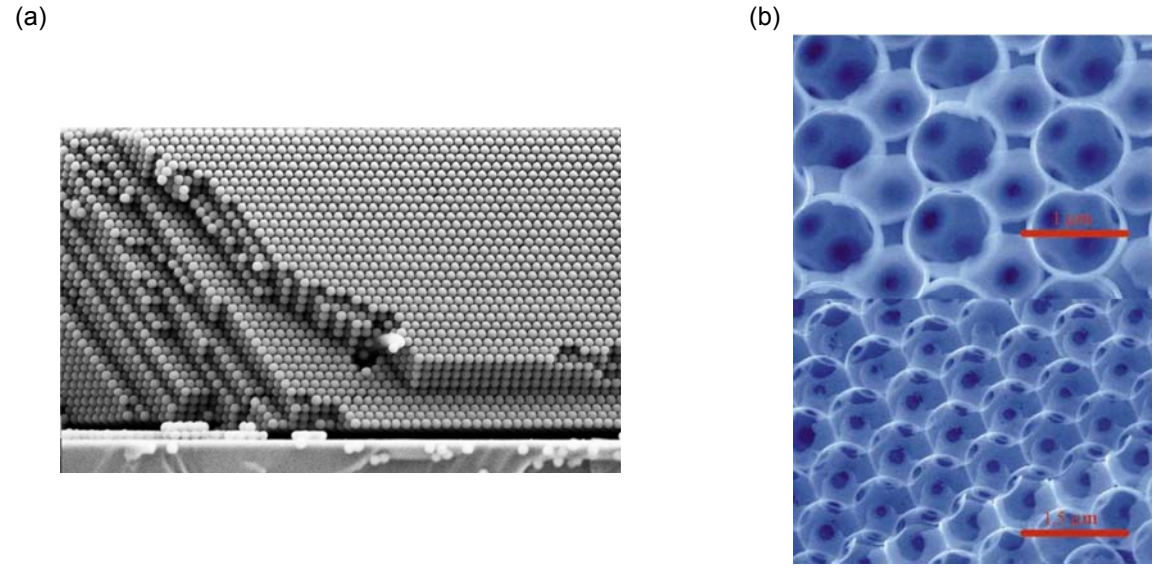

Figure 4.22.: (a) Opal photonic crystal consisting of PMMA spheres [79] and (b) inverted opal consisting of silicon [80].

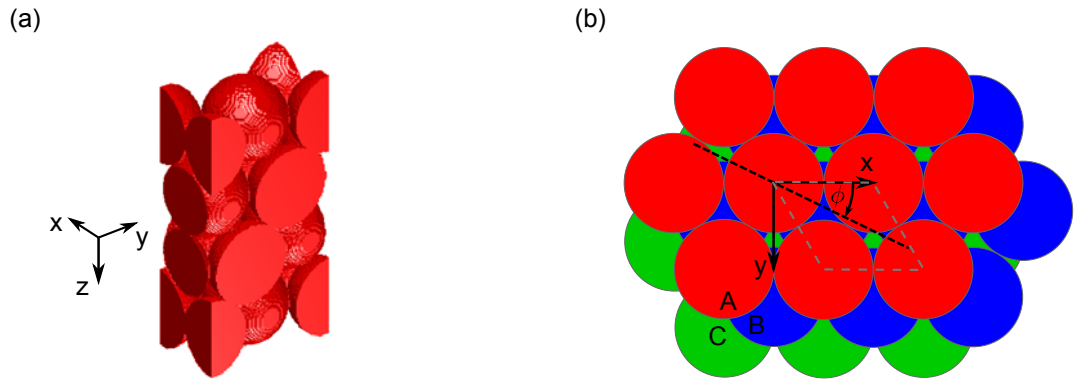

Figure 4.23.: Schematic figures of the opal photonic crystal. (a) 3D-view of opal with four stacking layers ABCA. (b) Top view on opal to illustrate the incident angle ϕ. The gray dashed line indicates the hexagonal unit cell used in the FMM calculations.

stacking corresponding to an hexagonal closed packed (hcp) and the other one is the face centered cubic (fcc) arrangement with ABCABC stacking. The filling factor for both arrangements is identical, namely $\approx 74\%$ [31]. Even random stacking is possible. Opals can be fabricated by colloidal suspension of commercially available silica or poly-methyl methacrylate (PMMA) microspheres [83] (see fig. 4.22). The spheres automatically arrange in close-packed form. The result is usually a mixture of hcp and fcc arrangements. These photonic crystals do not exhibit a complete photonic band gap, they have only stopbands in special propagation directions.
However, these structures can be employed as templates for silicon infiltration. Thus, by inversion of the opal structure with high index material (e.g. silicon with $\epsilon = 11.9$), inverse opal photonic crystals with a complete photonic band gap can be generated [15, 80] (see fig. 4.22).
Here, we numerically investigate opal photonic crystals made of PMMA spheres in a perfect fcc arrangement and compare their optical properties to fabricated (self-organized) opal photonic crystals [79]. The fabrication and experimental characterization has been performed by S. Romanov at the University of Erlangen-Nuremberg in the group of Prof. U. Peschel.
Figure 4.23 illustrates an opal photonic crystal with fcc arrangement. The top view on the opal photonic crystal shall also clarify the definition of the polar angle ϕ for the incident plane wave as defined in section 3.2.2.
The PMMA spheres have a refractive index $n_{\mathrm{PMMA}} = 1.489$ and a radius of $r \approx 184\mathrm{nm}$. Due to the close-packing, the radius is half of the lattice constant $a = 2r \approx 368\mathrm{nm}$. The spheres are surrounded by air, $n_{\mathrm{air}} = 1$. We investigate opal films which consist of 25 layers of spheres deposited on a glass substrate, $n_{\mathrm{glass}} = 1.5$. The distance between two neighboring layers of spheres is given by the close-packing as $d = \sqrt{2/3}a \approx 300.47\mathrm{nm}$.

4.3.1. Numerical Calculations of Opal Photonic Crystals

In the numerical calculations via the FMM, we use a hexagonal unit cell in the xy-plane with lattice vectors $\mathbf{a}_1 = (a, 0)$ and $\mathbf{a}_2 = (a/2, \sqrt{3}/2a)$. Thus, the lattice angle, as introduced in eq. (3.1), is $\zeta = 30^o$. The unit cell in the xy-plane is shown in fig. 4.23. As a single cell contains three layers of spheres it has a height of $a_z = 3d \approx 901.4$nm. In order to divide the unit cell into smaller subsystems, we use a total number of 60 equidistant slices where each single slice has a thickness of 15nm. The spectra shown are calculated with 97 Fourier coefficients in order to describe the lateral expansion in the FMM. To calculate the spectral properties, we illuminate the photonic crystal with a linearly polarized plane wave. The polarization can be either s-polarized or p-polarized (see section 2.6) and due to the anisotropy of the opal photonic crystal both

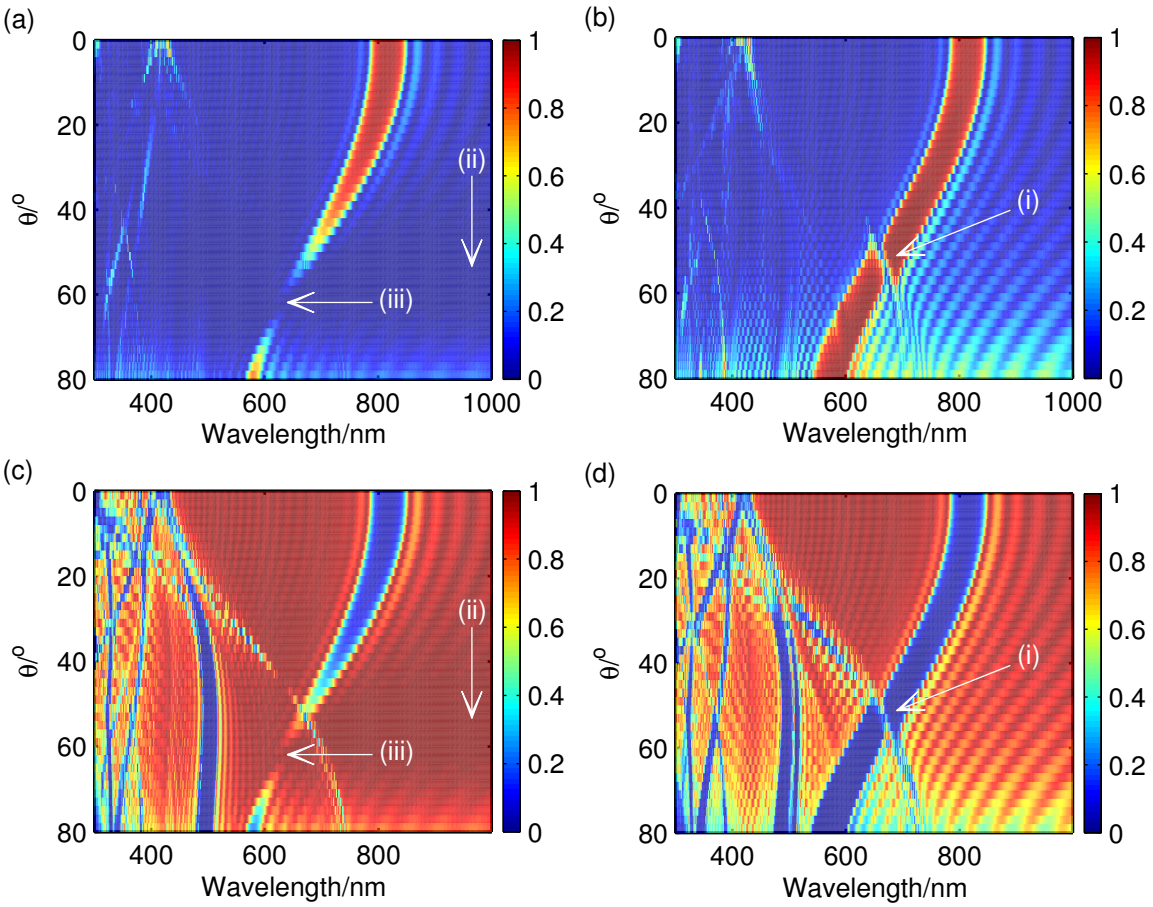

Figure 4.24.: Reflectance (a,b) and transmittance (c,d) spectra for an incident plane wave with $\phi = 30^o$ on the fcc-opal photonic crystal. The spectra (a,c) show the case for p-polarized incidence in p-polarized reflected and transmitted light, respectively, and the spectra (b,d) show the same for s-polarized incidence in s-polarized reflected and transmitted light. The white arrows indicate the avoided crossing (i), the Brewster angle (ii) and the critical angle of diffraction (iii).

polarizations behave completely differently. We observe the reflected p-polarized light into the zeroth diffraction order for a p-polarized incident plane wave. Analogously, we consider s-polarized incident light which is reflected in s-polarized light. In fig. 4.24, the spectra for those two polarizations are shown for different incident azimuth angles θ. We observe three different effects in these polarization spectra: (i) the avoided crossing of two bands, the so-called (111)- and ($\bar{1}$11)-band as defined below, in s-polarization, (ii) the Brewster angle in p-polarization, and (iii) the critical angle of diffraction also in the spectrum for p-polarized incidence. These three effects are discussed in the following.

Due to the close-packed form of the opal photonic crystal, the spheres arrange themselves in planes by self-assembling with different orientations in the opal photonic crystal. These planes can be labeled with the help of crystallography by Miller indices [31] as (hkl)-planes. The reflected light at these planes can form stopbands in the photonic crystals, the (hkl)-bands. In the case of the opal we can approximate the position of the bands by a simple Bragg diffraction model [84]. In general, light with vacuum wavelength $\lambda_{(hkl)}$ is diffracted at the (hkl)-plane in the crystal with refractive index n_{eff}. Thus, we obtain a stopband at

$$\lambda_{(hkl)}\left(\theta_{(hkl)}\right) = 2d_{(hkl)}n_{\text{eff}}\sqrt{\frac{3}{h^2+k^2+l^2}}\cos\theta_{(hkl)}, \tag{4.3}$$

with the interlayer distance $d_{(hkl)}$. $\theta_{(hkl)}$ is the angle of incidence with respect to the (hkl)-plane measured inside the crystal. For the effective refractive index of the opal we obtain $n_{\text{eff}} = \sqrt{0.74n_{\text{PMMA}}^2 + 0.26{n_{\text{air}}}^2} = 1.379$. In this case, the planes with the dominant diffraction are the (111)- and ($\bar{1}$11)-plane with interplane distances of $d_{(111)} = d_{(\bar{1}11)} = \sqrt{2/3}a$. The (111)-plane is illustrated by the colored layers A, B and C in fig. 4.23. The ($\bar{1}$11)-plane is tilted by an angle $\alpha = 70.53^o$ with respect to the (111)-plane. Since the angle of incidence is measured from outside the opal system, the internal angle onto the crystal plane has to be translated to the incident angle onto the opal surface. By Snell's law (2.43), we can relate, approximately, the angle inside

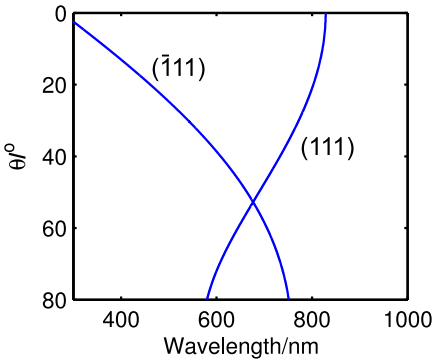

Figure 4.25.: Approximation of the (111) and ($\bar{1}$11) resonance in the fcc-opal photonic crystal by the Bragg diffraction model. The incidence with $\phi = 30^o$ and azimuth angle θ is measured in the air half-space.

the crystal θ_{inside} to the angle of incidence θ measured from outside the crystal, where the refractive index is denoted by n_{out}, as

$$\theta_{\text{inside}} = \arcsin\left(\frac{n_{\text{out}} \sin\theta}{n_{\text{eff}}}\right). \tag{4.4}$$

Since the crystal planes can also include an angle α with respect to the surface of the opal, we obtain for reflectance at the (111)-plane $\theta_{(111)} = \theta_{\text{inside}}$ and in the case of the $(\bar{1}11)$-plane $\theta_{(\bar{1}11)} = \alpha - \theta_{\text{inside}}$. The Bragg diffractions from these two planes are shown in fig. 4.25. Here, the angle θ is measured in the air half-space. The reflections from these planes form bands which can also be identified in the bandstructure of the system.
From this simple model, we expect that these two bands cross at the angle $\theta = 53^o$. Instead, the calculated spectra in fig. 4.24 for s-polarized incidence show an avoided crossing. In the spectra, we can clearly identify the (111)-resonance in the opal photonic crystal with the high reflectance and low transmittance band. Its position coincides with the Bragg model in fig. 4.25. As the model predicts, this band crosses with the $(\bar{1}11)$-band. In the spectrum for s-polarized incident light we observed the predicted crossing as avoided crossing. In this case, the eigenmodes of these bands, the Bloch modes, interact strongly. Consequently, the crossing presents as avoided crossing in the spectrum. The strong interaction can be attributed to the shared symmetry of the modes resulting in a repulsion of the bands at the crossing point.
For p-polarized incident light, the band caused by the reflectance at the (111)-plane is undisturbed at the position of the crossing. The reflectance band at the $(\bar{1}11)$-plane is hardly recognizable in the spectrum.
As second effect we can clearly identify the effect of the Brewster angle in the spectrum for p-polarized incident light in fig. 4.24 by the suppressed reflectance in the long wavelength limit for an incident angle θ between 50^o and 60^o. With the effective refractive index of the opal, the Brewster angle can be estimated by eq. (2.50) as $\theta_{\text{B}} = 54^o$. As expected, we cannot observe this effect in the spectrum for s-polarized incidence.
The third effect is the critical angle of diffraction. It is only observable in the p-polarized spectrum where the (111)-resonance vanishes at $\theta = 62^o$ and the line width of the resonance narrows around this point. In the s-polarized spectrum the (111)-resonance is not influenced at this point.
Together the three effects cause a strongly anisotropic behavior for s- and p-polarized incident light.

4.3.2. Comparison with Measured Spectra

We compare our calculations with the measured spectra of fabricated opal photonic crystals. The measured reflectance and transmittance spectra for s- and p-polarized light are presented in fig. 4.26. A visual comparison already shows the excellent agreement between measured and calculated data. In particular, we can clearly identify the (111)- and $(\bar{1}11)$-resonances. These resonances cross here at $\theta \approx 50^o$, where we observe the avoided crossing of the two resonances. In the reflectance spectrum for p-polarized incident light we identify the Brewster angle by the reduced reflectance

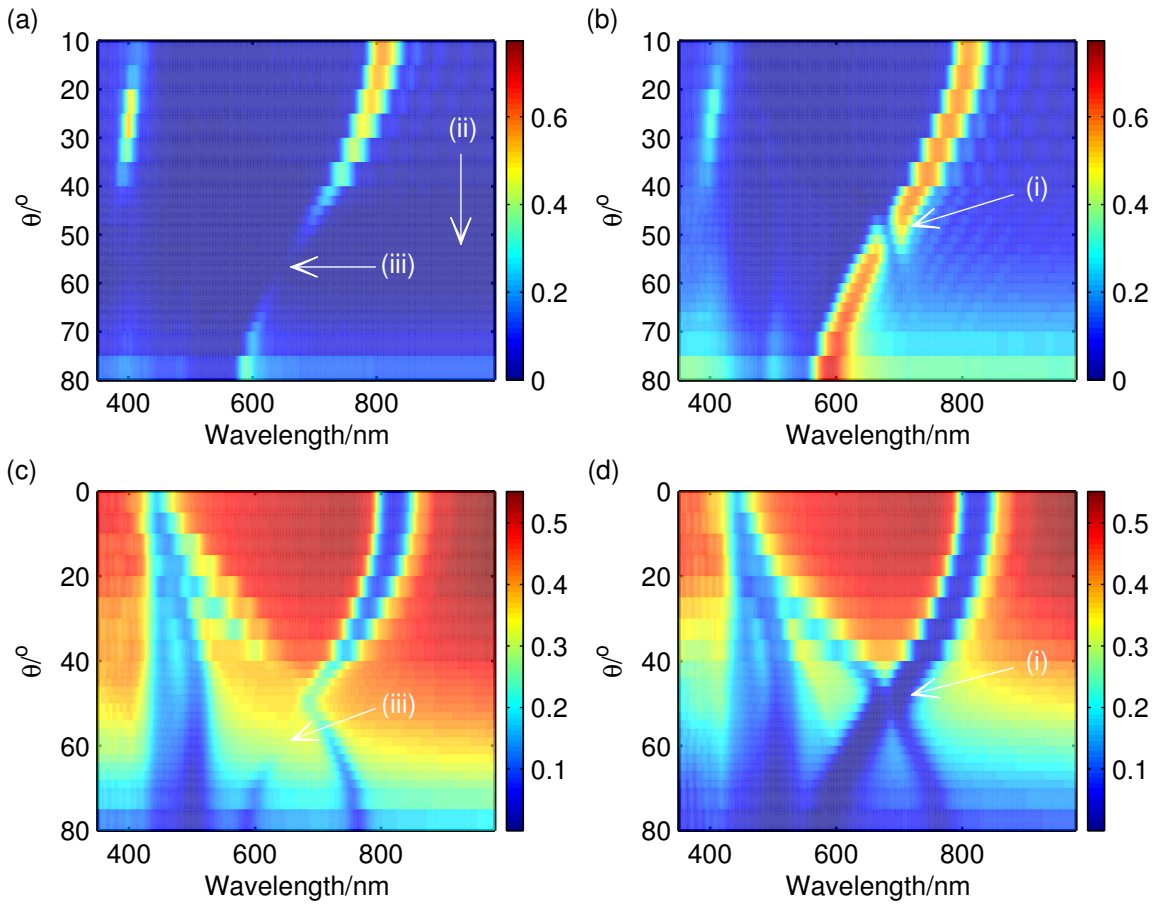

Figure 4.26.: Measured reflectance and transmittance spectra for an incident plane wave with $\phi = 30^o$ on the opal photonic crystal, arranged as in fig. 4.24.

around $\theta_B = 54^o$ as for the calculated fcc-opal. The critical angle of diffraction in the (111)-resonance also occurs in the reflectance spectrum. At $\theta = 56^o$ this resonance reaches its minimum. The small deviations between experiment and theory can be explained by fabricational imperfections.
The same effects as discussed in the calculated and measured spectra for $\phi = 30^o$ can also be observed by rotating the plane of incidence. But the incident angle θ for the observation of the avoided crossing changes, since the incidence on the internal opal-planes in the crystal is different. Especially at an incidence with $\phi = 0^o$ the band anticrossing is shifted closely towards the critical angle of diffraction.
To summarize section 4.3, we have shown that opal photonic crystals exhibit strongly anisotropic behavior. Furthermore, the numerical calculations of the fcc-opal photonic crystal are in excellent agreement with the experimental measurements on the opal films.

5. Adaptive Spatial Resolution

In this chapter, we report on our efforts in improving the convergence of the FMM by using adaptive spatial resolution. Our approach is to adapt the coordinate system to the structure under investigation. Additionally, the point density is increased at the material interfaces.
We start this chapter by summarizing earlier work on improving the convergence of the FMM. Then, we formulate the FMM in the transformed space. Since we already introduced the FMM in section 3.2 in general form, we are well prepared for the new formulation. The main focus of this chapter is the generation of the appropriate adaptive coordinates for arbitrary structures. Thus, we start the following section with an introduction to some analytically generated coordinates for grid-aligned rectangular structures such as circular structures. Then, we use a more general approach to generate the adaptive coordinates automatically. Similar to ref. [85], we set up a fictitious energy functional which is adapted to the desired structure. By a minimization procedure of this functional the coordinates are generated. Thereafter, we apply the automated coordinate generation to different test structures and perform convergence tests. Whenever possible, we compare the results with calculations by analytically generated transformations. Finally, we also show some field distributions calculated with the help of the adaptive coordinates.

5.1. Further Developments Regarding the Fourier Modal Method

The FMM, as introduced in section 3.2, is a fast and efficient method for investigating periodic systems with a moderate refractive index contrast such as dielectric photonic crystals. Examples of woodpile and opal photonic crystals have already been discussed in chapter 4. However, in the case of systems which contain metals (i.e. large refractive index contrast) the convergence of the FMM can become rather slow. Due to the large refractive index contrast in such systems, the number of required Fourier coefficients needs to be adapted in order to describe the permittivity in the slices adequately. However, by using more Fourier coefficients in the FMM the computations become very slow, memory consuming and inefficient. Additional problems arise since non-grid-aligned metallic structures are approximated by a zigzag-shaped contour in the plane which is Fourier transformed (see fig. A.2). To circumvent these problems, different approaches have been developed to further improve convergence. For instance, it has been suggested to calculate a vector field in the structure plane with vectors normal to the structure interfaces. By this normal vector field staircasing and the resulting zigzag contour of the structure can be avoided [86]. Therefore, the Fourier factorization rules

are applied more efficiently to the actual problem.
Another approach has been proposed by Granet [87]. He introduced new coordinates in the lateral plane which increase the spatial resolution at the material boundaries. Thereby, the Fourier representations of discontinuous permittivity profiles are improved. By incorporating these new coordinates into the FMM, the convergence of the method has been drastically improved. This concept is generally known as Adaptive Spatial Resolution (ASR). Until then, the ASR was only applied to two-dimensional systems. Furthermore, the same coordinate transformation was used for all slices. Subsequently, the method has been developed further in order to support different coordinate transformations in different slices [88]. In ref. [89] the extension to crossed gratings has been presented by employing two one-dimensional transformations. There, the authors have pointed out that the method could also be used for numerical calculations of three-dimensional systems. Unfortunately, the applied transformation is only applicable to gratings with rectangular structures. Another analytical transformation is discussed in ref. [90] for a two-dimensional grating with circular elements arranged in a quadratic grating.
In summary, it has already been shown that the FMM combined with ASR is a promising method for the numerical calculation of three-dimensional metallic systems. The primary problem is to find appropriate coordinates for an arbitrary structure.

5.2. Fourier Modal Method in Curvilinear Coordinates

First, we present the FMM in curvilinear coordinates. We use general coordinates as stated in eq. (2.52) together with Maxwell's equations in curvilinear coordinates which were introduced in eq. (2.61). In this formulation all changes to Maxwell's equations due to the coordinate transformation are absorbed in the material parameters (2.64) by the metric tensor g. Thus, we apply the FMM for anisotropic materials [30].
Since we only apply the coordinate transformation in the slicing plane, the general coordinate transformation can be expressed by

$$\bar{x}^1 = \bar{x}^1(x^1, x^2), \tag{5.1a}$$
$$\bar{x}^2 = \bar{x}^2(x^1, x^2), \tag{5.1b}$$
$$\bar{x}^3 = x^3. \tag{5.1c}$$

As a consequence, we obtain in the transformed system an anisotropic material with one principal axis pointing along the x^3-direction. The components of the anisotropic permittivity and permeability, following eq. (2.64), are stated here as

$$\begin{aligned}
\epsilon^{11} &= \bar{\epsilon}\sqrt{g}\left(\tfrac{\partial x^1}{\partial \bar{x}^1}\tfrac{\partial x^1}{\partial \bar{x}^1} + \tfrac{\partial x^2}{\partial \bar{x}^1}\tfrac{\partial x^2}{\partial \bar{x}^1}\right), & \mu^{11} &= \sqrt{g}\left(\tfrac{\partial x^1}{\partial \bar{x}^1}\tfrac{\partial x^1}{\partial \bar{x}^1} + \tfrac{\partial x^2}{\partial \bar{x}^1}\tfrac{\partial x^2}{\partial \bar{x}^1}\right),\\
\epsilon^{12} &= \bar{\epsilon}\sqrt{g}\left(\tfrac{\partial x^1}{\partial \bar{x}^1}\tfrac{\partial x^1}{\partial \bar{x}^2} + \bar{\epsilon}\tfrac{\partial x^2}{\partial \bar{x}^1}\tfrac{\partial x^2}{\partial \bar{x}^2}\right), & \mu^{12} &= \sqrt{g}\left(\tfrac{\partial x^1}{\partial \bar{x}^1}\tfrac{\partial x^1}{\partial \bar{x}^2} + \tfrac{\partial x^2}{\partial \bar{x}^1}\tfrac{\partial x^2}{\partial \bar{x}^2}\right),\\
\epsilon^{21} &= \bar{\epsilon}\sqrt{g}\left(\tfrac{\partial x^1}{\partial \bar{x}^2}\tfrac{\partial x^1}{\partial \bar{x}^1} + \bar{\epsilon}\tfrac{\partial x^2}{\partial \bar{x}^2}\tfrac{\partial x^2}{\partial \bar{x}^1}\right), & \mu^{21} &= \sqrt{g}\left(\tfrac{\partial x^1}{\partial \bar{x}^2}\tfrac{\partial x^1}{\partial \bar{x}^1} + \tfrac{\partial x^2}{\partial \bar{x}^2}\tfrac{\partial x^2}{\partial \bar{x}^1}\right),\\
\epsilon^{22} &= \bar{\epsilon}\sqrt{g}\left(\tfrac{\partial x^1}{\partial \bar{x}^2}\tfrac{\partial x^1}{\partial \bar{x}^2} + \bar{\epsilon}\tfrac{\partial x^2}{\partial \bar{x}^2}\tfrac{\partial x^2}{\partial \bar{x}^2}\right), & \mu^{22} &= \sqrt{g}\left(\tfrac{\partial x^1}{\partial \bar{x}^2}\tfrac{\partial x^1}{\partial \bar{x}^2} + \tfrac{\partial x^2}{\partial \bar{x}^2}\tfrac{\partial x^2}{\partial \bar{x}^2}\right),\\
\epsilon^{33} &= \bar{\epsilon}\sqrt{g} & \text{and} \quad \mu^{33} &= \sqrt{g}.
\end{aligned} \tag{5.2}$$

Thus, we have to solve Maxwell's equations with anisotropic material equations. In this case, the curl equations read

$$\begin{aligned} \partial_2 E_3 - \partial_3 E_2 &= \mathrm{i}\omega\mu^{11} H_1 + \mathrm{i}\omega\mu^{12} H_2, && (5.3a)\\ \partial_3 E_1 - \partial_1 E_3 &= \mathrm{i}\omega\mu^{21} H_1 + \mathrm{i}\omega\mu^{22} H_2, && (5.3b)\\ \partial_1 E_2 - \partial_2 E_1 &= \mathrm{i}\omega\mu^{33} H_3 && (5.3c) \end{aligned}$$

and

$$\begin{aligned} \partial_2 H_3 - \partial_3 H_2 &= -\mathrm{i}\omega\epsilon^{11} E_1 - \mathrm{i}\omega\epsilon^{12} E_2, && (5.4a)\\ \partial_3 H_1 - \partial_1 H_3 &= -\mathrm{i}\omega\epsilon^{21} E_1 - \mathrm{i}\omega\epsilon^{22} E_2, && (5.4b)\\ \partial_1 H_2 - \partial_2 H_1 &= -\mathrm{i}\omega\epsilon^{33} E_3. && (5.4c) \end{aligned}$$

In section 3.2 we already formulated the FMM for materials with these permeability and permittivity components. The correct Fourier factorization for this case is stated in appendix A.3. By transforming eqs. (5.3) and (5.4) into Fourier space, the equations obtained have the same form as eqs. (3.6) and (3.7). Thus, we can follow the calculation in section 3.2. In the end, we have to solve an eigenvalue problem of the same form as in eq. (3.15). Since we consider the case of one transformation in all slices, we do not need to change between the different coordinate systems. Thereby, we connect the eigensolutions of the individual slices by scattering matrices as described in section 3.2.5 and obtain the solutions of the fields in the transformed space.
Due to the transformed permittivity and permeability, even slices with homogeneous material distributions behave in the transformed space like structured regions. Therefore, the same eigenvalue equation (3.15) as in the structured slices has to be solved. Thus, also the incident plane wave (3.3) has to be presented via the numerical eigensolutions of the transformed space. Additionally, since we know the analytical solution of a homogeneous slice in the FMM by the Rayleigh expansion, we can directly transform these solutions into the curvilinear space. This means that on the one hand, we have to transform the plane wave basis of the Cartesian space into the plane wave basis of the transformed space. On the other hand, we have to transform the field components into the curvilinear system. The plane wave basis can be transformed via

$$L^o_{mn} = \int_0^1 \int_0^1 dx^1 dx^2 \, \mathrm{e}^{\mathrm{i}\alpha_{m_1}\bar{x}^1 - \mathrm{i}\alpha_{n_1}x^1 + \mathrm{i}\beta_{m_2}\bar{x}^2 - \mathrm{i}\beta_{n_2}x^2}, \qquad (5.5)$$

and the field components have to be transformed according to eq. (2.57). In order to properly determine the reflectance and transmittance into the different Bragg orders, we replace the numerically calculated eigenmodes in the incoming and outgoing region by the transformed Rayleigh solutions [91]. However, for the evanescent solutions we keep the numerical ones. The eigenmodes of the system can be degenerate. By using the analytical solutions we ensure that we can classify the different Bragg orders correctly as in the Chandezon method in section 3.3 [64].
We can also calculate the fields inside the structure and in both the outgoing and the incoming half-space of the system in two different ways. On the one hand, we can perform the Fourier back transformation in the curvilinear system and, on the other

hand, in the Cartesian system. Before we perform the Fourier back transformation, we transform the field components into the Cartesian system. This simplifies the calculation of the Poynting vector and the plotting of the field in the system. The applied transformation is the inverse transformation to the one stated in eq. (2.57). It reads in Fourier space

$$\bar{\mathbf{f}}_i^{\text{curvilinear}} = \left[\left[\frac{\partial x^k}{\partial \bar{x}^i}\right]\right] \mathbf{f}_k, \tag{5.6}$$

with the Toeplitz matrix representation of the derivative of the coordinate transformation. We gave the field vector $\bar{\mathbf{f}}$ the superscript $^{\text{curvilinear}}$ since the Fourier basis for this field vector is still given in the curvilinear space. The field vector $\mathbf{f}$ represents both the electric and the magnetic fields. Now, we have to transform the Fourier coefficients into the real space. If we back transform the Fourier coefficients as obtained by eq. (5.6) directly, we obtain the real space field components on the discretized curvilinear mesh $\bar{f}_i(x^1, x^2, x^3)$. Alternatively, we change the Fourier basis of the curvilinear space to the Fourier basis of the Cartesian space. Therefore, we have to multiply the Fourier vectors of the fields by the matrix L with the elements

$$\begin{aligned} L_{mn} &= \int_0^1 \int_0^1 d\bar{x}^1 d\bar{x}^2 \, \mathrm{e}^{-\mathrm{i}\alpha_{m_1}\bar{x}^1 + \mathrm{i}\alpha_{n_1}x^1 - \mathrm{i}\beta_{m_2}\bar{x}^2 + \mathrm{i}\beta_{n_2}x^2}, \\ &= \int_0^1 \int_0^1 dx^1 dx^2 \, |J(x^1, x^2)| \mathrm{e}^{-\mathrm{i}\alpha_{m_1}\bar{x}^1 + \mathrm{i}\alpha_{n_1}x^1 - \mathrm{i}\beta_{m_2}\bar{x}^2 + \mathrm{i}\beta_{n_2}x^2}, \end{aligned} \tag{5.7}$$

as in the Chandezon method by eq. (3.53). $|J|$ is the determinant of the Jacobian matrix (2.55) for the chosen coordinate transformation (5.1). The Fourier coefficients of the electric and magnetic field in the Cartesian space $\bar{\mathbf{f}}_i^{\text{Cartesian}}$ then read

$$\bar{\mathbf{f}}_i^{\text{Cartesian}} = L \left[\left[\frac{\partial x^k}{\partial \bar{x}^i}\right]\right] \mathbf{f}_k. \tag{5.8}$$

By the Fourier back transformation, we obtain the electric and magnetic fields on a Cartesian mesh $\bar{f}_i(\bar{x}^1, \bar{x}^2, \bar{x}^3)$.
For calculating the Poynting flux, we transform the field components into the Fourier space of the Cartesian space. Due to this transformation, we can, as in section 3.2.4, calculate the Poynting flux directly by the Poynting vector as the cross product of the electric and magnetic fields in eq. (2.34). However, we perform the field calculation in the structured region in the curvilinear space, since then we have an increased spatial resolution of the fields at the material boundaries as given by the adaptive coordinates. This means, we Fourier back transform the components $\bar{\mathbf{f}}_i^{\text{curvilinear}}$ in eq. (5.6) to the real space. In order to plot the obtained field distribution we have to take into account that the received field points are discretized on the mesh given by the curvilinear coordinates.

5.3. Mesh Generation

In the preceding section we have formulated the FMM in curvilinear coordinates. In order to significantly improve the convergence, we have to find appropriate coordinates

which are adapted to the structure [92]. This is the essential point for improving the convergence of the method.

5.3.1. Analytical Adaptive Coordinates for Rectangles and Circles

First, we present coordinate transformations for structures, where analytical transformations can be easily found as for rectangular and circular structures.
We start with rectangular structures which lie in the unit cell aligned to the coordinate axes. Thus, we can decouple the two-dimensional transformation (2.52) in two one-dimensional ones [89]. The transformation then reads

$$\bar{x}^1 = \bar{x}^1(x^1), \tag{5.9a}$$
$$\bar{x}^2 = \bar{x}^2(x^2), \tag{5.9b}$$
$$\bar{x}^3 = x^3. \tag{5.9c}$$

We take the one-dimensional transformation directly from ref. [88]. Since we apply the same type of transformation for the two spatial in-plane components, we state the transformation for a general axis $\bar{x}$ of the system first. The transformation is defined in sections between the material boundaries. In the case of a square, we have two material boundaries located at the points $\bar{x}_1$ and $\bar{x}_2$ in the unit cell. We call these points transition points because they define the transitions between the different sections in the coordinate transformation. These transition points in real space are transformed to the points $x_1 = 0.25$ and $x_2 = 0.75$ in the space of the adaptive coordinates, respectively. The transformation function between the subsequent transition points x_{l-1} and x_l reads

$$\bar{x}(x) = a_1 + a_2 x + \frac{a_3}{2\pi} \sin\left(2\pi \frac{x - x_{l-1}}{x_l - x_{l-1}}\right) \tag{5.10}$$

with parameters a_1, a_2 and a_3 as

$$a_1 = \frac{x_l \bar{x}_{l-1} - x_{l-1} \bar{x}_l}{x_l - x_{l-1}}, \tag{5.11}$$
$$a_2 = \frac{\bar{x}_l - \bar{x}_{l-1}}{x_l - x_{l-1}}, \tag{5.12}$$
$$a_3 = G\,(x_l - x_{l-1}) - (\bar{x}_l - \bar{x}_{l-1})\,. \tag{5.13}$$

The parameter G determines the strength of the transformation since G is the slope of the transformation at the transition points. When it approaches zero, the spatial resolution increases at these points. Due to the different transition points in the Cartesian and the curvilinear space, the transformation improves the resolution of tiny regions in the structure.
In the case of the quadratic structure, we apply the same transformation for the x^1- and x^2-coordinates. The resulting mesh for a square with side length assumed as half the lattice constant, arranged in a square array, is shown in fig. 5.1 (a). We place the square in the lattice such that the transition points in Cartesian space are $\bar{x}_1 = 0.25$ and $\bar{x}_2 = 0.75$.

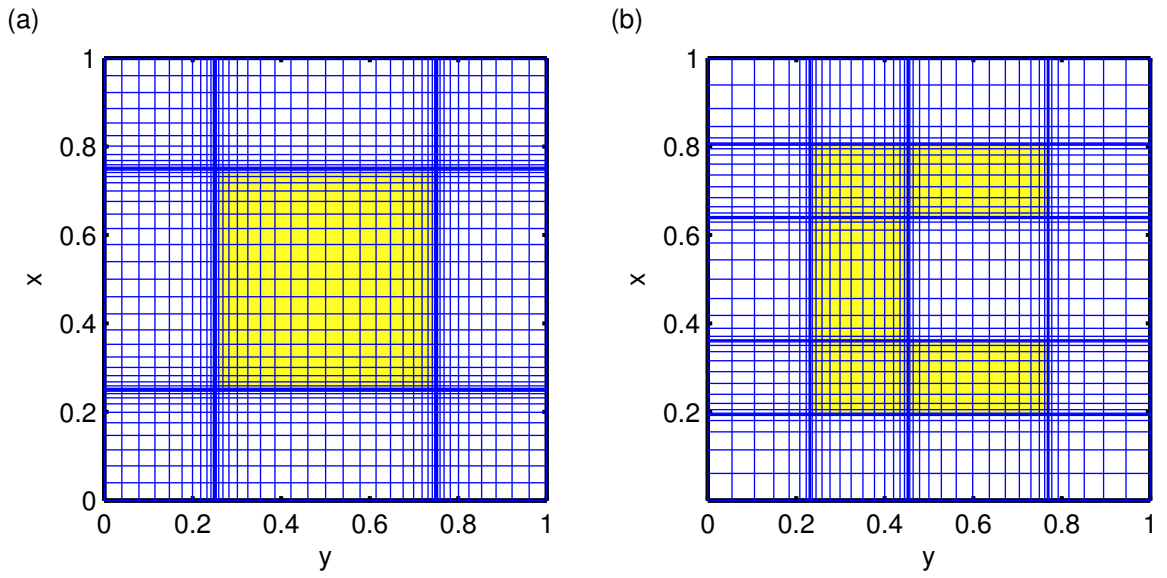

Figure 5.1.: (a) Mesh generated by two analytical transformations for a quadratic structure with side length $w = 1/2$ marked in yellow. The lattice constant a is set equal to one and the strength of the transformation is $G = 0.001$. (b) Analytical mesh for a split-ring resonator, marked in yellow. The strength of the transformation is again set to $G = 0.001$.

The transformation (5.10) can be easily applied to structures which are aligned to the lattice vectors of the periodic system, as for example split-ring resonators [93]. These have to be transformed with four transition points in the direction of the upper bar and three transition points along the two sidebars as shown in fig. 5.1 (b). We applied this transformation in ref. [94].
In order to obtain an analytical expression for adaptive coordinates of a circular structure, we make use of the fact that a circle can be transformed to a square [90]. The corresponding transformation for a circle with radius r arranged in a square array reads in normalized coordinates

$$\bar{x}^i(\tilde{x}^i,\tilde{x}^k) = \begin{cases} \frac{\tilde{x}^i}{\tilde{x}_1}\left(\frac{1}{2} - \sqrt{r^2 - \left(\tilde{x}^k - \frac{1}{2}\right)^2}\right), & \tilde{x}^i \le \tilde{x}_1,\ \ \tilde{x}_1 \le \tilde{x}^k \le \tilde{x}_2 \\ \frac{\tilde{x}^i - \tilde{x}_1}{\tilde{x}_2 - \tilde{x}_1}\left(\frac{1}{2} + \sqrt{r^2 - \left(\tilde{x}^k - \frac{1}{2}\right)^2}\right) & \\ \quad + \frac{\tilde{x}^i - \tilde{x}_2}{\tilde{x}_1 - \tilde{x}_2}\left(\frac{1}{2} - \sqrt{r^2 - \left(\tilde{x}^k - \frac{1}{2}\right)^2}\right), & \tilde{x}^i \le \tilde{x}_2,\ \ \tilde{x}_1 \le \tilde{x}^k \le \tilde{x}_2 \\ \frac{\tilde{x}^i - 1}{\tilde{x}_2 - 1}\left(\frac{1}{2} + \sqrt{r^2 - \left(\tilde{x}^k - \frac{1}{2}\right)^2}\right) + \frac{\tilde{x}^i - \tilde{x}_2}{1 - \tilde{x}_2}, & \tilde{x}^i \ge \tilde{x}_2,\ \ \tilde{x}_1 \le \tilde{x}^k \le \tilde{x}_2 \\ \tilde{x}^i, & \tilde{x}^k \ge \tilde{x}_1,\ \ \tilde{x}^k \ge \tilde{x}_2 \end{cases}, \tag{5.14}$$

with $i, k = 1, 2$. Thereby, the circle results in a square of side length $\sqrt{2}r$ in the $\tilde{x}^1\tilde{x}^2$-space. By this transformation the coordinate lines are aligned to the boundaries of the circle. The compression of the grid points at the interface can then be achieved by applying a transformation as in eq. (5.10) such that we obtain $\tilde{x}^1(x^1)$ and $\tilde{x}^2(x^2)$. The

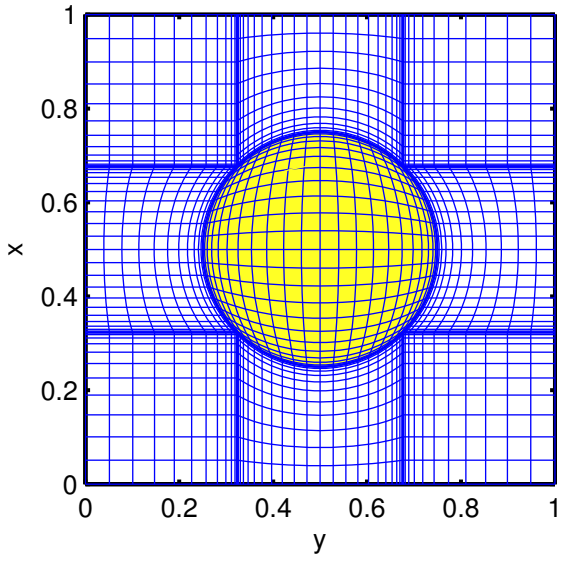

Figure 5.2.: Analytical mesh for a circular structure with radius $r = 1/4$ in the normalized unit cell. In the transformation, which is compressing the coordinates at the material boundary, G is set to 0.01.

transition points for this transformation can be chosen in the x^1x^2-space as $x_1 = 0.25$ and $x_2 = 0.75$ and in the $\tilde{x}^1\tilde{x}^2$-space the transition points are determined by eq. (5.14) as $\tilde{x}_1 = 0.5 - r/\sqrt{2}$ and $\tilde{x}_2 = 0.5 + r/\sqrt{2}$. Again, the strength of the transformation is given by the parameter G. In fig. 5.2, we show the analytically generated mesh for a circle with a diameter of half the lattice constant of the square array.

5.3.2. Minimization of a Fictitious Energy Functional

A coordinate transformation for an arbitrary dielectric distribution in the unit cell can be generated by minimizing a fictitious energy functional [85, 92, 95]. The free parameters in the functional determine the strength of the coordinate transformation. Due to the periodicity of the systems considered and of the FMM, the coordinate transformation needs to be periodic on the lattice. This can be easily obtained by defining the transformation in the truncated Fourier space as minimization

$$\bar{x}^1(x^1, x^2) = x^1 + \sum_m x_m^1 \mathrm{e}^{\mathrm{i}m_1 g_1 x^1 + \mathrm{i}m_2 g_2 x^2}, \tag{5.15a}$$

$$\bar{x}^2(x^1, x^2) = x^2 + \sum_m x_m^2 \mathrm{e}^{\mathrm{i}m_1 g_1 x^1 + \mathrm{i}m_2 g_2 x^2}, \tag{5.15b}$$

with the same notation for the summation over the reciprocal space as in section 2.8.2 and the reciprocal lattice vectors $g_1 = 2\pi/d_1$ and $g_2 = 2\pi/d_2$. Consequently, the free parameters are the complex Fourier coefficients x_m^1 and x_m^2. In the summation, we truncate the reciprocal space to M points by a circular truncation as already illustrated in fig. 3.3. Thus, there are $4M$ free parameters in the transformation function,

since we consider imaginary and real parts as independent parameters. However, the transformation has to be purely real. Hence, we only need half of the unknowns. With purely real coefficients the transformation can be written as

$$\begin{aligned}\bar{x}^1(x^1,x^2) &= x^1 + a^1_{\{0,0\}} + \sum_{m_+}\left[a^1_m \cos(m_1 g_1 x^1 + m_2 g_2 x^2)\right. \\ &\quad \left. - b^1_m \sin(m_1 g_1 x^1 + m_2 g_2 x^2)\right], \qquad (5.16a)\\ \bar{x}^2(x^1,x^2) &= x^2 + a^2_{\{0,0\}} + \sum_{m_+}\left[a^2_m \cos(m_1 g_1 x^1 + m_2 g_2 x^2)\right. \\ &\quad \left. - b^2_m \sin(m_1 g_1 x^1 + m_2 g_2 x^2)\right]. \qquad (5.16b)\end{aligned}$$

Here, we have reduced the summation to half of the Fourier space which is denoted by m_+. This is possible since the truncated Fourier space is symmetric. It is described by the point set $m_+ = \{m_1 > 0, m_2 \geq 0\} \cup \{m_1 \leq 0, m_2 > 0\}$. The remaining part of the space is given by the zero point $\{0,0\}$ and the point set $m_- = \mathbb{Z}^2 \setminus (\{0,0\} \cup m_+)$. The points belonging to m_+ are illustrated in fig. 5.3.

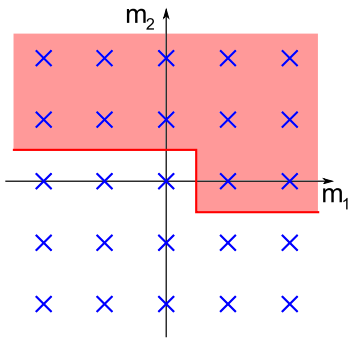

Figure 5.3.: The red-marked area denotes the set m_+.

Consequently, $M+1$ real coefficients a^1_m and a^2_m as well as $M-1$ coefficients b^1_m and b^2_m remain. Altogether, there are $2M$ free parameters. The coefficients of the real (5.16) and the complex transformations (5.15) are connected via

$$\begin{aligned} x^l_{\{0,0\}} &= a^l_{\{0,0\}}, \qquad (5.17a)\\ x^l_{m_+} &= \frac{1}{2}\left(a^l_{m_+} + \mathrm{i}b^l_{m_+}\right), \qquad (5.17b)\\ x^l_{m_-} &= \frac{1}{2}\left(a^l_{m_+} - \mathrm{i}b^l_{m_+}\right), \qquad (5.17c)\end{aligned}$$

with $l = 1, 2$.
We set the zeroth coefficients equal to zero, i.e. $a^1_{\{0,0\}} = a^2_{\{0,0\}} = 0$, since these merely cause constant shifts of the whole transformation. Thus, the number of free parameters is reduced to $2M-2$, which we use in the minimization.
Now, the energy functional has two different tasks. On the one hand, it shall increase the point density at the material interface and lead to coordinate lines which

are well aligned, on the other hand the grid points shall not accumulate too much. Consequently, our energy functional consists of four contributing terms

$$\mathcal{E}\left[\bar{x}^1(x^1,x^2),\bar{x}^2(x^1,x^2)\right] = \int dx^1 dx^2 \left[\mathcal{E}_\mathrm{c}(x^1,x^2) + \mathcal{E}_\mathrm{s}(x^1,x^2) + \mathcal{E}_\mathrm{g}(x^1,x^2) + \mathcal{E}_\mathrm{t}(x^1,x^2)\right], \tag{5.18}$$

which are integrated over the unit cell of the system.
$\mathcal{E}_\mathrm{c}$ is the compression energy and $\mathcal{E}_\mathrm{s}$ the shear energy [95]. These two energy terms act as restoring forces and pull back the coordinates to the Euclidean space. This means, an enhanced density in the coordinate points results in a necessary increase of the contributions by these two terms. Both energies depend on the covariant metric tensor (2.60b) by principal invariants as determinant and trace. The compression energy reads

$$\begin{aligned}\mathcal{E}_\mathrm{c}(x^1,x^2) &= \eta_\mathrm{c}\det\left(g^{pq}\right) \\ &= \eta_\mathrm{c}\frac{1}{\left(\partial_1\bar{x}^1\partial_2\bar{x}^2 - \partial_2\bar{x}^1\partial_1\bar{x}^2\right)^2}\end{aligned} \tag{5.19}$$

and the shear energy is given by

$$\begin{aligned}\mathcal{E}_\mathrm{s}(x^1,x^2) &= \eta_\mathrm{s}\mathrm{tr}\left(g^{pq}\right) \\ &= \eta_\mathrm{s}\frac{\left(\partial_1\bar{x}^1\right)^2 + \left(\partial_1\bar{x}^2\right)^2 + \left(\partial_2\bar{x}^1\right)^2 + \left(\partial_2\bar{x}^2\right)^2}{\left(\partial_1\bar{x}^1\partial_2\bar{x}^2 - \partial_2\bar{x}^1\partial_1\bar{x}^2\right)^2}\end{aligned} \tag{5.20}$$

with the parameters η_c and η_s, which we need to control the relative strength of the energy terms in the functional. In the later example calculations, we do not use the shear energy and set $\eta_\mathrm{s} = 0$ as in ref. [85]. We only state the term for reason of consistency.
The remaining two terms, the gradient energy $\mathcal{E}_\mathrm{g}$ and the tangential energy $\mathcal{E}_\mathrm{t}$, are responsible for adapting the coordinates to the special geometry of the actual system. They contain the geometry information of the system by the permittivity distribution $\epsilon(\bar{x}^1,\bar{x}^2)$ in the slice. The energy term $\mathcal{E}_\mathrm{g}$ should increase the point density near the material interfaces in the system. It is directly generated from the permittivity distribution of the structure. First, we prepare the permittivity by applying a Gaussian smoothing to the distribution. This means that we multiply the permittivity distribution in Fourier space with a Gaussian filter function. Thereby, the higher-order Fourier coefficients are reduced in magnitude and in real space the sharp boundaries of the distribution are blurred.
Since we are only interested in the positions of the material boundaries, we do not need to consider particular material properties in the coordinate generation. This has also the advantage, that we obtain the same adaptive coordinates if we only change the materials in the system. In the case of only two materials we are dealing with a binary grating. Here, the structural information is given by the function $S(\bar{x}^1,\bar{x}^2)$ which can either assume the values 0 and 1. Then, the smoothed structure function in real space is

$$S_\mathrm{sm}(\bar{x}^1,\bar{x}^2) = \sum_{l=\{l_1,l_2\}} \underbrace{S_l \mathrm{e}^{-\frac{(2\pi/d_1 l_1)^2+(2\pi/d_2 l_2)^2}{2w_\mathrm{g}^2}}}_{S_{\mathrm{sm},l}} \mathrm{e}^{\mathrm{i}l_1 g_1 \bar{x}^1 + \mathrm{i}l_2 g_2 \bar{x}^2}, \tag{5.21}$$

with the smoothing width w_s and the 'respective' Fourier coefficients $S_{sm,l}$. We sum over the reciprocal space, which is truncated to N_{sm} points, again by a circular truncation (see fig. 3.3).
Figure 5.4 (a) shows an example structure to illustrate the smoothing. We choose a circular structure located in the middle of a quadratic unit cell. By applying the smoothing as in eq. (5.21) with the width $w_s = 25$, we obtain a blurred image of the circle as shown in fig. 5.4 (b). The gradient of the smoothed structure function S_{sm} returns a vector field with vectors normal to the structure interface. Due to the applied smoothing of the structure function, the vectors of the gradient field have largest magnitude at the former material interfaces. For the case of the example structure, the corresponding gradient vector field is shown in fig. 5.4 (c) and the absolute values of

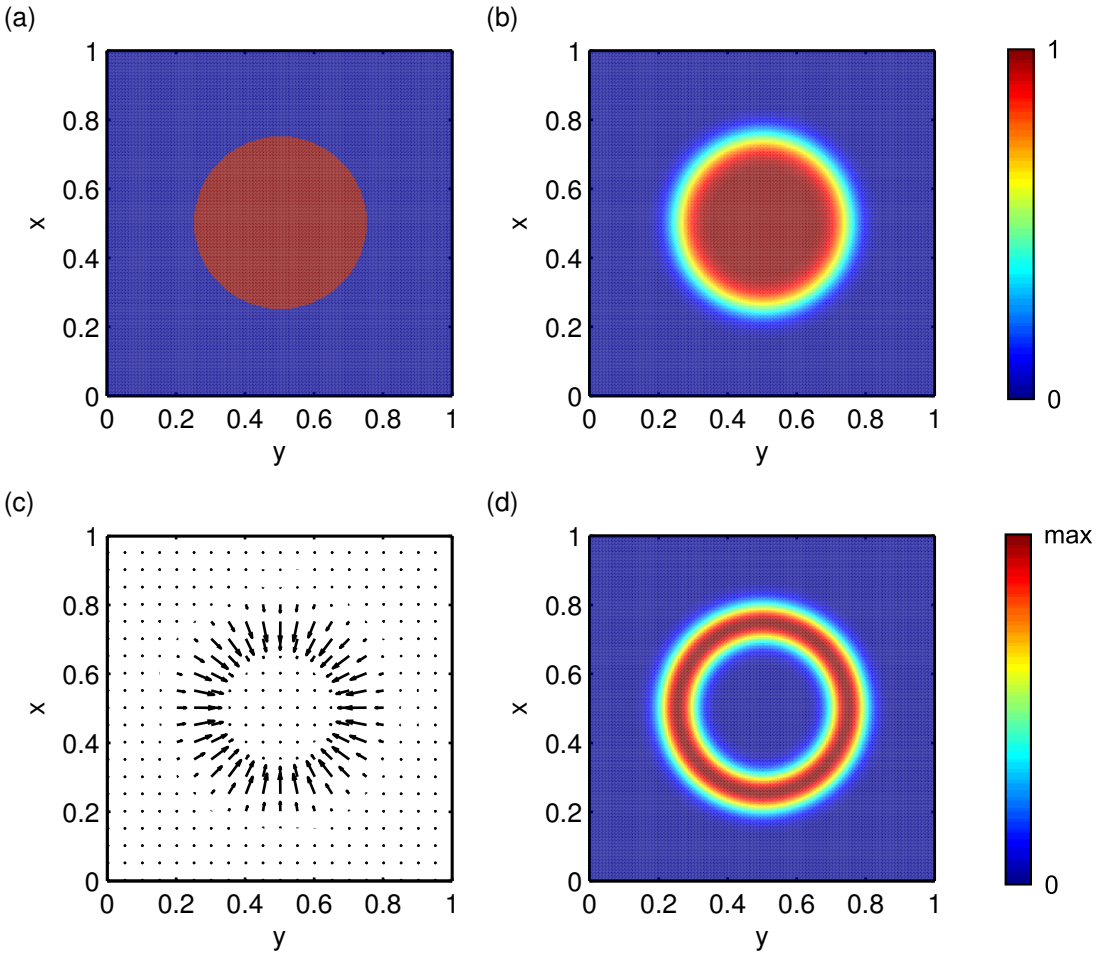

Figure 5.4.: Structural information of the ϵ distribution for a circle with radius $r = 0.25$ arranged in a quadratic array presented by (a) its structure function $S(x, y)$, (b) its smoothed structure function $S_{sm}(x, y)$ with smoothing width set to $w_s = 25$ and $N_{sm} = 240$, (c) the gradient vector field of $S_{sm}(x, y)$ (decreased vector density for better visibility) and (d) the magnitude of the vector field.

the gradients are presented in fig. 5.4 (d). As a consequence, we can use this gradient function as a potential distribution having its minima at the material interfaces by adding a minus sign in front of the gradient. The resulting term is called the gradient energy (or also negative energy [85]) and reads

$$\mathcal{E}_{\mathrm{g}}(x^1, x^2) = -\Big|\nabla S_{\mathrm{sm}}\left[\bar{x}^1(x^1, x^2), \bar{x}^2(x^1, x^2)\right]\Big|. \tag{5.22}$$

The gradient ∇ is calculated with respect to the Cartesian coordinates $\bar{x}^1$ and $\bar{x}^2$. This contribution to the fictitious energy functional does not carry a weighting factor, consequently the other energy terms are weighted relative to the gradient contribution in the functional (5.18).
The second structure dependent energy term $\mathcal{E}_{\mathrm{t}}$ shall orient the coordinate lines such that they are aligned along the structure interface. In order to generate such an energy term in the functional, we use a property of the gradient in eq. (5.22): It is perpendicular to the material interfaces in the vicinity of the material. Thus, we can include the scalar product of the gradient with the tangential vector along the coordinates lines into this energy term. The absolute value of the scalar product becomes minimal if the coordinate lines are parallel to the material interfaces [86, 96]. Therefore, it is a direct measure of the local parallelism of the coordinate lines relative to the material interface. The tangential vectors along the coordinate lines are given by the covariant basis vectors, $\mathbf{b}_1 = \partial_1\mathbf{r}$ and $\mathbf{b}_2 = \partial_2\mathbf{r}$, as defined in section 2.7.1. We call this contribution to the energy functional, the tangential energy. It reads

$$\begin{aligned}\mathcal{E}_{\mathrm{t}}(x^1, x^2) \;=\; & \eta_{\mathrm{t}}\Big(\left|\nabla S_{\mathrm{sm}}\left[\bar{x}^1(x^1, x^2), \bar{x}^2(x^1, x^2)\right]\cdot\mathbf{b}_1\right|^2 \\ & + \left|\nabla S_{\mathrm{sm}}\left[\bar{x}^1(x^1, x^2), \bar{x}^2(x^1, x^2)\right]\cdot\mathbf{b}_2\right|^2\Big)\end{aligned} \tag{5.23}$$

with the weighting parameter η_{t}.
In order to perform the minimization of the fictitious energy functional in eq. (5.18), we employ a conjugate gradient algorithm (Fletcher-Reeves) implemented in the gnu scientific library (gsl)[1]. For minimization this algorithm requires the energy functional and the gradient of the energy terms as a function of the coefficients of the coordinate transformation (5.16). The latter can be easily calculated by performing the derivatives of the energy terms with respect to the coefficients a_i and b_i.
The integral in the energy functional is solved by numerical integration. Thus, we sum over a sufficiently fine discretized equidistant grid in Cartesian $(\bar{x}^1, \bar{x}^2)$-space. This means, the number of grid points within the unit cell has to be chosen such that the structural features are adequately resolved. Additionally, we apply an oversampling in the Fourier transformation of the structure relative to the Fourier representation of the coordinate transformation. For the following results, we use a grid of 200×200 points. In these cases, we checked that a finer discretization does not change the numerical results.
Since the computation of the minimization can become very time consuming, we enforce the symmetry of the system on the coordinate transformation (5.16), whenever possible. This reduces the number of coefficients and therefore, the free parameters

[1] www.gnu.org/software/gsl/

in the minimization procedure are reduced, as well. Exploiting the symmetry property, we can also reduce the summation over the grid points to calculate the integral in the functional and the number of Fourier coefficients which describe the smoothed permittivity. Clearly, the calculation is enormously accelerated.
In the following section, we consider examples with mirror symmetry, $\mathcal{C}_\mathrm{s}$, and square symmetry, $\mathcal{C}_{4\mathrm{v}}$, according to the Schönflies notation. Additionally, the symmetry of the coordinates also ensures the expected symmetry in the field distributions.

5.4. Performance Investigations

In this section, we discuss three example systems to demonstrate the improvements in the convergence of the FMM due to the adaptive coordinates. As test systems we choose two set-ups for which we can also obtain a reference solution by an analytical coordinate transformation: (i) the transformation for squares and (ii) for circles, both arranged in a square array as discussed in section 5.3.1. Finally, we also investigate a square array of crescent-shaped optical antennas. Here, we do not have a reference solution by an analytical coordinate transformation for comparing the results.
The three different motifs – square disk, circular disk and crescent-shaped antenna – are arranged on a glass substrate with permittivity $\epsilon = 2.25$. As already discussed in chapter 4, the glass substrate is accounted for by a half-space. The remaining part of the system is filled with air, $\epsilon = 1$. The side length of the quadratic unit cell is in all three cases $d_1 = d_2 = 1000$nm. All test structures consist of a single layer with height $h = 50$nm. Thus, we consider systems with three slices. For the square disc, we discuss two different cases for the material of the motifs. First, we investigate the case of a dielectric object with permittivity $\epsilon = 12$. Second, we change the material to a metal which is described by a Drude model (see section 2.2.3) for gold with the parameters shown in fig. 2.4. In the case of the circular disk and the crescent-shaped antenna, we restrict the investigations to the transmittance spectra of a metallic motif. Additionally, we determine the electric field enhancement at the particle plasmon resonance for the crescent-shaped antenna with the ASR. All results are for normal incidence from the air side. Calculations for oblique incidence are also possible but do not provide any further insight into the performance of ASR within FMM.

5.4.1. Square Disk

The investigated square disks have a side length of $w = 500$nm. They are aligned to the Cartesian coordinate lines (see fig. 5.5). Thus, in the Fourier transformation the shape of the disk is not deformed by a zigzag contour as shown in fig. A.2. Consequently, the convergence of the system by the standard FMM should be rather good.
Before starting with the investigation of the convergence behavior, we have to generate a mesh for this system by minimizing the energy functional in eq. (5.18). In the case of the square disk we calculate the minimization with $M = 97$ points in reciprocal space. Due to the enforced $\mathcal{C}_{4v}$ symmetry in the minimization process, we deal with $(M-1)/4 = 24$ free parameters instead of the full $2M - 2 = 192$. In the terms of the

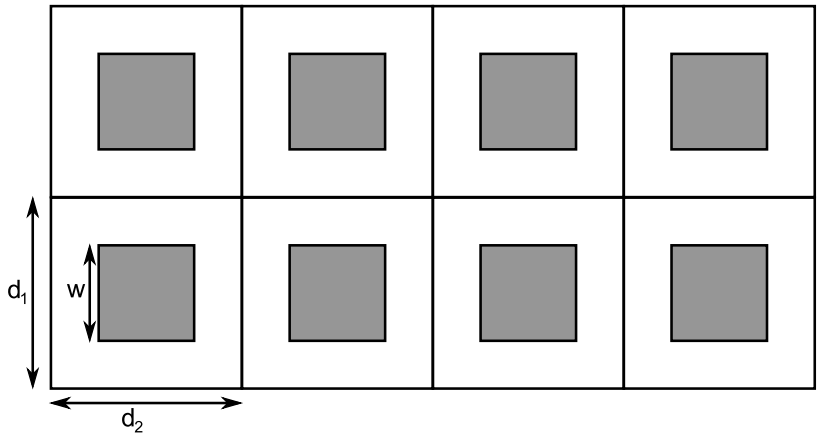

Figure 5.5.: Top view on square-disk structure (side length w) arranged in an array of quadratic unit cells with lattice constants d_1 and d_2.

energy functional we have to set different parameters: First, we choose the smoothing width in eq. (5.21) as $w_\mathrm{s} = 400$. Second, we set (also in eq. (5.21)) the number of Fourier coefficients of the truncated reciprocal space for the smoothing to $N_\mathrm{sm} = 9981$. Both determine the smoothed permittivity for the gradient energy as well as for the tangential energy term. As relative weights of the individual energy terms we choose the coefficients $\eta_\mathrm{c} = 0.1$, $\eta_\mathrm{s} = 0.0$ and $\eta_\mathrm{t} = 0.1$. This mesh is depicted in fig. 5.6 (a) and called later min (a). For comparison we also generate a mesh without the tangential energy term and set $\eta_\mathrm{t} = 0$. The other factors are kept the same. The resulting mesh is shown in fig. 5.6 (b) and denoted as min (b). At first sight, it seems to be very similar to the one with the tangential energy term.

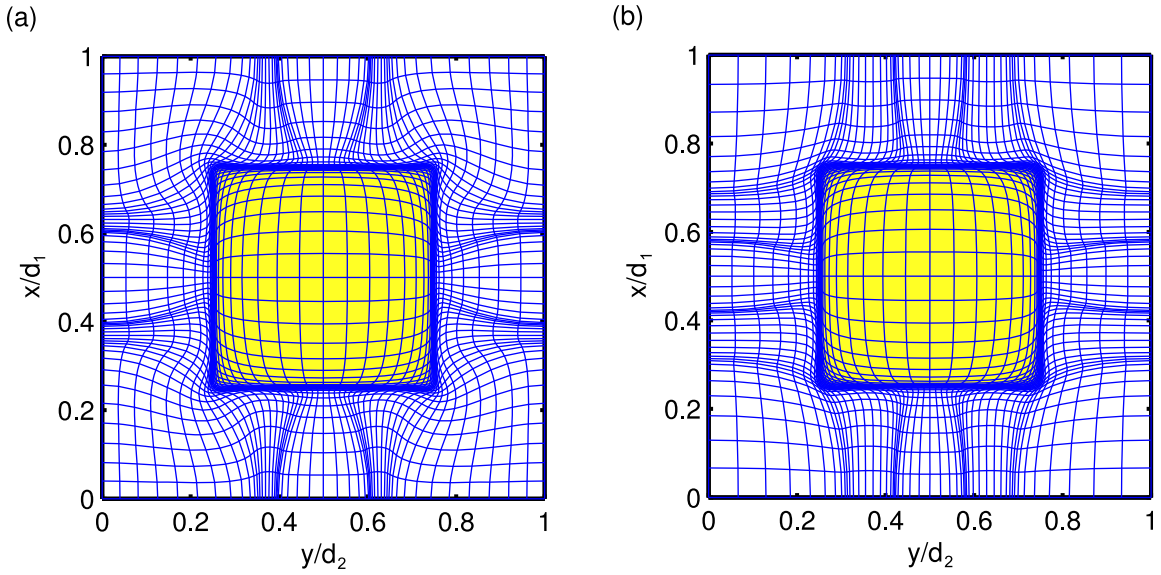

Figure 5.6.: Automatically generated mesh (a) with and (b) without tangential energy term. The parameters for the minimization are given in the text.

N	Li	analytical	min (a)	min (b)
81	11.10136637	11.13011854	10.94312509	10.92452339
149	11.12409750	11.14779821	11.11683144	11.11483733
253	11.13158052	11.14818684	11.14632990	11.14585998
377	11.13469796	11.14817728	11.14808488	11.14784958
529	11.13621747	11.14817722	11.14813399	11.14797708
709	11.13704113	11.14817476	11.14813736	11.14800343
901	11.13752691	11.14817457	11.14814216	11.14803617
1129	11.13783207	11.14817429	11.14814738	11.14805258

Table 5.1.: Convergence of first (rescaled) propagation constant q for a square array of square dielectric disks with $\epsilon = 12$ as a function of the number of plane waves N. The results for the largest purely real eigenvalue at $\lambda = 1600$nm are shown. The eigenvalues have been calculated with standard FMM (Li), with analytical ASR (analytical, fig. 5.1), and numerically determined ASR via (a) minimization with tangential energy term (min (a), fig. 5.6 (a)) and (b) without this term (min (b), fig. 5.6 (b)).

First, we check the convergence of the propagation constants q which are obtained by solving the eigenproblem (3.15) in the structured slice. For this purpose, we use the square motif consisting of dielectric material with $\epsilon = 12$. In table 5.1, the largest real-valued propagation constants, at $\lambda = 1600$nm, calculated with the standard FMM (see section 3.2) and results obtained by three different coordinate transformations are listed. As coordinates for the adaptive spatial resolution we have the analytical transformation shown in fig. 5.1 and the two transformations obtained by minimization of the functional in fig. 5.6.
We can observe that the analytical ASR and the numerical ASR with tangential term are identical up to the sixth significant digit. The numerical ASR without tangential term shows slightly worse convergence behavior by yielding only the first five digits identical to the other two transformations. Using the standard FMM, we only obtain the first three digits identical to the result from the analytical transformation. From this behavior, we conclude that the standard FMM is not converged for $N = 1129$ plane waves that we have considered in this example.
Since the FMM shows really slow convergence in the case of systems containing metals, we calculate the transmittance spectrum of the same structure but with the discussed square disks made from gold. The transmittance spectra into zeroth order obtained with standard FMM and the three different adaptive coordinates are presented in fig. 5.7. All spectra have been calculated with $N = 317$ plane waves and, at first sight, rather good agreement is obtained.
Additionally, we have investigated the convergence characteristics of this system near the particle plasmon resonance at $\lambda = 1600$nm. In fig. 5.8, the convergence for transmittance into the zeroth diffraction order over the number of plane waves N is shown. At first sight, the four different curves show similar behavior. As expected, best con-

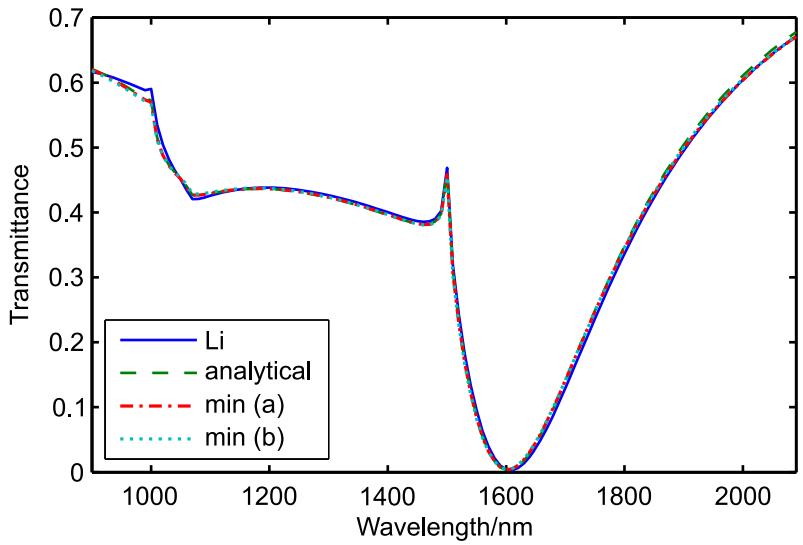

Figure 5.7.: Transmittance spectra into the zeroth diffraction order for square gold disks arranged in a square array calculated with standard FMM (Li) and three different adaptive coordinates which are the analytical ASR (analytical), numerically generated ASR with tangential term (min (a)) and without this term (min (b)). The four numerical calculations are performed with $N = 317$ plane waves.

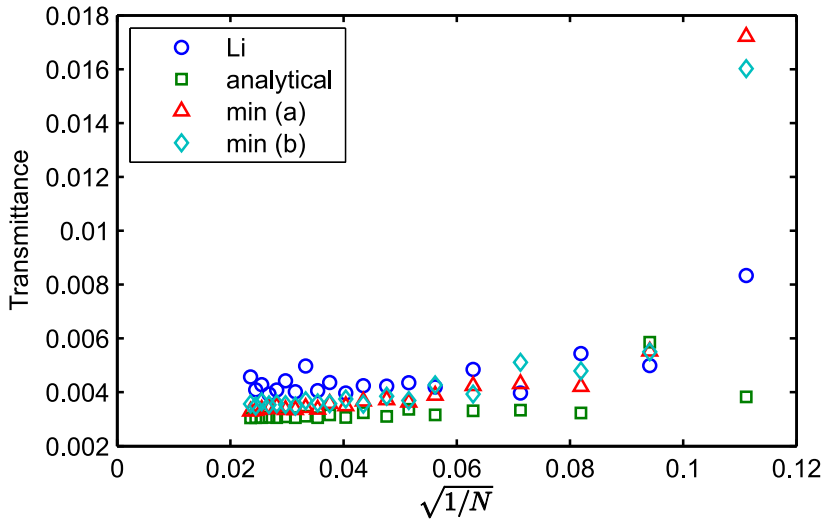

Figure 5.8.: Convergence characteristics of the transmittance into the zeroth diffraction order at $\lambda = 1600$nm for the square array of quadratic metallic disks. Again standard FMM (Li), the analytical ASR (analytical), the numerically generated ASR with tangential term (min (a)) and without this term (min (b)) are employed. At the considered wavelength, the permittivity of gold is assumed as $\epsilon = -122.03 + 12.85\mathrm{i}$.

vergence is reached with the analytical transformation. The convergence behavior obtained by the two automatically generated coordinates follows closely with a small advance of the transformation considering the tangential energy term. Even the standard FMM by Li performs well. This result shows that grid-aligned structures, as the square disk here, can be treated rather satisfactorily within standard FMM. However, the use of adaptive coordinates provides a welcome convergence acceleration. The importance of the adaptive coordinates should increase in the case of non-grid-aligned structures such as, for example, circular shapes as investigated in the next section.
In the following, for all example structures which we discuss, we apply the tangential energy term in the mesh generation by minimization.

5.4.2. Circular Disk

As second example, we consider a square array of circular disks. The disks under investigation have a radius of $r = 250\text{nm}$ and are placed in the center of a quadratic unit cell as shown in fig. 5.9(a). In order to generate the adaptive coordinates by minimization, we use – in contrast to the square disk – a smaller smoothing width of $w_\text{s} = 200$ since the coordinates do not have to map sharp corners in the case of the circular disk. Consequently, we also reduce the employed Fourier coefficients for the smoothing of the structure in eq. (5.21) and set $N_\text{sm} = 3993$. The parameters for the weights of the individual terms in the functional are kept the same as for the square disk, i.e. $\eta_\text{c} = 0.1$, $\eta_\text{s} = 0.0$ and $\eta_\text{t} = 0.1$. We again employ $M = 97$ Fourier coefficients to describe the coordinate transformation and enforce the $\mathcal{C}_{4\text{v}}$-symmetry of the structure. The resulting mesh is shown in fig. 5.9(b).
In fig. 5.10 we depict the transmittance spectra into zeroth diffraction order of the square array of circular metallic disks made of gold. The gold is again described by

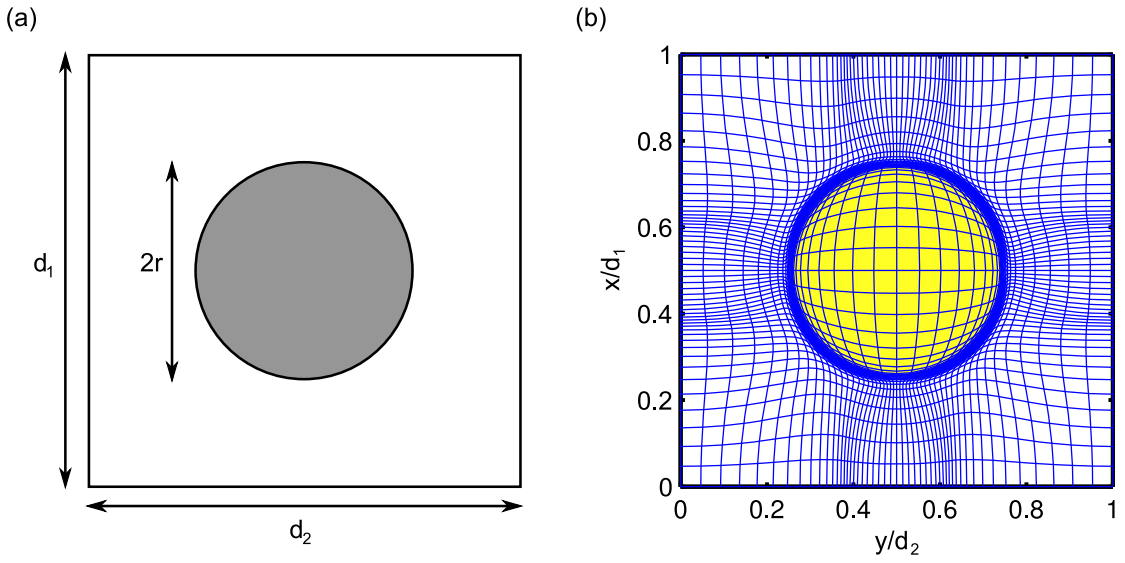

Figure 5.9.: (a) Schematic view of circular disk in the quadratic unit cell. (b) Automatically generated mesh with parameters given in the text.

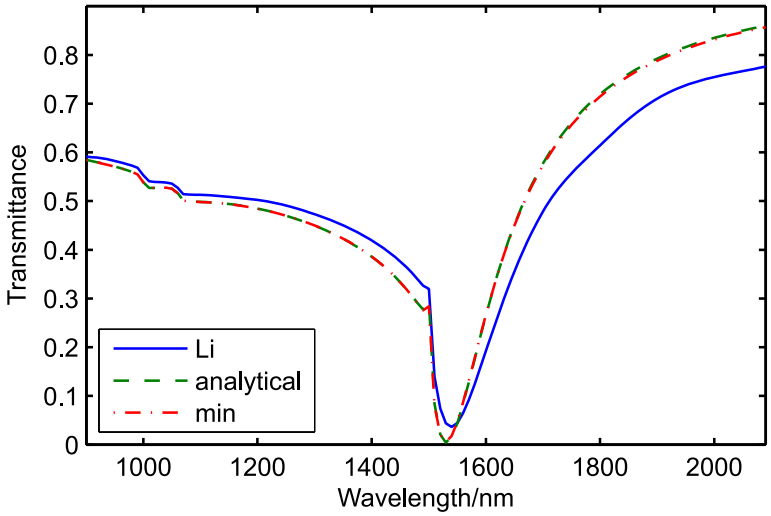

Figure 5.10.: Transmittance spectra into zeroth diffraction order for the square array of circular disks. The spectrum carried out within standard FMM (Li) is calculated with $N = 1257$ plane waves and the spectra with ASR (analytical and min) are calculated with $N = 317$ plane waves.

the Drude model. The three different spectra are obtained within standard FMM, analytical ASR and minimized ASR. In fig. 5.2, the analytical transformation is shown. We employ $N = 1257$ plane waves for the standard FMM since the structure is not grid-aligned. Therefore, the circular structure has to be treated by a zigzag contour in the Fourier transformation similar to fig. A.2. Due to this approximation the circular disk system is far from convergence. In contrast to this, the spectra of both ASR approaches agree well even if we only apply $N = 317$ plane waves.
In analogy to the square disks, we also investigate the convergence of the system with the circular disk at the particle plasmon resonance, $\lambda = 1530$nm. The convergence behavior of the transmittance into zeroth diffraction order is shown in fig. 5.11. It becomes clear that the analytical and numerical ASR converge to the same value. In contrast to this, the ordinary FMM shows a rather poor convergence behavior. Since the standard FMM value is far from the value obtained by the ASR, we further increase the number of plane waves in the standard FMM. For this purpose we applied the symmetry reduction technique as described in ref. [97]. Thus, we pushed the number of plane waves up to $N = 23\,993$, but even for this enormous number of Fourier coefficients we cannot state that the ordinary FMM yields converged results. The result slowly approaches the values obtained with the two ASR-based computations.
From these results, we conclude that the ASR is absolutely necessary for the investigation of non-grid-aligned metallic structures. In the subsequent section, we will, therefore, apply our numerical ASR technique to analyze a realistic system with geometric features at different length scales. Thus, we study an array of crescent-shaped metallic nano-particles which shall serve as an example of an arbitrarily shaped structure and shows the universality of the automatic coordinate generation by minimization.

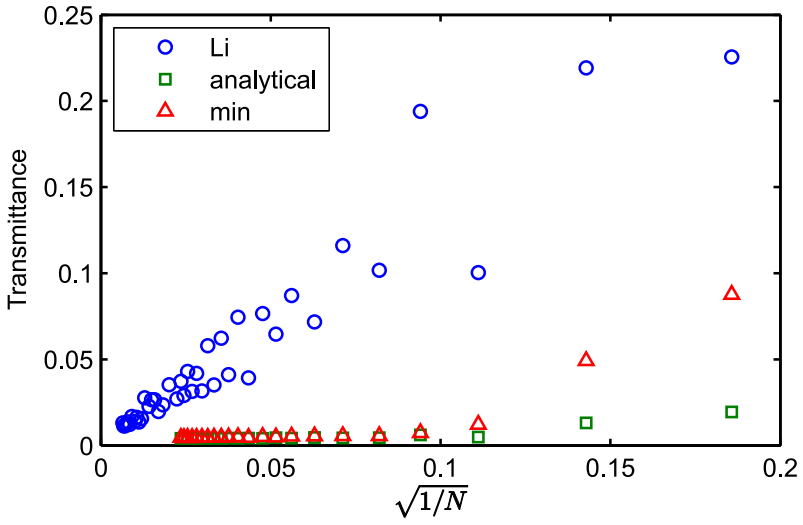

Figure 5.11.: Convergence characteristics of the transmittance into the zeroth diffraction order at $\lambda = 1530$nm for the square array of circular metallic disks. At this wavelength the permittivity of gold is assumed as $\epsilon = -110.9 + 11.24$i.

5.4.3. Crescent-shaped Optical Antenna

Finally, we apply the numerical ASR to crescent-shaped optical antennas arranged in a square array. Similar crescent-shaped antennas can be fabricated by colloidal templating [98]. Their optical properties can be compared to the ones of split-ring resonators [93]. Figure 5.12 (a) illustrates the crescent-shaped antennas with the dimensions we

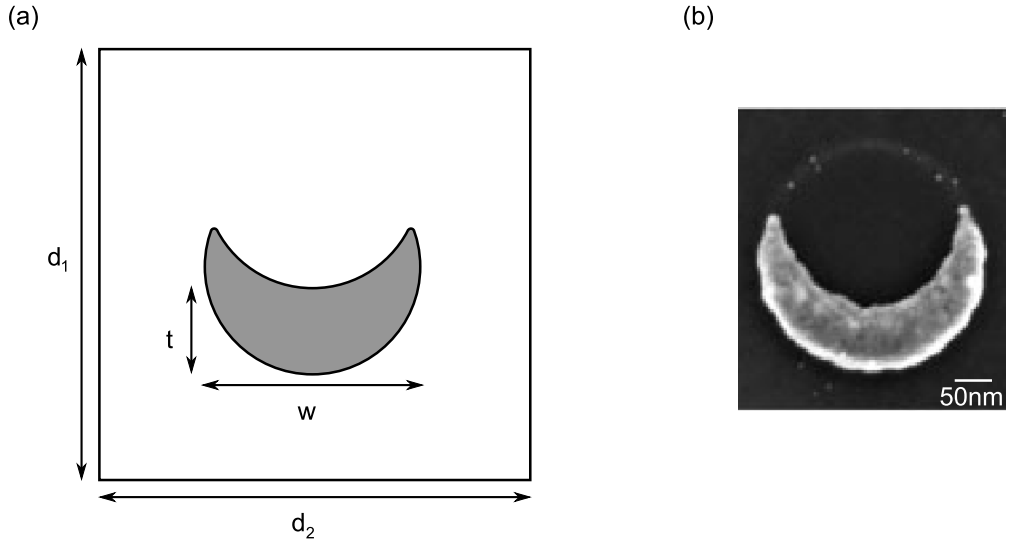

Figure 5.12.: (a) Sketch of crescent-shaped nano-particle and (b) experimentally realized crescent taken from ref. [98].

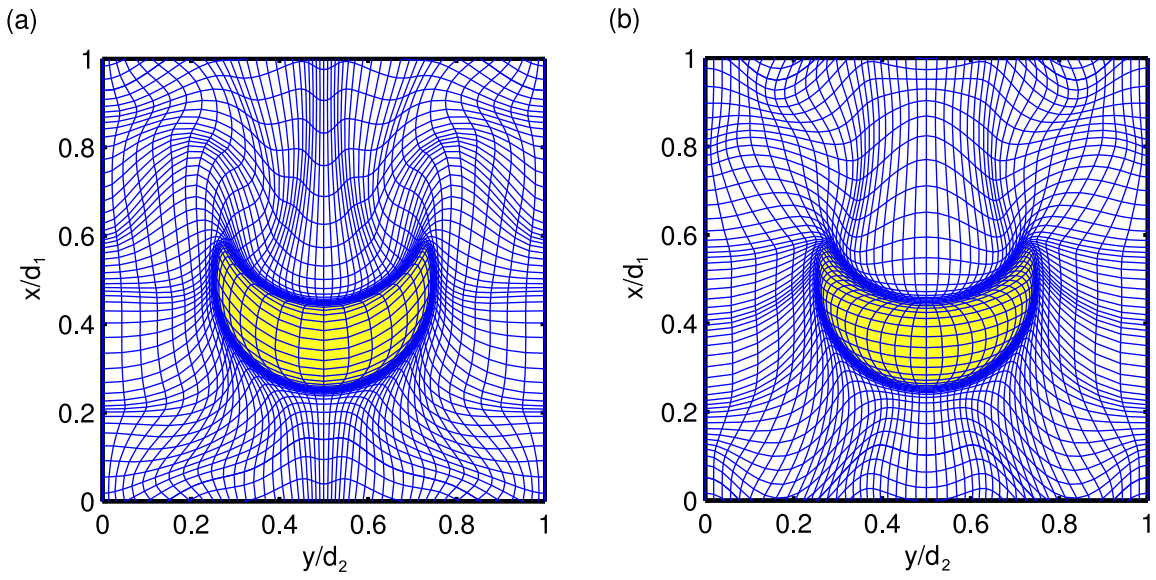

Figure 5.13.: Automatically generated mesh (a) with and (b) without tangential energy term. The parameters for the minimization are given in the text.

use in our numerical calculations. The specific values for the dimensions are the width $w = 500$nm and lateral thickness $t = 200$nm. Again, the structure is situated in the center of the quadratic unit cell. Since experimentally realized structures as shown in fig. 5.12 (b) do not possess sharp corners at the two tips we added roundings on the two corners, each with radius 10nm.
First, we generate the coordinate transformation for this special structure. Since the gradient energy term produces high concentrations of points at the small tips relative to the other boundaries of the crescent-shape, we have to increase the relative strength of the compression term (compare eq. (5.19)) to the energy functional. Additionally, we increase the weight of the tangential energy term (5.23) in order to adapt the coordinate lines to the local geometry and to align them to the small radius of the tip rounding. Consequently, we generate the ASR with $\eta_\mathrm{c} = 0.2$, $\eta_\mathrm{s} = 0.0$ and $\eta_\mathrm{t} = 0.2$. We set the smoothing width to $w_\mathrm{s} = 200$ as for the circular disk, since a too large value causes a very narrow range of the gradient energy. Thus, almost no coordinate points would be collected at the tip. Then, the other areas are more 'attractive' for the energy functional. We adapt the number of points in the truncated Fourier space for the smoothing to $N_\mathrm{sm} = 7989$, based on the size of the tips. Due to the mirror symmetry $\mathcal{C}_\mathrm{s}$ of the crescent-shape, we can reduce the reciprocal space to half of the points. For the minimization, we only have $M - 1$ free parameters. Here, we used $M = 97$. Thus, the number of free parameters in the minimization is equal to 96, which is sufficient to describe the transformation instead of the full $2M - 2 = 192$ parameters.
The resulting coordinate transformation by the minimization is shown in fig. 5.13 (a). For the crescent-shape we cannot obtain an analytical transformation as easily as for the rectangular and circular shapes in the previous examples. Thus, we generate a second transformation by the minimization without the tangential energy term which we use for comparing the results. We only change $\eta_\mathrm{t} = 0$ and take the other values as

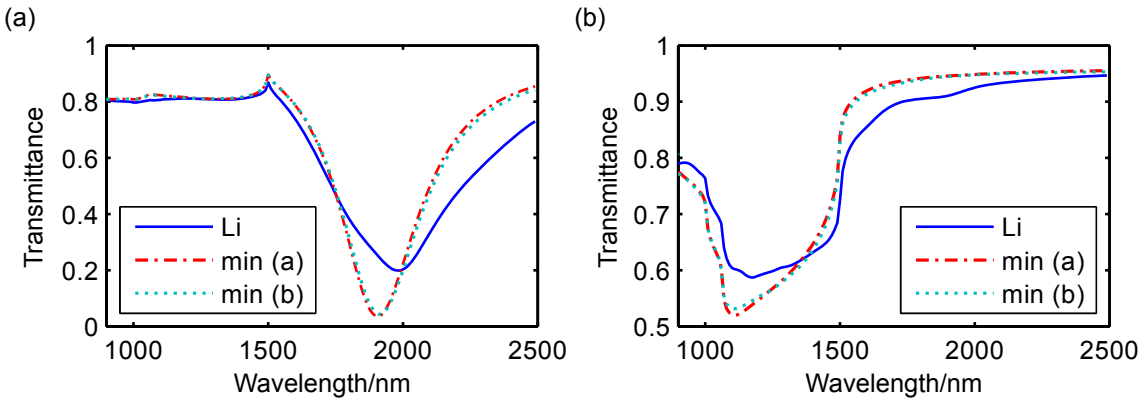

Figure 5.14.: Transmittance spectrum into zeroth diffraction order of the crescent-shaped antenna arranged in a square array for (a) y-polarized and (b) x-polarized incident light. The spectrum carried out within standard FMM (Li) is calculated with $N = 1257$ plane waves and the spectra with ASR (min (a) and min (b)) are calculated with $N = 317$ plane waves

before. The mesh obtained is illustrated in fig. 5.13 (b).
Next, we calculate the transmittance spectra for x- and y-polarized normally incident plane waves. The resulting transmittance spectra are depicted in fig. 5.14. They are obtained by the standard FMM and the two coordinate transformations. In the case of the standard FMM, the computation is not converged with the applied $N = 1257$ reciprocal lattice vectors. However, the computations with the two different numerical ASRs need only $N = 317$ Fourier coefficients to achieve well-converged spectra. As expected from the similarity of the crescent-shaped nano-antenna to the split-ring resonators, we obtain a so-called electric resonance at $\lambda = 1100$nm for incidence with x-polarized electric field. The resonance under y-polarized incidence at $\lambda = 1900$nm can be compared with the so-called magnetic resonance. Additionally, we observe Rayleigh anomalies at $\lambda = 1500$nm and $\lambda = 1000$nm in the spectra.
As before, we check the convergence of the transmittance into zeroth order near the resonances of the crescent-shape. In fig. 5.15 (a) the convergence behaviors for the three different FMM-computations at $\lambda = 1900$nm for y-polarized incident light are presented. Correspondingly, the convergence close to the electric resonance at $\lambda = 1100$nm is investigated in fig. 5.15 (b). As already expected from the spectra and similar to the result for the circular disk, the convergence behavior of the standard FMM is very poor. However, the transmittance values for the crescent-shapes, calculated with the two different numerical ASR, seem to converge to the same value at the two investigated positions. As in the case of the square disks in section 5.4.1, the transmittance value in the FMM obtained by the ASR including the tangential energy term converges faster than the one without the tangential energy term.
In the case of the crescent-shape, we also calculate the field distribution via the FMM with ASR. Thereby, we can exploit the increased resolution of the adapted mesh at the two tips of the crescent-shape by computing the electromagnetic field directly in the curvilinear coordinates. Hence, the high spatial resolution of the coordinates near

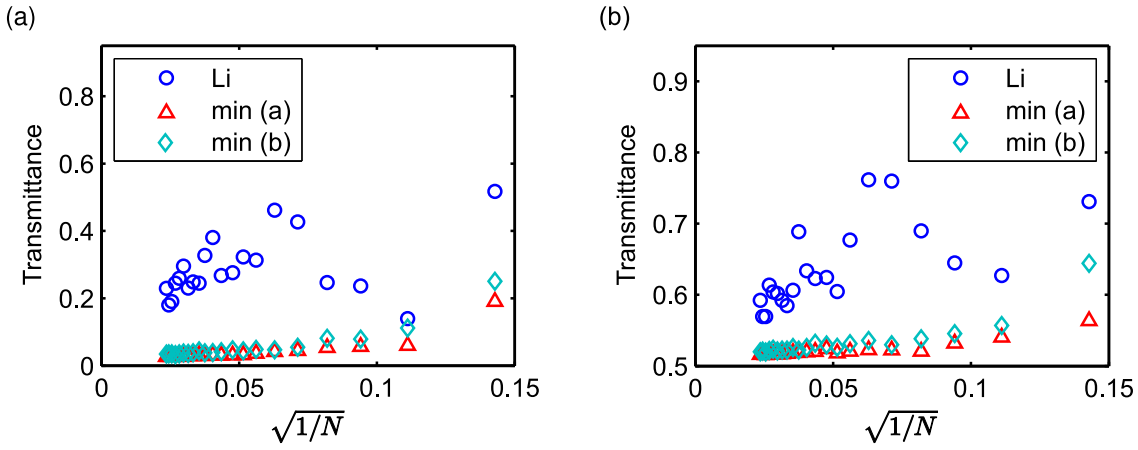

Figure 5.15.: Convergence characteristics of the transmittance into zeroth diffraction order for a square array of metallic crescent-shapes made from gold. The convergence is tested at the resonance of the crescent-shapes in (a) y-polarized excitation at $\lambda = 1900\text{nm}$ (with $\epsilon = -175.08 + 21.43\text{i}$) and (b) x-polarized excitation at $\lambda = 1100\text{nm}$ (with $\epsilon = -53.21 + 4.20\text{i}$).

the material interfaces can be directly translated into well-resolved fields. Thus, we transform the curvilinear field components into the Cartesian space by eq. (5.6) and perform the Fourier back transformation on the adaptive coordinates. The resulting electric field enhancements at the electric and magnetic resonance, determined at a plane 25nm above the glass substrate, are shown in figs. 5.16 (a) and (b), respectively. The fields are calculated with $N = 1257$ Fourier coefficients and the minimized mesh

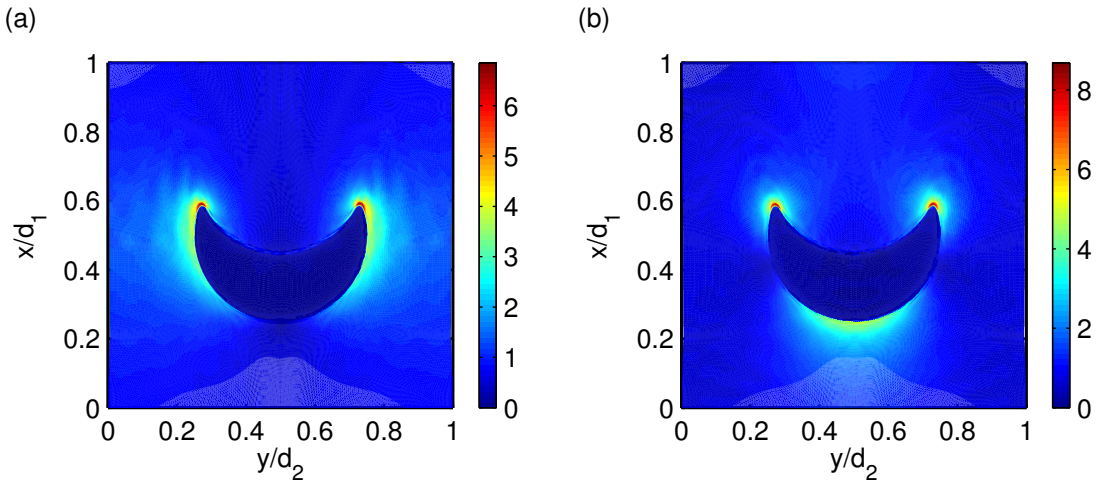

Figure 5.16.: Magnitude of the electric field enhancement as shown by the colorbars at the (a) magnetic and (b) electric resonance calculated on the generated coordinates in fig. 5.13 (a). In (a) the incident electric field is polarized along the y-axis and in (b) along the x-axis.

with tangential term is employed (see fig. 5.13 (a)). The enhancement of the fields near the tips is clearly visible and the distributions of the modes confirms the similarity of the crescent-shape with the split-ring resonators.

5.5. Conclusion

In conclusion, we have included the adaptive spatial resolution (ASR) and the resulting curvilinear coordinates in the FMM by application of Li's anisotropic formulation. The adapted coordinates for an arbitrary shaped structure are generated by minimizing a fictitious energy functional which favors increased point density near the material boundaries and coordinate lines parallel-aligned to the interfaces.
By studying the three different test cases, we learned that the standard FMM as formulated by Li works reasonably well for grid-aligned dielectric and metallic structures (as shown by the square disks). However, in the case of non-grid-aligned structures (such as circular disks and crescent-shaped antennas) the convergence of the method becomes extremely slow and the computational effort increases enormously. By combining ASR with the FMM such structures can be calculated with reasonable computational effort. We have investigated the convergence behavior at the particle plasmon resonance of the test structures and compared, if accessible, with adaptive coordinates which can be written in an analytical expression as for the square and circular disk. As expected, we obtain fastest convergence on these analytical coordinates, but the results by the automatically generated coordinates follow closely. For the case of the crescent-shaped antenna we do not have analytical coordinates. However, a comparison of the convergence behavior for two different automatically generated coordinates shows good agreement of the results. Additionally, we also present the field distributions at two resonances of the system, where the increased resolution of the coordinates, especially at the two tips, is directly visible in the field plot. The test with the crescent-shaped antenna shows that the automatized mesh generation can be applied to arbitrarily shaped objects due to the flexibility of the minimization. Thus, arbitrarily shaped nano-particles can be investigated by the FMM with ASR.

6. Conclusion and Outlook

In this work, we numerically investigated woodpile and opal photonic crystals via the Fourier Modal Method. We also improved the convergence characteristics of the FMM by applying curvilinear coordinates. These are adapted to the geometry of the investigated system. Furthermore, we showed the improved convergence for several metallic test geometries.

After discussing the necessary basics for this thesis in chapter 2, we introduced in chapter 3 two numerical methods used in the field of diffractive optics after a short historical review. First, we presented the Fourier Modal Method where the system under consideration is illuminated by a plane wave. The system is decomposed along the z-direction in two-dimensional, periodic subsystems by the staircase approximation. For each subsystem, Maxwell's equations are solved separately in the Fourier space. The solutions in the individual slices are combined by a scattering matrix technique. Thus, the reflected and transmitted electric fields can be calculated as well as the fields inside the system. Additionally, we introduced two extensions to the Fourier Modal Method which allow to investigate non-periodic structures and systems by internal sources. The second method we presented is the Chandezon method which solves grating problems by transforming these problems in coordinate where the grating surface is presented as a plane.

In chapter 4, we applied the Fourier Modal Method to investigate photonic crystals which can experimentally be fabricated: woodpiles and opals. In the case of the woodpile photonic crystals we concentrated on the investigation of cavities and straight waveguides. Due to the required periodicity in the method we employed a supercell calculation. We obtained increased transmittance in the frequency range of the stop-band by these elements. Furthermore, we determined the field distributions of the excited cavity modes. These investigations were performed for an idealized woodpile with quadratic rod cross section. Additionally, we also performed calculations for experimentally realized woodpiles. First, such a woodpile was designed to obtain a complete band-gap at the telecommunication wavelength. Then, a straight waveguide was incorporated in a woodpile. In both cases, we found good agreement between the measured and calculated results of these woodpile systems.

In opal photonic crystals, we investigated effects depending on the polarization of the impinging light. We found for illumination with s-polarized light an avoided crossing. For illumination with p-polarized light, we could observe the Brewster angle and the critical angle of diffraction. These three effects were identified in both, the measured and the calculated spectra.

In chapter 5 we presented our progress in improving the convergence of the Fourier Modal Method which is especially important for the investigation of metallic nanostructures due to the large values of the refractive index. By the concept of adaptive

spatial resolution we locally refined the discretization at the material boundaries in order to resolve the material discontinuities in Fourier space appropriately. In order to obtain locally refined coordinates for structures with arbitrary shape we applied an automated mesh generation. The generation works by minimizing a fictitious energy functional which consists of different terms. Among others, these terms increased the point density at the material boundaries and oriented coordinate lines tangential along these boundaries. We showed the improved convergence for three different test structures, namely square disks, circular disks and crescent-shaped optical antennas. In the case of the square and circular disks we could compare our results to analytical adaptive coordinates. We also took advantage of the local refinement in the field calculation by determining the electric field distribution in the electric and magnetic resonance of the crescent-shape. Here, we obtained high resolution of the fields at the tips of the crescent-shape by the adaptive coordinates.

Outlook

As further step, in the case of woodpile photonic crystals with the incorporated cavity and waveguide we can imagine to investigate more complicated waveguide structures which include bends. Additionally, the individual building blocks of the waveguide can be optimized by varying the size or even change the complete design of the cavity. Also, waveguides and cavities in other photonic crystals can be investigated.
Since opals show polarization dependent effects it is interesting to investigate the coupling between the two polarizations, especially the polarization conversion properties. By incidence with an s-polarized plane wave, part of the reflected and transmitted light becomes p-polarized and vice versa. This cross-coupling between the two polarizations can be studied with respect to the bandstructure of the opal photonic crystal. In addition, the conversion can be analyzed as function of the thickness of the opal.
Regarding the adaptive spatial resolution, we used one transformation for the entire system. For applications in more complex systems different slices require different adaptive spatial resolutions. Thus, the different coordinate transformations have to be coupled at the interfaces between neighboring slices. This means, a transformation between the individual coordinate system of the slices has to be performed. This would allow the Fourier Modal Method the calculation of arbitrarily shaped metallic structures, with respect to all three spatial direction. By combining perfectly matched layers and internal sources with the adaptive spatial resolution, the FMM can become a more general computational tool.

A. Fourier Factorization

Since the numerical method, we apply, uses Maxwell's equations in reciprocal space, we need also to Fourier transform the constitutive relations (2.10). In this appendix we discuss how the product of two functions has to be transformed in reciprocal space. Then we apply this for an isotropic medium in a two-dimensional nonrectangular coordinate system and in curvilinear coordinates.

A.1. Laurent and Inverse Rule

In order to solve Maxwell's equations in reciprocal space, the product of permittivity and electric field, which is the dielectric displacement

$$D(x) = \epsilon(x)E(x), \tag{A.1}$$

has to be Fourier transformed in reciprocal space. By describing the functions with infinite Fourier series we can obtain the relations for the coefficients

$$d_n = \sum_{m=-\infty}^{\infty} \epsilon_{n-m} e_m, \tag{A.2}$$

which is known as Laurent's rule [40]. This is the convolution theorem for lattice Fourier transformations. Since we can only handle a finite number of coefficients in the actual calculations we have to truncate the Fourier series. The relation becomes

$$d_n^N = \sum_{m=-N}^{N} \epsilon_{n-m} e_m, \tag{A.3}$$

with $2N+1$ coefficients. The Fourier coefficients of the permittivity can be arranged in a matrix which is called Toeplitz matrix. The coefficients of the Toeplitz matrix $[\![\epsilon]\!]$ are defined as $\epsilon_{nm} = \epsilon_{n-m}$. By calculating the entries of the matrix numerically via Fast Fourier Transformation (FFT) we apply a so-called oversampling [99]. In detail, we perform the numerical Fourier transformation with more coefficients than we actually need because the Fourier coefficients which lie at the boundary of the calculated region in Fourier space are worse due to the aliasing effect. In most calculations in this thesis, we use 1024 real space points along one spatial direction in the transformation. The Fourier coefficients of the function $E(x)$ and $D(x)$ can be written in vectors. Consequently, eq. (A.3) reads

$$\mathbf{d} = [\![\epsilon]\!]\,\mathbf{e}. \tag{A.4}$$

Until now we have not commented on the properties of the functions which have to be Fourier transformed. If the functions are discontinuous, the Laurent rule can cause

problems, which were identified and corrected by Li in 1996 [40]. He established three rules which clarify the Fourier transformation of a product as in eq. (A.1). Thus we have to distinguish three different types

- type 1: $E(x)$ and $\epsilon(x)$ have no concurrent jump discontinuities. We have to apply Laurent's rule as in eq. (A.4).
- type 2: $E(x)$ and $\epsilon(x)$ have concurrent jump discontinuities which are pairwise complementary. Therefore, $D(x)$ is continuous. In this case we have to apply Li's inverse rule

$$\mathbf{d} = \left[\!\left[\frac{1}{\epsilon}\right]\!\right]^{-1} \mathbf{e}. \tag{A.5}$$

  By Fourier transforming the reciprocal of the function $\epsilon(x)$ and inverting the resulting Toeplitz matrix, the continuous function $D(x)$ is perfectly reproduced by the Fourier coefficients in eq. (A.5).
- type 3: $E(x)$ and $\epsilon(x)$ have concurrent jump discontinuities which are not pairwise complementary. In this case, Li could not give any advice what to do.

An example for the Laurent and inverse rule is shown in fig. A.1 where the product in eq. (A.1) of a concurrent jump discontinuity is calculated according to eq. (A.4) and eq. (A.5). Here, the product function $D(x)$ obtained by Laurent's rule shows oscillations close to the interface, which vanish in the case of the inverse rule. The oscillations can be assigned to the Gibbs phenomenon. In the limit of the sum about the infinite Fourier series the inverse and the Laurent rule would become identical, but since we can only consider a finite number of coefficients, we have to differ between these two cases.
Since the product in eq. (A.1) represents in our case the constitutive relations, the Laurent and the inverse rule are sufficient. The jump discontinuities in the permittivity function describe material interfaces and the behavior of the electric field and dielectric displacement is clearly depicted by the continuity conditions in eqs. (2.35) and (2.37).

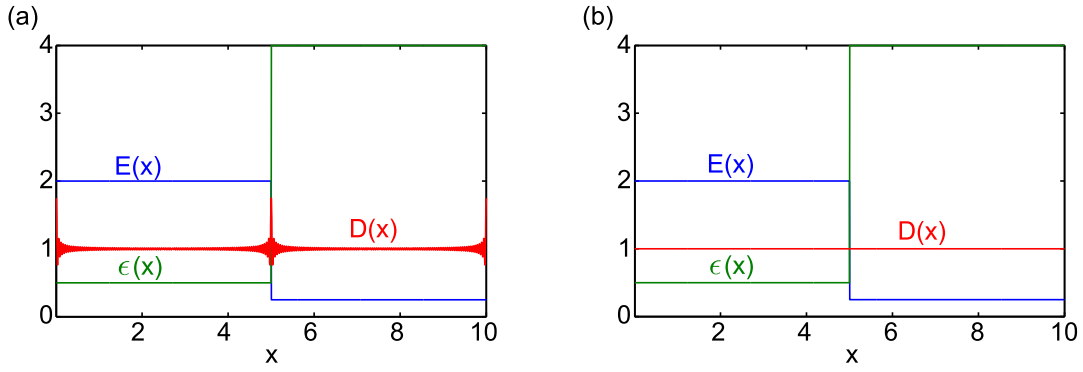

Figure A.1.: (a) Laurent and (b) inverse rule for a system with a concurrent jump discontinuity. The functions $E(x)$ and $\epsilon(x)$ are Fourier transformed and multiplied in Fourier space by the two rules. Finally, the result $D(x)$ is back transformed in real space and presented as the red curve in the graphs.

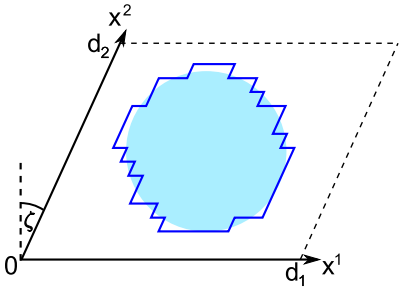

Figure A.2.: Discretized permittivity distribution in a nonrectangular unit cell. The structure (a circle) is shown in light blue and the corresponding zigzag contour in dark blue.

A.2. Nonrectangular Coordinates

Now, we apply the Fourier factorization rules in the FMM. Since, in the general case, Maxwell's equations are applied in nonrectangular coordinates (3.1) the permittivity is anisotropic. Finally, we obtain for the material equation [18]

$$D^1 = \bar{\epsilon}E^1 = \sec\zeta\bar{\epsilon}E_1 - \tan\zeta\bar{\epsilon}E_2, \tag{A.6a}$$
$$D^2 = \bar{\epsilon}E^2 = -\tan\zeta\bar{\epsilon}E_1 + \sec\zeta\bar{\epsilon}E_2, \tag{A.6b}$$
$$D^3 = \bar{\epsilon}E^3 = \cos\zeta\bar{\epsilon}E_3. \tag{A.6c}$$

The permittivity in the Cartesian system is isotropic. It is denoted by $\bar{\epsilon}$. These equations have to be Fourier transformed along the x^1- and x^2-directions. Therefore, the structure in the two-dimensional unit cell is discretized on the nonrectangular grid by the staircase approximation which is illustrated in fig. A.2. Evidently, the structure is described by a zigzag contour.
In order to perform the Fourier transformation we have to know which field components are continuous in the discretized system. For transformation along the x^1-direction E_2 is the tangential component of the electric field along the zigzag contour of the material interface since the covariant component is obtained by the projection of the contravariant basis vector on the field vector (see section 2.7.1). The contravariant component D^1 is the normal component of the dielectric displacement on the surface as the contravariant basis vector is normal to the coordinate surface. Both components, E_2 and D^1, are in this case continuous. Respectively, for transformation along the x^2-direction the E_1 and D^2 components are continuous.
Thus, while Fourier transforming eq. (A.6) we always have to keep in mind the continuous components.
First, we transform eq. (A.6a). We start with the x^1-direction which is transformed according to the inverse rule [18]

$$\left[D^1\right]_1 = \left[\frac{1}{\bar{\epsilon}}\right]_1^{-1} \left[\sec\zeta E_1 - \tan\zeta E_2\right]_1 . \tag{A.7}$$

The transformation along the x^2-direction results in

$$\left[D^1\right]_{12} = \cos\zeta \left[\left[\frac{1}{\bar{\epsilon}}\right]_1^{-1}\right]_2 [E_1]_{12} - \sin\zeta \left[\left[\frac{1}{\bar{\epsilon}}\right]_1\right]_2^{-1} \left[-\tan\zeta\,[E_1]_1 + \sec\zeta\,[E_2]_1\right]_2, \quad \text{(A.8)}$$

where we applied both Laurent's rule and the inverse rule. Using the notation with the Fourier vectors of the fields, we can conclude the Fourier transformation as

$$\mathbf{d}^1 = \left(\cos\zeta \left[\left[\frac{1}{\bar{\epsilon}}\right]_1^{-1}\right]_2 + \sin\zeta\tan\zeta \left[\!\left[\frac{1}{\bar{\epsilon}}\right]\!\right]^{-1}\right)\mathbf{e}_1 - \tan\zeta \left[\!\left[\frac{1}{\bar{\epsilon}}\right]\!\right]^{-1}\mathbf{e}_2. \quad \text{(A.9)}$$

The second equation (A.6b) is first transformed with respect to x^2

$$\left[D^2\right]_2 = \left[\frac{1}{\bar{\epsilon}}\right]_2^{-1} \left[-\tan\zeta\bar{\epsilon}E_1 + \sec\zeta\bar{\epsilon}E_2\right]_2, \quad \text{(A.10)}$$

and afterwards with respect to x^1

$$\left[D^2\right]_{21} = \cos\zeta \left[\left[\frac{1}{\bar{\epsilon}}\right]_2^{-1}\right]_1 [E_2]_{21} - \sin\zeta \left[\left[\frac{1}{\bar{\epsilon}}\right]_2\right]_1^{-1} \left[\sec\zeta\,[E_1]_2 - \tan\zeta\,[E_2]_2\right]_1. \quad \text{(A.11)}$$

Finally, we obtain

$$\mathbf{d}^2 = -\tan\zeta \left[\!\left[\frac{1}{\bar{\epsilon}}\right]\!\right]^{-1}\mathbf{e}_1 + \left(\cos\zeta \left[\left[\frac{1}{\bar{\epsilon}}\right]_2^{-1}\right]_1 + \sin\zeta\tan\zeta \left[\!\left[\frac{1}{\bar{\epsilon}}\right]\!\right]^{-1}\right)\mathbf{e}_2. \quad \text{(A.12)}$$

The last material equation (A.6c) can be Fourier transform in both directions via Laurent's rule since the component E_3 is always continuous

$$\mathbf{d}^3 = \cos\zeta\,[\![\bar{\epsilon}]\!]\,\mathbf{e}_3. \quad \text{(A.13)}$$

We can write the Fourier transformed material equation as $\mathbf{d}^i = [\![\epsilon^{ij}]\!]\,\mathbf{e}_j$. Consequently, we can identify the Toeplitz matrices of the anisotropic components

$$[\![\epsilon^{11}]\!] = \cos\zeta \left[\left[\frac{1}{\bar{\epsilon}}\right]_1^{-1}\right]_2 + \sin\zeta\tan\zeta \left[\!\left[\frac{1}{\bar{\epsilon}}\right]\!\right]^{-1}, \quad \text{(A.14a)}$$

$$[\![\epsilon^{12}]\!] = -\tan\zeta \left[\!\left[\frac{1}{\bar{\epsilon}}\right]\!\right]^{-1}, \quad \text{(A.14b)}$$

$$[\![\epsilon^{21}]\!] = -\tan\zeta \left[\!\left[\frac{1}{\bar{\epsilon}}\right]\!\right]^{-1}, \quad \text{(A.14c)}$$

$$[\![\epsilon^{22}]\!] = \cos\zeta \left[\left[\frac{1}{\bar{\epsilon}}\right]_2^{-1}\right]_1 + \sin\zeta\tan\zeta \left[\!\left[\frac{1}{\bar{\epsilon}}\right]\!\right]^{-1}, \quad \text{(A.14d)}$$

$$[\![\epsilon^{33}]\!] = \cos\zeta\,[\![\bar{\epsilon}]\!]. \quad \text{(A.14e)}$$

The other components are equal to zero.

A.3. Curvilinear Coordinates

In curvilinear coordinates permittivity and permeability become anisotropic. We have to apply the Fourier factorization rules on the anisotropic material equation. Here, we discuss only the permittivity; the permeability is treated identically. The dielectric material equation

$$D^i = \epsilon^{ij} E_j \tag{A.15}$$

can be Fourier transformed as described in ref. [30]. Since the coordinate transformation in the curvilinear coordinates acts only on the x^1 and x^2 coordinate, we can restrict the anisotropic treatment to materials with principal axis along x^3-axis. Thus, we have to consider the material equation in the form

$$D^1 = \epsilon^{11} E_1 + \epsilon^{12} E_2, \tag{A.16a}$$
$$D^2 = \epsilon^{21} E_1 + \epsilon^{22} E_2, \tag{A.16b}$$
$$D^3 = \epsilon^{33} E_3. \tag{A.16c}$$

Again, the structure in the unit cell is discretized but this time in the curvilinear coordinates. As in appendix A.2, the continuous field components for the transformation along x^1 are D^1, E_2 and E_3 (see fig. A.3). E_1, D^2 and E_3 are continuous for the transformation along x^2.

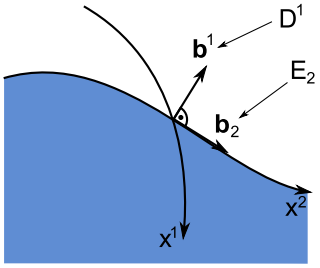

Figure A.3.: Boundary conditions for electric field and displacement components in curvilinear space. D^1 and E_2 are the continuous components at the interface along the x^2-coordinate line.

First, we carry out the transformation along the x^1-axis. Under consideration of Laurent's and the inverse rule we obtain for the material equation (A.16)

$$\left[D^1\right]_1 = \left[\frac{1}{\epsilon^{11}}\right]_1^{-1} \left(\left[E_1\right]_1 + \left[\frac{\epsilon^{12}}{\epsilon^{11}}\right]_1 \left[E_2\right]_1 \right), \tag{A.17a}$$
$$\left[D^2\right]_1 = \left[\frac{\epsilon^{21}}{\epsilon^{11}}\right]_1 \left[D^1\right]_1 + \left[\epsilon^{22} - \frac{\epsilon^{21}\epsilon^{12}}{\epsilon^{11}}\right]_1 \left[E_2\right]_1, \tag{A.17b}$$
$$\left[D^3\right]_1 = \left[\epsilon^{33}\right]_1 \left[E_3\right]_1. \tag{A.17c}$$

In order to simplify the readability of the material equations, we write the partially

Fourier transformed material equation along x^1

$$\begin{aligned}
\left[D^1\right]_1 &= Q_1^{11}\left[E_1\right]_1 + Q_1^{12}\left[E_2\right]_1, && \text{(A.18a)}\\
\left[D^2\right]_1 &= Q_1^{21}\left[E_1\right]_1 + Q_1^{22}\left[E_2\right]_1, && \text{(A.18b)}\\
\left[D^3\right]_1 &= Q_1^{33}\left[E_3\right]_1, && \text{(A.18c)}
\end{aligned}$$

with the quantities Q_1^{ij}

$$\begin{aligned}
Q_1^{11} &= \left[\frac{1}{\epsilon^{11}}\right]_1^{-1}, && \text{(A.19a)}\\
Q_1^{12} &= \left[\frac{1}{\epsilon^{11}}\right]_1^{-1}\left[\frac{\epsilon^{12}}{\epsilon^{11}}\right]_1, && \text{(A.19b)}\\
Q_1^{21} &= \left[\frac{\epsilon^{21}}{\epsilon^{11}}\right]_1\left[\frac{1}{\epsilon^{11}}\right]_1^{-1}, && \text{(A.19c)}\\
Q_1^{22} &= \left[\frac{\epsilon^{21}}{\epsilon^{11}}\right]_1\left[\frac{1}{\epsilon^{11}}\right]_1^{-1}\left[\frac{\bar{\epsilon}^{12}}{\bar{\epsilon}^{11}}\right]_1 - \left[\epsilon^{22} - \frac{\epsilon^{21}\epsilon^{12}}{\epsilon^{11}}\right]_1, && \text{(A.19d)}\\
Q_1^{33} &= \left[\epsilon^{33}\right]_1. && \text{(A.19e)}
\end{aligned}$$

Then, we perform the transformation of the material equation (A.18) in x^2. We obtain

$$\begin{aligned}
\left[D^2\right]_{12} &= \left[\left(Q_1^{22}\right)^{-1}\right]_2^{-1}\left(\left[\left(Q_1^{22}\right)^{-1}Q_1^{21}\right]_2\left[E_1\right]_{12} + \left[E_2\right]_{12}\right), && \text{(A.20a)}\\
\left[D^1\right]_{12} &= \left[Q_1^{12}\left(Q_1^{22}\right)^{-1}\right]_2\left[D^2\right]_{12} + \left[Q_1^{11} - Q_1^{12}\left(Q_1^{22}\right)^{-1}Q_1^{21}\right]_2\left[E_1\right]_{12}, && \text{(A.20b)}\\
\left[D^3\right]_{12} &= \left[Q_1^{33}\right]_2\left[E_3\right]_{12}. && \text{(A.20c)}
\end{aligned}$$

Finally, the Fourier transformed material equations in the reciprocal space is

$$\begin{aligned}
\mathbf{d}^1 &= \left[\!\left[\epsilon^{11}\right]\!\right]_{12}\mathbf{e}_1 + \left[\!\left[\epsilon^{12}\right]\!\right]_{12}\mathbf{e}_2, && \text{(A.21a)}\\
\mathbf{d}^2 &= \left[\!\left[\epsilon^{21}\right]\!\right]_{12}\mathbf{e}_1 + \left[\!\left[\epsilon^{22}\right]\!\right]_{12}\mathbf{e}_2, && \text{(A.21b)}\\
\mathbf{d}^3 &= \left[\!\left[\epsilon^{33}\right]\!\right]_{12}\mathbf{e}_3, && \text{(A.21c)}
\end{aligned}$$

with the matrices for the anisotropic permittivity

$$\begin{aligned}
\left[\!\left[\epsilon^{11}\right]\!\right]_{12} &= \left[Q_1^{12}\left(Q_1^{22}\right)^{-1}\right]_2\left[\left(Q_1^{22}\right)^{-1}\right]_2^{-1}\left[\left(Q_1^{22}\right)^{-1}Q_1^{21}\right]_2, && \text{(A.22a)}\\
&\quad + \left[Q_1^{11} - Q_1^{12}\left(Q_1^{22}\right)^{-1}Q_1^{21}\right]_2, && \text{(A.22b)}\\
\left[\!\left[\epsilon^{12}\right]\!\right]_{12} &= \left[Q_1^{12}\left(Q_1^{22}\right)^{-1}\right]_2\left[\left(Q_1^{22}\right)^{-1}\right]_2^{-1}, && \text{(A.22c)}\\
\left[\!\left[\epsilon^{21}\right]\!\right]_{12} &= \left[\left(Q_1^{22}\right)^{-1}\right]_2^{-1}\left[\left(Q_1^{22}\right)^{-1}Q_1^{21}\right]_2, && \text{(A.22d)}\\
\left[\!\left[\epsilon^{22}\right]\!\right]_{12} &= \left[\left(Q_1^{22}\right)^{-1}\right]_2^{-1}, && \text{(A.22e)}\\
\left[\!\left[\epsilon^{33}\right]\!\right]_{12} &= \left[Q_1^{33}\right]_2. && \text{(A.22f)}
\end{aligned}$$

We can summarize the Fourier transformation of the anisotropic permittivity with the help of the compact notation introduced by Li [30]. The Fourier transformation in x^1 is described by the operator

$$L_1 = l_1^+ F_1 l_1^-, \tag{A.23}$$

and the transformation in x^2 by

$$L_2 = l_2^+ F_2 l_2^-. \tag{A.24}$$

The operator F_i denotes the Fourier transform with respect to the variable x^i. We arrange the resulting Fourier coefficients in a Toeplitz matrix. The operator $l_k^\pm$ acts on the anisotropic components as

$$B^{ij} = l_k^\pm(A^{ij}) \tag{A.25}$$

being defined by

$$B^{ij} = \begin{cases} \left(A^{kk}\right)^{-1} & , k = i = j \\ \left(A^{kk}\right)^{-1} A^{kj} & , i = k, k \neq j \\ A^{ik}\left(A^{kk}\right)^{-1} & , k = j, k \neq i \\ A^{ij} \pm A^{ik}\left(A^{kk}\right)^{-1} A^{kj} & , k \neq j, k \neq i \end{cases} \tag{A.26}$$

Then, the Fourier representation of the permittivity can be expressed as

$$\left[\!\left[\epsilon^{ij}\right]\!\right]_{12} = L_2 L_1(\epsilon^{ij}), \tag{A.27}$$

where we first carry out the transformation in x^1 and thereafter in x^2 as shown in the derivation above. But, we can also flip the order to obtain

$$\left[\!\left[\epsilon^{ij}\right]\!\right]_{21} = L_1 L_2(\epsilon^{ij}). \tag{A.28}$$

The two possibilities do not give the same result due to the truncation of the Fourier series. By increasing the number of coefficients the difference becomes smaller. Thus, the possible symmetry in the structure is not conserved in the Fourier transformed permittivity. In order to conserve the symmetry we symmetrize the two results and use

$$\left[\!\left[\epsilon^{ij}\right]\!\right] = \frac{\left[\!\left[\epsilon^{ij}\right]\!\right]_{12} + \left[\!\left[\epsilon^{ij}\right]\!\right]_{21}}{2}. \tag{A.29}$$

By the symmetrization the energy balance in the FMM is lost. However, by increasing the number of Fourier coefficients this effect is reduced. In our calculations we use enough Fourier coefficients that we cannot observe violations of the energy conservation.

Bibliography

[1] S. John, "Strong localization of photons in certain disordered dielectric superlattices," *Phys. Rev. Lett.*, vol. 58, p. 2486, 1987.

[2] E. Yablonovitch, "Inhibited spontaneous emission in solid-state physics and electronics," *Phys. Rev. Lett.*, vol. 58, p. 2059, 1987.

[3] V. Shalaev, "Optical negative-index metamaterials," *Nature Photon.*, vol. 1, p. 41, 2007.

[4] N. Liu, T. Weiss, M. Mesch, R. Langguth, U. Eigenthaler, M. Hirscher, and C. S

[5] J. Pendry, "Negative refraction makes a perfect lens," *Phys. Rev. Lett.*, vol. 85, p. 3966, 2000.

[6] S. Noda, M. Fujita, and T. Asano, "Spontaneous-emission control by photonic crystals and nanocavities," *Nat. Photon.*, vol. 1, p. 449, 2007.

[7] J. Joannopoulos, R. Meade, and J. Winn, *Photonic Crystals: Molding the Flow of Light*. Princton University Press, first ed., 1995.

[8] V. Veselago, "The electrodynamics of substances with simultaneously negative values of ϵ and μ," *Sov. Phys. Usp.*, vol. 10, p. 509, 1968.

[9] J. B. Pendry, D. Schurig, and D. R. Smith, "Controlling electromagnetic fields," *Science*, vol. 312, p. 1780, 2006.

[10] U. Leonhardt, "Optical conformal mapping," *Science*, vol. 312, p. 1777, 2006.

[11] D. Schurig, J. Mock, B. Justice, S. Cummer, J. B. Pendry, A. Starr, and D. R. Smith, "Metamaterial electromagnetic cloak at microwave frequencies," *Science*, vol. 314, p. 977, 2006.

[12] A. Taflove and S. Hagness, *Computational Electrodynamics: The finite-difference time-domain method*. Artech House, third ed., 2005.

[13] J. Hesthaven and T. Warburton, *Nodal Discontinuous Galerkin Methods: Algorithms, Analysis, and Applications*. Springer Verlag, first ed., 2007.

[14] J. Jin, *Computational Electrodynamics: The Finite Element Method in Electromagnetics*. John Wiley & Sons, second ed., 2002.

[15] K. Busch and S. John, "Photonic band gap formation in certain self-organizing systems," *Phys. Rev. E*, vol. 58, p. 3896, 1998.

[16] M. Nevière and E. Popov, *Light propagation in periodic media: Differential theory and design*. Marcel Dekker, 2003.

[17] J. Chandezon, D. Maystre, and G. Raoult, "A new theoretical method for diffraction gratings and its numerical application," *J. Optics*, vol. 11, p. 235, 1980.

[18] L. Li, "New formulation of the Fourier modal method for crossed surface-relief gratings," *J. Opt. Soc. Am. A*, vol. 14, p. 2758, 1997.

[19] J. D. Jackson, *Classical Electrodynamics*. John Wiley & Sons, third ed., 1999.

[20] A. Lakhtakia and R. Messier, *Sculptured Thin Films*. SPIE Press, 2005.

[21] R. W. Boyd, *Nonlinear Optics*. Academic Press San Diego, first ed., 1992.

[22] I. Bronstein, K. Semendjaev, G. Musiol, and H. Mühlig, *Taschenbuch der Mathematik*. Verlag Harri Deutsch, fifth ed., 2000.

[23] K. Busch, G. von Freymann, S. Linden, S. F. Mingaleev, L. Tkeshelashvili, and M. Wegener, "Periodic nanostructures for photonics," *Physics Reports*, vol. 444, p. 101, 2007.

[24] E. Hecht, *Optik*. Oldenbourg Wissenschaftsverlag, third ed., 2005.

[25] P. B. Johnson and R. W. Christy, "Optical constants of the noble metals," *Phys. Rev. B*, vol. 6, p. 4370, 1972.

[26] A. Vial, A.-S. Grimault, D. Macías, D. Barchiesi, and M. L. de la Chapelle, "Improved analytical fit of gold dispersion: Application to the modeling of extinction spectra with a finite-difference time-domain method," *Phys. Rev. B*, vol. 71, p. 085416, 2005.

[27] M. Born and E. Wolf, *Principles of Optics*. Cambridge University Press, seventh (expanded) ed., 2007.

[28] L. Novotny and B. Hecht, *Principles of Nano-Optics*. Cambridge University Press, 2007.

[29] E. J. Post, *Formal Structure of Electromagnetics*. North-Holland Publishing Company, 1962.

[30] L. Li, "Fourier modal method for crossed anisotropic gratings with arbitrary permittivity and permeability tensors," *J. Opt. A: Pure Appl. Opt.*, vol. 5, p. 345, 2003.

[31] C. Kittel, *Introduction to Solid State Physics*. John Wiley & Sons, seventh ed., 1996.

[32] L. Rayleigh, "On the dynamical theory of gratings," *Proc. R. Soc. Lond. A*, vol. 79, p. 399, 1907.

[33] R. W. Wood, "Anomalous diffraction gratings," *Phys. Rev.*, vol. 48, p. 928, 1935.

[34] M. G. Moharam and T. K. Gaylord, "Rigorous coupled-wave analysis of planar-grating diffraction," *J. Opt. Soc. Am.*, vol. 71, p. 811, 1981.

[35] M. G. Moharam and T. K. Gaylord, "Diffraction analysis fo dielectric surface-relief gratings," *J. Opt. Soc. Am.*, vol. 72, p. 1385, 1982.

[36] L. Li and C. Haggans, "Convergence of the coupled-wave method for metallic lamellar diffraction gratings," *J. Opt. Soc. Am. A*, vol. 10, p. 1184, 1993.

[37] L. Li, "Formulation and comparison of two recursive matrix algorithms for modeling layered diffraction gratings," *J. Opt. Soc. Am. A*, vol. 13, p. 1024, 1996.

[38] P. Lalanne and G. M. Morris, "Highly improved convergence of the coupled-wave method for TM polarization," *J. Opt. Soc. Am. A*, vol. 13, p. 779, 1996.

[39] G. Granet and B. Guizal, "Efficient implementation of the coupled-wave method for metallic lamellar gratings in TM polarization," *J. Opt. Soc. Am. A*, vol. 13, p. 1019, 1996.

[40] L. Li, "Use of Fourier series in the analysis of discontinuous periodic structures," *J. Opt. Soc. Am. A*, vol. 13, p. 1870, 1996.

[41] E. Popov and M. Nevière, "Grating theory: new equations in Fourier space leading to fast converging results for TM polarization," *J. Opt. Soc. Am. A*, vol. 17, p. 1773, 2000.

[42] T. W. Preist, N. P. K. Cotter, and J. R. Sambles, "Periodic multilayer gratings of arbitrary shape," *J. Opt. Soc. Am. A*, vol. 12, p. 1740, 1995.

[43] L. Li and J. Chandezon, "Improvement of the coordinate transformation method for surface-relief gratings with sharp edges," *J. Opt. Soc. A*, vol. 13, p. 2247, 1996.

[44] D. M. Whittaker and I. S. Culshaw, "Scattering-matrix treatment of patterned multilayer photonic structures," *Phys. Rev. B*, vol. 60, p. 2610, 1999.

[45] E. L. Tan, "Note on formulation of the enhanced scattering (transmittance-) matrix approach," *J. Opt. Soc. Am. A*, vol. 19, p. 1157, 2002.

[46] L. Li, "Note on the s-matrix propagation algorithm," *J. Opt. Soc. Am. A*, vol. 20, p. 655, 2003.

[47] N. P. K. Cotter, T. W. Preist, and J. R. Sambles, "Scattering-matrix approach to multilayer diffraction," *J. Opt. Soc. Am. A*, vol. 12, p. 1097, 1995.

[48] D. Armani, T. Kippenberg, S. Spillane, and K. Vahala, "Ultra-high-Q toroid microcavity on a chip," *Nature*, vol. 421, p. 925, 2003.

[49] M. Husnik, M. Klein, N. Feth, M. König, J. Niegemann, K. Busch, S. Linden, and M. Wegener, "Absolute extinction cross-section of individual magnetic split-ring resonators," *Nat. Photon.*, vol. 2, p. 614, 2008.

[50] J. Knight, "Photonic crystal fibres," *Nature*, vol. 424, p. 847, 2003.

[51] Y. Vlasov, M. O'Boyle, H. Hamann, and S. McNab, "Active control of slow light on a chip with photonic crystal waveguides," *Nature*, vol. 438, p. 65, 2005.

[52] A. Faraon, I. Fushman, D. Englund, N. Stoltz, P. Petroff, and J. Vuckovic, "Coherent generation of non-calssical light on a chip via photon induced tunneling and blockade," *Nat. Phys.*, vol. 4, p. 859, 2008.

[53] P. Lalanne and E. Silberstein, "Fourier-modal methods applied to waveguide computational problems," *Opt. Lett.*, vol. 25, p. 1092, 2000.

[54] J. Bérenger, "A perfectly matched layer for the absorption of electromagnetic waves," *J. Comput. Phys.*, vol. 114, p. 185, 1994.

[55] S. Gedney, "An anisotropic perfectly matched layer-absorbing medium for the truncation of fdtd lattices," *IEEE Trans. Antennas Propag.*, vol. 44, p. 1630, 1996.

[56] E. Silberstein, P. Lalanne, J.-P. Hugonin, and Q. Cao, "Use of grating theories in integrated optics," *J. Opt. Soc. Am. A*, vol. 18, p. 2865, 2001.

[57] Q. Cao, P. Lalanne, and J.-P. Hugonin, "Stable and efficient bloch-mode computational method for one-dimensional grating waveguides," *J. Opt. Soc. Am. A*, vol. 19, p. 335, 2002.

[58] J.-P. Hugonin and P. Lalanne, "Perfectly matched layers as nonlinear coordinate transforms: a generalized formalization," *J. Opt. Soc. Am. A*, vol. 22, p. 1844, 2005.

[59] T. Zebrowski, "Nonlinear complex coordinate transformations for the Fourier modal method," Master's thesis, Universität Karlsruhe, 2008.

[60] H. Benisty, R. Stanley, and M. Mayer, "Method of source terms for dipole emission modification in modes of arbitrary planar structures," *J. Opt. Soc. Am. A*, vol. 15, p. 1192, 1998.

[61] A. David, *High-efficiency GaN-based light-emitting diodes: Light extraction by photonic crystals and microcavities*. PhD thesis, Institut d'Optique, Orsay, France, 2006.

[62] C. Klock, "Modeling of point sources in photonic structures via the Fourier modal method," Master's thesis, Universität Karlsruhe, 2009.

[63] J. Chandezon, M. T. Dupuis, G. Gornet, and D. Maystre, "Multicoated gratings: a differential formalism applicable in the entire optical region," *J. Opt. Soc. Am.*, vol. 72, p. 839, 1982.

[64] L. Li, J. Chandezon, G. Granet, and J.-P. Plumey, "Rigorous and efficient grating-analysis method made easy for optical engineers," *Appl. Opt.*, vol. 38, p. 304, 1999.

[65] E. Popov, Nevière, B. Gralak, and G. Tayeb, "Staircase approximation validity for arbitrary-shaped gratings," *J. Opt. Soc. Am. A*, vol. 19, p. 33, 2002.

[66] P. Vukusic and J. Sambles, "Photonic structures in biology," *Nature*, vol. 424, p. 852, 2003.

[67] J. Sanders, "Colour of precious opals," *Nature*, vol. 204, p. 1151, 1964.

[68] K. Ho, C. Chan, C. Soukoulis, R. Biswas, and M. Sigalas, "Photonic bandgaps in three dimensions: New layer-by-layer periodic structures," *Solid State Comm.*, vol. 89, p. 413, 1994.

[69] S. Noda, K. Tomoda, N. Yamamoto, and A. Chutinan, "Full three-dimensional photonic bandgap crystals at near-infrared wavelengths," *Science*, vol. 289, p. 604, 2000.

[70] G. von Freymann, A. Ledermann, M. Thiel, I. Staude, S. Essig, K. Busch, and M. Wegener, "Three-dimensional nanostructures for photonics," *Adv. Funct. Mater.*, vol. 20, p. 1038, 2010.

[71] M. Deubel, G. v. Freymann, M. Wegener, S. Pereira, K. Busch, and C. M. Soukoulis, "Direct laser writing of three-dimensional photonic-crystal templates for telecommunications," *Nature Mat.*, vol. 3, p. 444, 2004.

[72] N. Tétreault, G. v. Freymann, M. Deubel, M. Hermatschweiler, F. Pérez-Willard, S. John, M. Wegener, and G. Ozin, "New route to three-dimensional photonic bandgap materials: Silicon double inversion of polymer templates," *Adv. Mater.*, vol. 18, p. 457, 2006.

[73] S. Shoji, H.-B.Sun, and S. Kawata, "Photofabrication of wood-pile three-dimensional photonic crystals using four-beam laser interference," *Appl. Phys. Lett.*, vol. 83, p. 608, 2003.

[74] Y. Lin and P. Herman, "Effect of structural variation on the photonic band gap in woodpilee photonic crystal with body-centered-cubic symmetry," *J. Appl. Phys.*, vol. 98, p. 063104, 2005.

[75] I. Staude, M. Thiel, S. Essig, C. Wolff, K. Busch, G. von Freymann, and M. Wegener, "Fabrication and characterization of silicon woodpile photonic crystals with a complete bandgap at telecom wavelenghts," *Opt. Lett.*, vol. 35, p. 1094, 2010.

[76] I. Staude, G. von Freymann, S. Essig, K. Busch, and M. Wegener, "Waveguides in three-dimensional photonic-bandgap materials by direct laser writing and silicon double inversion," *Opt. Lett.*

[77] E. Yablonovitch, "Photonic band-gap structures," *J. Opt. Soc. Am. B*, vol. 10, p. 283, 1987.

[78] S. Kawashima, K. Ishizaki, and S. Noda, "Light propagation in three-dimensional photonic crystals," *Opt. Express*, vol. 18, p. 386, 2010.

[79] S. Romanov, U. Peschel, M. Bardosova, S. Essig, and K. Busch, "Suppression of the critical angle of diffraction in thin-film colloidal photonic crystals," *Phys. Rev. B*, vol. 82, p. 115403, 2010.

[80] A. Blanco, E. Chomski, S. Grabtchak, M. Ibisate, S. John, S. Leonard, C. Lopez, F. Meseguer, H. Miguez, J. Mondia, G. Ozin, O. Toader, and H. van Driel, "Large-scale synthesis of a silicon photonic crystal with a complete three-dimesional bandgap near 1.5 micrometres," *Nature*, vol. 405, p. 437, 2000.

[81] K. Busch, S. Lölkes, R. Wehrspohn, and H. Föll, *Photonic Crystals: Advances in Design, Fabrication, and Characterization.* Wiley-VCH, 2004.

[82] J.-M. Lourtioz, *Photonic Crystals: Towards Nanoscale Photonic Devices.* Springer, 2005.

[83] M. Müller, R. Zentel, T. Maka, S. Romanov, and C. S. Torres, "Dye-containing polymer beads as photonic crystals," *Chem. Mater.*, vol. 12, p. 2508, 2000.

[84] A. Baryshev, A. Khanikaev, H. Uchida, M. Inoue, and M. Limonov, "Interaction of polarized light with three-dimensional opal-based photonic crystals," *Phys. Rev. B*, vol. 73, p. 033103, 2006.

[85] G. J. Pearce, T. D. Hedley, and D. M. Bird, "Adaptive curvilinear coordinates in a plane-wave solution of Maxwell's equations in photonic crystals," *Phys. Rev. B*, vol. 71, p. 195108, 2005.

[86] T. Schuster, J. Ruoff, N. Kerwien, S. Rafler, and W. Osten, "Normal vector method for convergence improvement using the RCWA for crossed gratings," *J. Opt. Soc. Am. A*, vol. 24, p. 2880, 2007.

[87] G. Granet, "Reformulation of the lamellar grating problem through the concept of adaptive spatial resolution," *J. Opt. Soc. Am. A*, vol. 16, p. 2510, 1999.

[88] T. Vallius and M. Honkanen, "Reformulation of the Fourier modal method with adaptive spatial resolution: application to multilevel profiles," *Opt. Express*, vol. 10, p. 24, 2002.

[89] G. Granet and J.-P. Plumey, "Parametric formulation of the Fourier modal method for crossed surface-relief gratings," *J. Opt. A: Pure Appl. Opt.*, vol. 4, p. S145, 2002.

[90] T. Weiss, G. Granet, N. A. Gippius, S. G. Tikhodeev, and H. Giessen, "Matched coordinates and adaptive spatial resolution in the Fourier modal method," *Opt. Express*, vol. 17, p. 8051, 2009.

[91] G. Granet and B. Guizal, "Analysis of strip gratings using a parametric modal method by Fourier expansions," *Opt. Comm.*, vol. 255, p. 1, 2005.

[92] S. Essig and K. Busch, "Generation of adaptive coordinates and their use in the Fourier Modal Method," *Opt. Express*, vol. 18, p. 23258, 2010.

[93] S. Linden, C. Enkrich, M. Wegener, J. Zhou, T. Koschny, and C. Soukoulis, "Magnetic response of metamaterials at 100 terahertz," *Science*, vol. 306, p. 1351, 2004.

[94] L.-H. Shao, M. Ruther, S. Linden, S. Essig, K. Busch, and J. Weissmüller, "Electrochemical modulation of photonic metamaterials," *Adv. Mater.*, vol. 22, p. 5173, 2010.

[95] F. Gygi, "Electronic-structure calculations in adaptive coordinates," *Phys. Rev. B*, vol. 48, p. 11692, 1993.

[96] P. Götz, T. Schuster, K. Frenner, S. Rafler, and W. Osten, "Normal vector method for the RCWA with automated vector field generation," *Opt. Express*, vol. 16, p. 17295, 2008.

[97] B. Bai and L. Li, "Group-theoretic approach to enhancing the Fourier modal method for crossed gratings with C_4 symmetry," *J. Opt. A: Pure Appl. Opt.*, vol. 7, p. 783, 2005.

[98] J. S. Shumaker-Parry, H. Rochholz, and M. Kreiter, "Fabrication of crescent-shaped optical antennas," *Adv. Mater.*, vol. 17, p. 2131, 2005.

[99] W. Press, S. Teukolsky, W. Vetterling, and B. Flannery, *Numerical Recipes in C*. Cambridge University Press, second ed., 1992.

Acknowledgments

At this place I would like to thank all the people who contributed to the success of this thesis. Especially, I would like to thank

- Prof. Kurt Busch who gave me the opportunity to work in his group and this interesting research field. I am also grateful that he always takes care of the social aspects in his group.
- Prof. Martin Wegener for kindly agreeing to co-referee this thesis and for giving me the opportunity to contribute to his research that resulted in several publications.
- my diffractive optics colleagues Thomas Zebrowski, Christian Klock, Jens Küchenmeister and Benjamin Lutz who supported me in developing our numerical framework.
- Isabelle Staude and Matthias Ruther from the group of Prof. Martin Wegener who took care of the experimantal realization of some structures for which I could calculate the optical properties.
- Christian Wolff for performing the bandstructure calculations shown in this thesis.
- Sergei Romanov who raised my interest into opal photonic crystals. He also fabricated these opals for which I computed the optical properties.
- the proof-readers Christian Wolff, Michael König, Jens Niegemann, Benjamin Lutz and Thomas Zebrowski. They gave many useful comments that definitely improved my thesis.
- all other actual and former members of the photonics group, who were partners in many interesting discussions. I very much appreciate the frequently occuring barbecues at different locations, mainly at Antje's place.
- Nils and my family for supporting me in all aspects of life.

List of Publications

1. C.E. Kriegler, M.S. Rill, M. Thiel, E. Müller, S. Essig, A. Frölich, G. von Freyman, S. Linden, D. Gerthsen, H. Hahn, K. Busch and M. Wegener, "Transition between corrugated metal films and split-ring-resonator arrays", Appl. Phys. B **96**, 749 (2009)

2. I. Staude, M. Thiel, S. Essig, C. Wolff, K. Busch, G. von Freymann and M. Wegener, "Fabrication and characterization of silicon woodpile photonic crystals with a complete bandgap at telecom wavelengths", Opt. Lett. **35**, 1094 (2010)

3. G. von Freymann, A. Ledermann, M. Thiel, I. Staude, S. Essig, K. Busch and M. Wegener, "Three-Dimensional Nanostructures for Photonics", Adv. Funct. Mater. **20**, 1038 (2010)

4. S. Romanov, U. Peschel, M. Bardosova, S. Essig and K. Busch, "Suppression of the critical angle of diffraction in thin-film colloidal photonic crystals", Phys. Rev. B **82**, 115403 (2010)

5. S. Essig and K. Busch, "Generation of adaptive coordinates and their use in the Fourier Modal Method", Opt. Expr. **18**, 23258 (2010)

6. L. Shao, M. Ruther, S. Linden, S. Essig, K. Busch, J. Weissmüller and M. Wegener, "Electrochemical modulation of photonic metamaterials", Adv. Mater. **22**, 5173 (2010)

7. I. Staude, G. von Freymann, S. Essig, K. Busch and M. Wegener, "Waveguides in three-dimensional photonic-band-gap materials by direct laser writing and silicon double inversion", Opt. Lett. **36**, 67 (2011)